Unveiling Catalytic Species in Suspension/Solution-Based Reactions by *In Situ* X-Ray Absorption Spectroscopy

Evolution of Palladium and Ruthenium Species

Ning Yuan
Faculty of Natural Resources and Agricultural Sciences
Department of Molecular Sciences
Uppsala

Doctoral thesis
Swedish University of Agricultural Sciences
Uppsala 2019

Acta Universitatis agriculturae Sueciae

2019:33

ISSN 1652-6880
ISBN (print version) 978-91-7760-384-9
ISBN (electronic version) 978-91-7760-385-6
© 2019 Ning Yuan, Uppsala
Print: SLU Service/Repro, Uppsala 2019

Unveiling Catalytic Species in Suspension/Solution-Based Reactions by *In Situ* X-Ray Absorption Spectroscopy. Evolution of Palladium and Ruthenium Species

Abstract

The palladium (Pd) and ruthenium (Ru) species in several attractive catalysts have been probed using X-ray absorption spectroscopy (XAS). The study of catalyst evolution in suspension- and solution-based reactions was the primary aim. It was achieved by performing *in situ* XAS experiments on Pd and Ru over the course of the reactions. A custom-made reactor was employed which allowed the catalysts to be mixed with other reaction components under desired conditions.

The first system investigated was the Heck coupling reaction catalyzed by Pd(II) complexes embedded on metal-organic frameworks. Mononuclear Pd complexes are the active species at the first stage of the measurement which then gradually transform into Pd nanoclusters. At a later stage of the measurement, chloride ligands start to bind to surface atoms of the Pd nanoclusters, leading to a deactivation of the catalyst. Pd(II) carbene complexes catalyzing undirected C–H acetoxylation of benzene in the presence of an oxidant were then explored. A gradual ligand substitution occurs, and the mean oxidation state of Pd increases at the same time. At a later stage, Pd nanoclusters form, while the mean oxidation state of Pd returns to the start value. Deactivation of a heterogeneous Pd(II) catalyst during cycloisomerization of acetylenic acids was also investigated using *in situ* XAS. The choice of substrates showed to significantly influence the nature of Pd species, and the formation of Pd(0) aggregates causes the deactivation. Moreover, strategies of reactivating the catalyst and prevention of the deactivation were developed and examined. In the end, the activation process of a Ru catalyst was studied and the structure of the intermediate was determined by *in situ* XAS. It was demonstrated that an electron-donating substituent on the cyclopentadiene ligand exhibits a promoting effect on the activation, while an electron-withdrawing substituent inhibits the activation.

Keywords: Palladium and ruthenium species, Catalysts; Suspension and solution, *In situ* X-ray absorption spectroscopy, Activation, Deactivation

Author's address: Ning Yuan, SLU, Department of Molecular Sciences,
P.O. Box 7015, SE-750 07 Uppsala, Sweden

Dedication

To Lukas, Qiong, Shuxia and Baosheng

Contents

List of publications

This thesis is based on the work contained in the following papers, referred to by Roman numerals in the text:

I Ning Yuan,† Vlad Pascanu,† Zhehao Huang, Alejandro Valiente, Niclas Heidenreich, Sebastian Leubner, Andrew K. Inge, Jakob Gaar, Norbert Stock, Ingmar Persson,* Belén Martín-Matute* and Xiaodong Zou* (2018). Probing the Evolution of Palladium Species in Pd@MOF Catalysts during the Heck Coupling Reaction: An Operando X-Ray Absorption Spectroscopy Study. Journal of the American Chemical Society, 140, pp. 8206−8217.

II Ning Yuan,†* Maitham H. Majeed,† Éva G. Bajnóczi, Axel R. Persson, L. Rein Wallenberg, A. Ken Inge, Niclas Heidenreich, Norbert Stock, Xiaodong Zou, Ola Wendt* and Ingmar Persson* (2019). *In Situ* XAS Study of the Local Structure and Oxidation State Evolutions of Palladium in a Reduced Graphene Oxide Supported Pd(II) Carbene Complex during an Undirected C−H Acetoxylation Reaction. *Catalysis Science & Technology,* 9, pp. 2025−2031.

III Ning Yuan,† Arnar Guðmundsson,† Karl P.J. Gustafson, Michael Oschmann, Oscar Verho, Ingmar Persson, Xiaodong Zou, Éva G. Bajnóczi* and Jan-Erling Bäckvall.* *In Situ* XAS Investigation of the Deactivation and Reactivation Mechanisms of a Heterogeneous Palladium(II) Catalyst During the Cycloisomerization of Acetylenic Acids (manuscript)

IV Alexandre Bruneau, Karl P. J. Gustafson, Ning Yuan, Ingmar Persson, Xiaodong Zou and Jan-Erling Bäckvall* (2017). Synthesis of Bensofurans and Indoles from Terminal Alkynes and Iodoaromatics Catalyzed by

Recylable Palladium Nanoparticles Immobilized on Siliceous Mesocellular Foam. *Chemistry: A European Journal*, 23, pp. 12886–12891.

V Karl P. J. Gustafson,† Tamás Görbe,† Gonzalo De Gonzalo-Calvo, Ning Yuan, Cynthia Schreiber, Andrey Shchukarev, Cheuk-Wai Tai, Ingmar Persson, Xiaodong Zou and Jan-Erling Bäckvall.* Chemoenzymatic Dynamic Kinetic Resolution of Primary Benzylic Amines using Pd(0)-CalB CLEA as a Biohybrid Catalyst (submitted)

VI Karl P. J. Gustafson,† Arnar Guðmundsson,† Éva G. Bajnóczi,† Ning Yuan, Xiaodong Zou, Ingmar Persson* and Jan-Erling Bäckvall.* *In Situ* Structural Determination of a Homogeneous Ruthenium-Catalyst and its Activated Intermediates using X-Ray Absorption Spectroscopy (submitted)

Papers I, II, and IV are reproduced with the permission of the publishers.

* Corresponding author.

The contribution of Ning Yuan to the papers included in this thesis was as follows:

I. Designed the experiments and synthesized the Pd@MOFs together with Vlad Pascanu, wrote the XAS beamtime application at ESRF. Collected the XAS data with collaborators and performed the XAS data analysis. Had major contributions to the writing of the paper and responding to the reviewers' comments.

II. Planned the experiments with Maitham Majeed. Wrote the XAS beamtime application at Petra III, DESY. Collected the XAS data with collaborators and performed the XAS data analysis. Had major contributions to the writing of the paper. Took the responsibilities for submitting the paper and communicating with the journal. Provided main responses to the reviewers' comments.

III. Planned the experiments with Arnar Guðmundsson and Karl Gustafson. Collected the XAS data with collaborators and performed the XAS data analysis. Had major contributions to the writing of the paper.

IV. Participated in the beamtime application, performed the XAS data collection and analysis, wrote the XAS part of the paper.

V. Participated in the beamtime application, performed the XAS data collection and analysis, wrote the XAS part of the paper.

VI. Participated in the planning of the experiment, the XAS beamtime application and data collection at Petra III, DESY. Joined the discussions of the work.

List of tables

List of figures

Abbreviations

AMP	Aminopropyl
BQ	Benzoquinone
CalB	Candida *antartica* lipase B
C–H	Carbon–hydrogen
CLEA	Cross-linked enzyme aggregate
DKR	Dynamic kinetic resolution
DME	Dimethoxyethane
DMF	Dimethylformamide
EXAFS	Extended X-ray absorption fine structure
EDS	Electron dispersive spectroscopy
FT	Fourier transform
FTIR	Fourier-transform infrared spectroscopy
ICP-OES	Inductively coupled plasma-optical emission spectrometry
MCF	Mesocellular foam
MIL	Matérial Institut Lavoisier
MOF	Metal-organic framework
MS	Multiple scattering
NMR	Nuclear magnetic resonance
OAc	Acetoxy
PXRD	Powder X-ray diffraction
rGO	Reduced graphene oxide
S/N	Signal-to-noise ratio
SS	Single backscattering
Sub.	Substrate
TEM	Transmission electron microscopy
TEA	Triethylamine
XANES	X-ray absorption near edge structure
XAS	X-ray absorption spectroscopy
XES	X-ray emission spectroscopy

1 Introduction to Catalysts and Their Characterizations

1.1 Catalysts

Catalysis is the process of facilitating a chemical reaction with the aid of a substance called catalyst, which is neither consumed nor formed during the reaction. A catalyst provides an alternative pathway for the reaction and lowers the energy barrier of the process significantly (Figure 1.1).[1] Catalysis plays an essential role in the modern chemical industry where catalysis-based synthesis contributes to around 60% of chemical products and 90% of current chemical processes.[2]

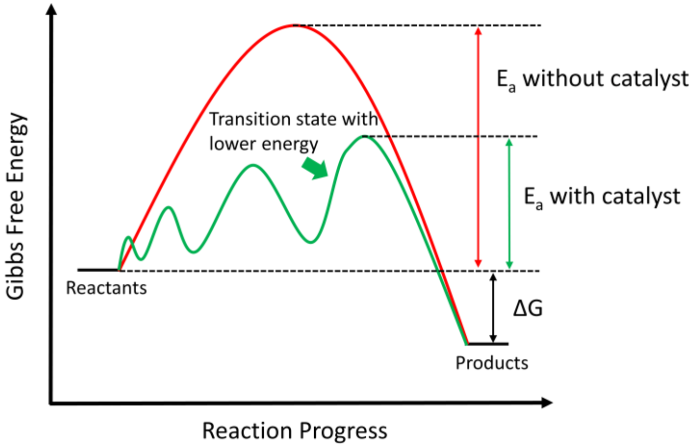

Figure 1.1. Energy diagram of catalyzed and non-catalyzed reactions.

Generally, catalysis is classified into two types, homogeneous and heterogeneous. In homogeneous catalysis, the catalyst exists in the same phase as the reactants. Typically, both the catalyst and the substrates are dissolved in a solvent forming a homogenous solution.[1] The efficiency of homogeneous catalytic reactions is usually high due to high activity and selectivity of the catalysts in comparison to heterogeneous catalysts.[3,4] Structure determination and mechanistic studies of homogeneous catalysts are relatively easy, as well as precise tailoring of the catalysts at the molecular level. However, it can be challenging to separate homogeneous catalysts from products, and therefore difficult to recover and recycle them. Heterogeneous catalysts, on the other hand, operate in a different phase than the reactants. Typical combinations are solid catalyst with gas or liquid reactants. Stability and recyclability are the main advantages of heterogeneous catalysts, which has led to their dominating positions in industrial processes in comparison to homogeneous catalysts.[5] The main weakness of heterogeneous catalysts is their lack of tunability, which hinders them to be adapted effectively to different reaction processes.

The development of catalysts with desirable properties has been a major focus of research in the chemical industry. Transition metals and their complexes have been extensively studied and used both as homogeneous and heterogeneous catalysts. This can partly be attributed to the various oxidation states that transition metals can exist in. Palladium, for instance, can be nucleophilic when it is in an oxidation state of 0. Meanwhile, it can also exhibit properties of an electrophile when the oxidation state is increased to +II or +IV. This makes it possible for palladium to catalyze many reactions via different routes.[6]

1.2 Characterization techniques for catalysts

To a chemist studying catalytic reactions, there are some particularly important questions which should be considered when using a catalyst, for example:

- What is the form of catalytic species in the as-synthesized catalyst?
- What is the form of catalytic species during the reaction?
- What is the form of catalytic species in its deactivated state and what is the cause of the deactivation?
- How does the choice of substrates and/or other reaction components and conditions affect the catalytic species?

There are a few widely used techniques for investigating catalysts. For instance, transmission electron microscopy (TEM) is suitable to study the catalytic species in the form of nanoparticles. Electron-dispersive spectroscopy (EDS) can identify the chemical elements and their distribution in a heterogeneous catalyst. Both X-ray and electron diffraction techniques can determine the structure of a crystalline catalyst. X-ray photoelectron spectroscopy (XPS) can determine the oxidation state of catalytic speciation.

Table 1.1. summarizes some of the techniques commonly used to study catalysts and the main information that they can provide.

Table 1.1. *Typical techniques used to study catalysts*

Techniques	**Main information**
Electron microscopy	Nanoparticle, morphology
Electron-dispersive spectroscopy	Elemental analysis
X-ray/Electron diffraction	Crystalline structure
X-ray photoelectron spectroscopy	Oxidation state
X-ray absorption spectroscopy	Oxidation state, local structures
Fourier-transform infrared spectroscopy	Chemical bonds
Gas-sorption	Porosity, surface area

Each technique has its advantages and limitations and usually multiple techniques are applied to gain a comprehensive understanding of a catalyst. The more information that is available about the catalysts, the more opportunities there are to develop better catalysts or prolong the lifetime of active catalysts. For example, palladium nanoparticles have been extensively used to catalyze various types of reactions. It is known that the surface atoms of the palladium nanoparticles can be oxidized in the presence of oxygen. TEM can be used to acquire information about the size and distribution of the nanoparticles, but it cannot easily distinguish palladium oxide from the metallic palladium. For this reason, XPS measurements are often conducted to identify the co-existence of palladium species in different oxidation states.[7] Another example is metal complex catalysts embedded on crystalline porous materials, for instance, zeolites[8] and metal-organic frameworks (MOFs)[9–11]. X-ray and electron diffraction techniques are accurate in determining the crystalline structures of the supports. However, due to the fact that the spatial distribution of metal complexes often lacks long range order, diffraction methods are limited to providing insights into the structure of the catalytic metal species. Fortunately, element-specific techniques, such as X-ray absorption spectroscopy (XAS), can probe the metal complex centers exclusively and elucidate the structures.

The development of catalysts today is generally moving towards the systems that are more complex in order to achieve better performance. This situation increases the demand for a more thorough understanding of the catalysts, where characterizations by multiple advanced techniques are necessary.

1.3 Objectives of this thesis

The main objective of this thesis is to apply the synchrotron-based *in situ* X-ray absorption spectroscopy as the main approach to provide some insights into the catalytic species of several attractive palladium and ruthenium catalysts over the course of the reactions. Another objective is to make contributions to the relatively challenging area of utilizing *in situ* XAS in suspension/solution-based catalytic systems.

The thesis starts with briefly introducing some of the important questions in the catalysis research and the typical characterization methods used to study the catalysts. Chapter 2 dives into the fundamentals of XAS and the application of *in situ* XAS in catalysis. This information aims to help the readers gain an overview of the technique and the questions in catalysis it can answer. In Chapter 3, an example of *in situ* XAS studies of Pd(II)@MOFs catalysts mediating the Heck coupling reaction is illustrated. The work intents to elucidate the entire evolution of the Pd species which is then correlated to their catalytic actives. Chapter 4 discusses an *in situ* XAS investigation of a Pd(II) carbene complex supported on reduced graphene oxide (rGO) during an undirected C–H acetoxylation reaction. The transformation of the Pd species in the presence of an oxidant during the reaction is the focus of the study. A deactivation study of a heterogeneous Pd(II) catalyst using *in situ* XAS was followed and discussed in Chapter 5. The catalyst is comprised of Pd(II) complexes immobilized on amino-functionalized siliceous mesocellular foam, Pd(II)-AmP-MCF. The deactivation and activity prolongation mechanisms are explored. The synthesis of Pd(0)-AmP-MCF and a Pd(0) biohybrid catalyst are elucidated in Chapter 6 by *ex situ* XAS measurements. In the last chapter, the chemical element scope is extended to ruthenium. The goal is to determine the structures of the homogenous ruthenium catalyst and its intermediates during the activation process using *in situ* XAS.

2 X-Ray Absorption Spectroscopy and Its Application to *In Situ* Catalysis Studies

2.1 Fundamentals of X-ray absorption spectroscopy

2.1.1 Processes at X-ray radiation of matter

X-rays are a type of electromagnetic radiation with wavelengths typically ranging from 0.01 to 10 nm. They have been extensively applied in material sciences due to their suitable wavelengths for interactions with electrons in matters. Figure 2.1 summarizes the common interactions between X-ray radiation and matter exposed to it. X-ray scattering is one of the primary effects. X-ray diffraction (XRD) is based on this effect and is a widely used approach to determine the structure of crystalline matter at the atomic level.

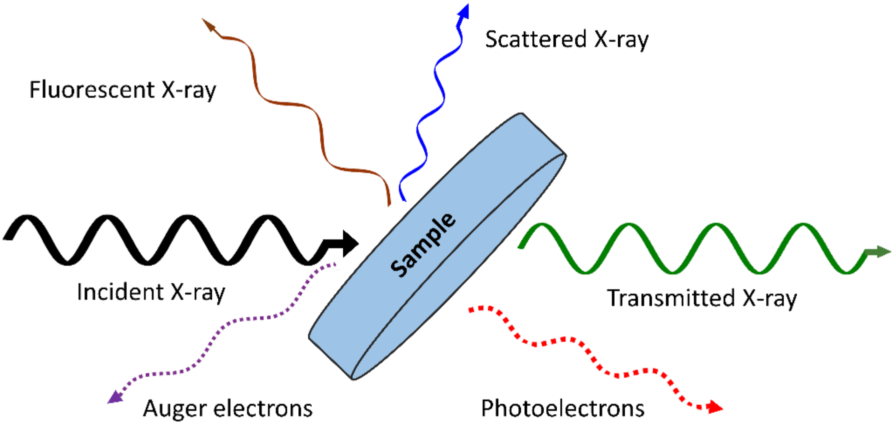

Figure 2.1. Typical effects when a matter is radiated by X-rays.

Another primary effect is the absorption of X-rays by matter. The absorption increases sharply at certain energies where the energy of the incident X-ray is sufficient to excite the ground state electrons to vacant electron-shells, or to the continuum generating photoelectrons and core-holes. The formed core-holes are filled through secondary processes resulting in the emission of fluorescent photons and Auger electrons. The electron transitions and the corresponding species generated are illustrated in Figure 2.2.

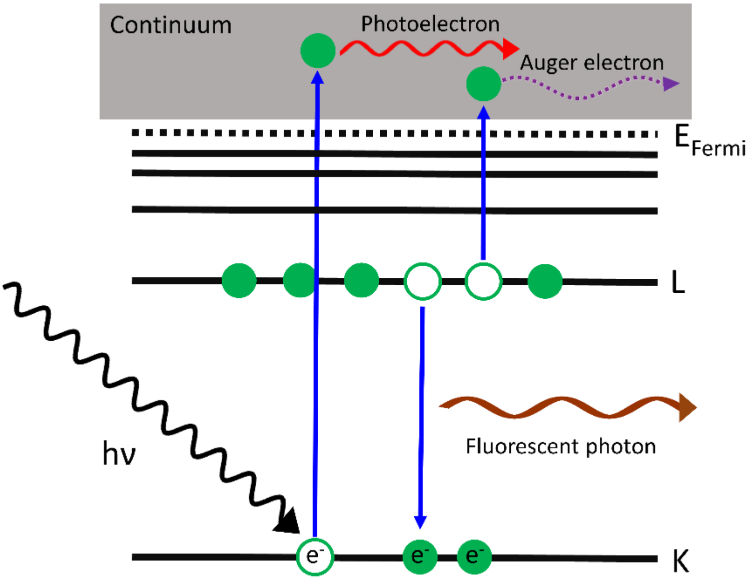

Figure 2.2. Electron transitions generating photoelectrons, fluorescent photons and Auger electrons.

2.1.2 X-ray absorption spectrum

The absorption of X-ray radiation by matter leads to attenuated transmitted radiation compared to the incident beam. For a path length of x, the relation of the incident beam I_0 and the transmitted beam I_1 can be expressed by the Beer-Lambert's law:

$$\ln(I_0/I_1) = \mu x \tag{1}$$

where μ is the linear absorption coefficient. There is a sharp increase of μ when the incident radiation has sufficient energy to excite the electron from an inner electron-shell to a higher vacant electron-shell or to the continuum. This sharp rise in μ is denoted as an absorption edge and its first inflection point is defined as the edge position. The minimum energy required to kick out a core-electron is denoted the threshold energy E_0. Due to the characteristic binding energy of electrons in different electron shells for each element, the absorption edge position is element specific. The difference between the incoming energy and the electron binding energy is the kinetic energy E_k of photoelectrons, which then travel in the interatomic space in the form of waves.

$$E_k = hv - E_0 \tag{2}$$

Figure 2.3 shows a Pd K-edge X-ray absorption spectrum of palladium foil after removal of the pre-edge background, where the correlation of X-ray absorbance and energy of the X-ray radiation is displayed. Only a minor part of the radiation is absorbed before the energy of the radiation is increased close to Pd K-edge. This is followed by a sharp rise in absorbance when the radiation starts to excite electrons at the ground states. The absorbance then oscillates as the energy further increases.

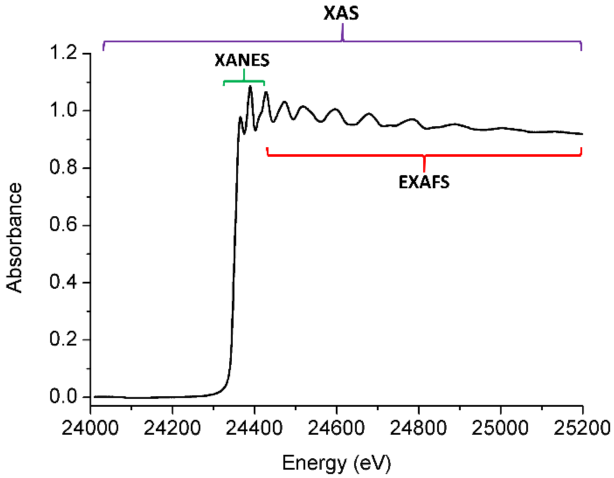

Figure 2.3. The X-ray absorption spectrum of palladium foil showing the different regions of the spectrum. The tabulated electron binding energy of 1s electrons in Pd is 24350 eV.[12]

The K-edge position of an XAS spectrum corresponds to the binding energy of electrons in the K shell of the absorbing atoms. For increasing atomic number there are electrons in the K, L, M, … shells and all the electrons can be excited to the continuum when absorbing X-ray radiation with the desired energy. Figure 2.4 elaborates the excitations of electrons at different electron orbitals and their corresponding absorption edges. For second row transition metals, K-edge (ca. 17–27 keV) is normally applied as the energy required is sufficient for the X-rays to penetrate the samples. L_{III} edge is suitable for elements with high atomic numbers, such as third row transition metals. X-rays that can excite electrons in 2p orbital (j=3/2) L_{III} have energies higher than 5 keV which can often penetrate the samples under normal conditions. Electrons in M orbitals or even higher have low electron binding energies. For that reason, they are normally not used in XAS experiments. In the X-ray data booklet[12] the electron binding and X-ray fluorescence energies of all elements are collected. These are of utmost importance when planning and perfoming XAS experiments.

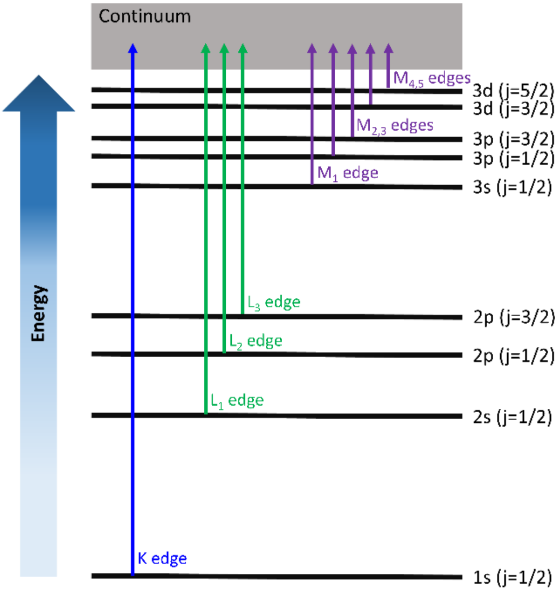

Figure 2.4. X-ray absorption edges and their electron transitions.

2.1.3 XAS experimental set-ups

Until now, synchrotron radiation sources are the most suitable light sources for standard XAS measurements due to the experimental requirements of broad energy ranges and high X-ray photon flux. Figure 2.5 describes the basic experimental arrangement for XAS measurements. The primary X-ray beam from the storage ring and the insertion device, normally a wiggler at XAS beamlines, is defined in size and shape by a set of slits and mirrors. XAS experiments are performed in the experimental hutch where the samples and detectors are located.

XAS experiments can be performed according to two principles, transmission and fluorescence. In the transmission mode, ion chambers are the detectors. They measure the intensities of the X-ray beam before (I_0) and after (I_1) the sample and also after the reference compound (I_2), as displayed in Figure 2.5. They consist of gas mixtures with controlled compositions. Ideally, ion chambers I_0 and I_1 should absorb respectively about 10–20% of the incident beam, while ion chamber I_2 can absorb the remaining radiation. A reference material containing the same element as the absorbing atom in the sample is placed between ion chambers I_1 and I_2, and is measured simultaneously with the sample. The purpose of using a reference is to calibrate the energy of the beam. A metal foil or powder of a pure non-metal element, has a well-defined absorption energy measured as the first inflection point on the edge.

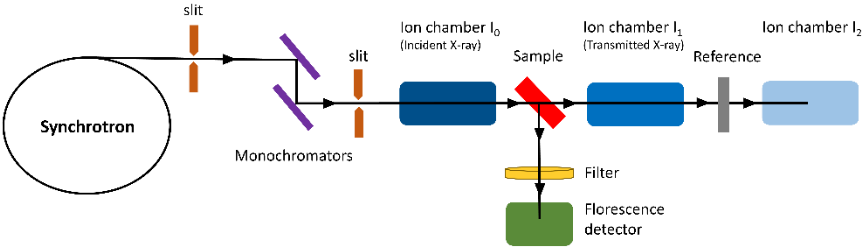

Figure 2.5. Schematic description of the experimental arrangement for XAS measurements.

The fluorescence generated by the relaxation of electrons to the core-holes is proportional to the X-ray absorption. Therefore, fluorescence signals can also be used in XAS measurements. The experimental set-up in fluorescence mode requires ion chamber I_0 to measure the intensity of the incident beam, and a fluorescence detector, such as a Lytle detector (also an ion chamber with a highly absorbing gas or gas mixture) or a solid state detector, is placed perpendicular to the ion chambers alignment, as illustrated in Figure 2.5. Due to the significant noise produced by the elastic and Compton scattering, an X-ray filter is applied to diminish the scattered photons before they enter the fluorescence detector. The criteria of choosing a suitable filter is that the K or L edge of the element in the filter should be at the energy position where it can absorb most of the photons from the elastic scattering and Compton scattering. Usually the element in the filter should have one or two atomic numbers lower than the absorbing element in the sample. For example, when the absorbing element is palladium ($K\alpha_1$ = 21.177 keV)[12] in the sample, ruthenium (K 1s = 22.117 keV)[12] is the ideal filter. The sample is preferably positioned 45° to the incoming beam in order to maximize the signal to the fluorescence detector. Normally, simultaneous measurements in both transmission and fluorescence modes are performed.

2.1.4 Samples

The samples for XAS measurements can be in all physical phases: solid, liquid or gas. The data quality of an X-ray absorption spectrum is affected by the sample preparation. For the data collection in transmission mode, the optimal signal-to-noise (S/N) ratio is achieved when absorbance is between 0.5 and 1.5, which is determined by the thickness of the sample and concentration of the absorbing element. For solid samples, it is advantageous to grind them into fine powders, and, in most cases, it is necessary to dilute samples with boron nitride (BN) to achieve suitable absorbance. Samples should be as homogenous as possible to ensure they have equal absorption throughout and to therefore avoid the so called pin-hole effect. Pressing solid samples into sample holders can help to maintain this. Fluorescence measurements are particularly suitable for diluted samples, where the applied concentrations can be as low as 1 mM for first row transition metals in solution.13 Guest atoms imbedded in a solid matrix with low weight percentages (<1 wt%) are also favorable for fluorescence measurements.

For *in situ* XAS experiments, it is generally more complicated to prepare the samples and the data quality is often worse than the properly prepared ex situ samples. Fortunately, due to the development of *in situ* reactors and increased quality of photon sources, decent data can now be collected *in situ*. *In situ* XAS experiments are further discussed in detail in Section 2.4 of the thesis.

2.2 X-ray absorption near edge structure (XANES)

2.2.1 Theory and applications of the main absorption edge

As shown in Figure 2.3, X-ray absorption spectroscopy (XAS) consists of two parts: X-ray absorption near edge structure (XANES), which is also known as near-edge X-ray absorption fine structure (NEXAFS), and extended X-ray absorption fine structure (EXAFS). The energy range of a XANES spectrum is defined relatively loosely and it typically refers to the absorbance of photons from around 10 eV below the absorption edge, where the pre-edge shall be included, to 50-200 eV above the absorption edge. When the oxidation state of an element increases, the binding energy of the electron will increase. Hence, the energy required to excite the electron will also increase leading to an edge shift towards higher energy. This property makes XANES sensitive to the oxidation state of an element, and it is therefore used to estimate the oxidation state of the absorbing atoms in a sample by observing the edge positions. Figure 2.6 shows the Pd K-edge XANES spectra of Pd(0), Pd(II) and Pd(IV) in Pd foil, $(CH_3CN)_2PdCl_2$, and K_2PdCl_6, respectively. It clearly shows that the Pd K-edge shifts towards higher energies as the oxidation state of Pd increases.

The edge of a XANES spectrum is followed frequently by a sharp and intense peak which is called a "white line". Its formation is attributed to the high probability of electrons being excited to electron orbitals close to the continuum. The number of orbitals close to the continuum is larger than orbitals at lower energy levels and they have smaller energy differences. This phenomenon can also be reflected in Figure 2.4. Therefore, the absorbance becomes more significant at the white line.

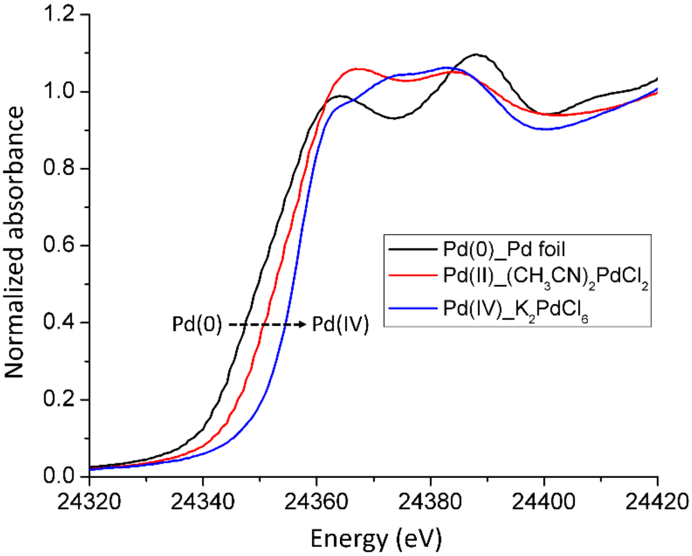

Figure 2.6. Normalized Pd K-edge XANES spectra of Pd(0), Pd(II) and Pd(IV) in selected Pd compounds. The data were collected at BM01 (SNBL), European Synchrotron Radiation Facility (ESRF).

When the energy is higher than the white line position, the near edge region is reached where photoelectrons are generated. They are ejected from the absorbing atoms, travel in the interatomic space, and "meet" the electrons surrounding the absorbing atoms. The photoelectrons will either be backscattered directly to the absorbing atoms or scattered to other atoms before returning to the absorbing atoms. These two principle paths are known as "single backscattering (SS)" and "multiple scattering (MS)", respectively, and they are schematically described in Figure 2.7. Multiple scattering is the dominating process in the XANES region after the absorption edge. It involves more than one scattering atom and there are various scattering paths. Scattering atoms arranged in different geometries around the absorbing atom, such as square-planar and tetrahedral, result in different multiple scattering paths with different distances for the photoelectrons to travel and return back to the absorbing atoms. Therefore, XANES spectra are sensitive to the geometry of scattering atoms. A XANES spectrum is a fingerprint for a specific local environment of absorbing atoms, as demonstrated in Figure 2.6.

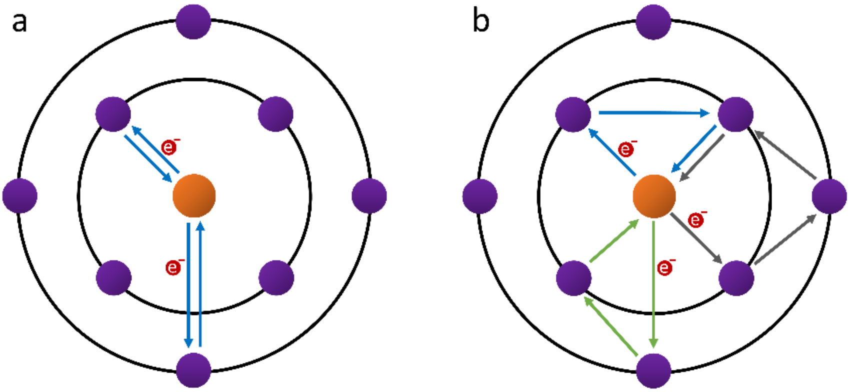

Figure 2.7. Scheme of photoelectron scattering paths among the absorbing atoms and neighboring atoms: (a) single backscattering and (b) multiple scattering processes.

2.2.2 Pre-edge features

For some elements with vacancies on 3d or 4p orbitals, a relatively weak pre-edge peak may appear in the region before the main absorption edge in the XANES spectrum. Figure 2.8 shows the pre-edge features of titanium and vanadium K-edge XANES spectra of anatase (TiO_2) and vanadium dioxide (VO_2). The Ti pre-edge peak at ca. 4974 eV is commonly attributed to the 1s → 3d electron transition,[14] while the V pre-edge peak at ca. 5471 eV is mainly attributed to the 1s → 4p transition.[15] Pre-edge peaks can provide very useful structural information about coordination number and geometry. For instance, the higher intensities of pre-edge peak before Ti K-edge indicates lower coordination numbers of oxygen to Ti(IV).[14,16] In the case of Cu(I), the shape and intensity of the pre-edge peak at ca. 8980 eV correspond to different coordination numbers and geometries.[17]

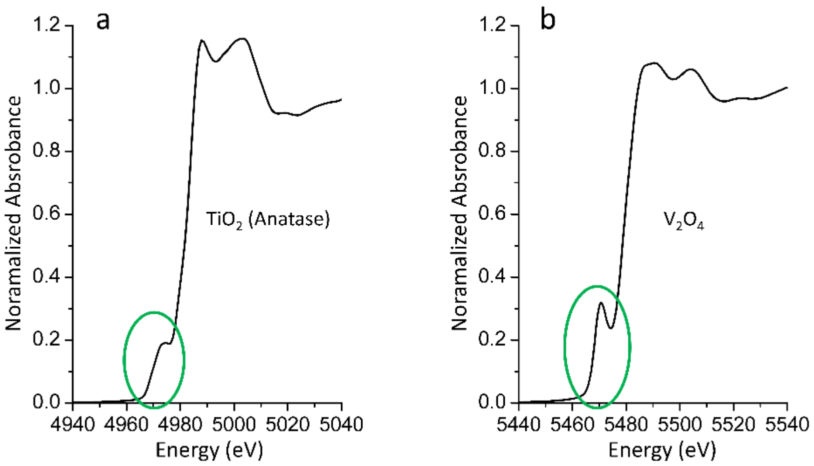

Figure 2.8. Ti and V K-edge XANES spectra with their pre-edge peaks marked by green circles. Data were collected at beamline I811, Max-Lab II, Lund, Sweden.

2.3 Extended X-ray absorption fine structure (EXAFS)

2.3.1 Theory

The region of the X-ray absorption spectrum after XANES and towards higher energies is called extended X-ray absorption fine structure (EXAFS) (Figure 2.3). This region is defined by X-ray radiations of energies from ca. 50 eV above the threshold energy E_0, to more than 1000 eV. Photoelectrons are produced in this region and the single backscattering process illustrated in Figure 2.7a is the dominant contribution to the EXAFS signal. Multiple scattering processes have minor contributions, however, 3-leg MS scattering or 4-leg MS with a linear or near linear geometry can generate significant contributions to the EXAFS. During the scattering events of photoelectron waves, the outgoing photoelectron waves are backscattered by atoms around absorbing atoms, so called “backscattering atoms”. Due to the wave nature of the photoelectrons, the outgoing photoelectrons and backscattered photoelectrons interfere with each other. During an EXAFS measurement, the kinetic energy of the photoelectrons keeps increasing as the energy of the incident beam increases. This means that wavelengths of outgoing and backscattered photoelectrons become increasingly shorter with increasing excitation energy. During this process, constructive and destructive interference between the outgoing and the backscattered photoelectron waves occurs, which alternate as the energy of incident beam increases. Figure 2.9 schematically visualizes this phenomenon.

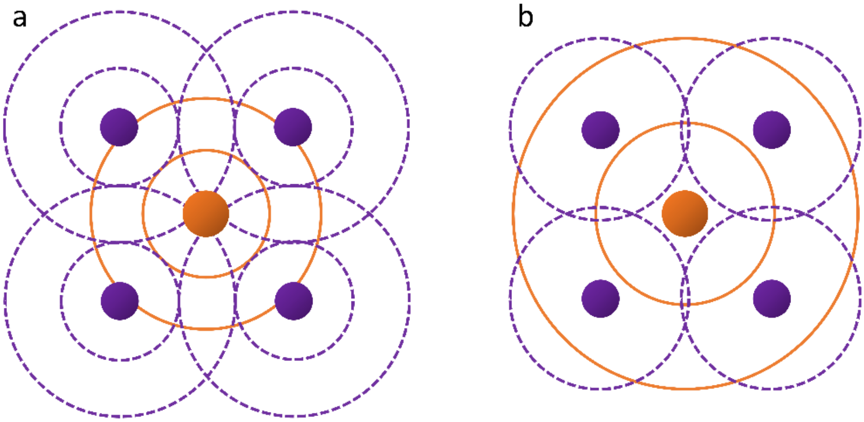

Figure 2.9. Schematic illustration of (a) constructive and (b) destructive interferences between outgoing (solid orange rings) and backscattered (broken purple rings) photoelectron waves. The orange circles indicate absorbing atoms, and the purple ones are as backscattering atoms.

The electron density of absorbing atoms varies according to the interference of the photoelectrons, which creates systematic changes in absorbance. Constructive interference increases the electron density, leading to a higher probability of absorbing photons, while destructive interference has the opposite effect. This variation in absorption with increasing energy is the fundament of EXAFS.

In order to deduce the EXAFS equation, the energy of X-ray radiation is converted to the wave vector, k, with a unit of Å^{-1}. It is obtained from:

$$k = \sqrt{\frac{2m_e(E - E_0)}{\hbar^2}} \qquad (3)$$

where m_e is the mass of electron, $E - E_0$ is the kinetic energy of the photoelectron, and $\hbar$ is the Dirac constant.

A factor $\chi(k)$ is introduced which represents the fractional variation in the absorption coefficient as a function of the wave vector, k. $\chi(k)$ is commonly referred as “the EXAFS function”, and it has oscillatory features which decay considerably with increasing k. To magnify the oscillations, $\chi(k)$ is usually multiplied by k^2 or k^3. Some structural information can be directly extracted from the appearance of $\chi(k)$, and Figure 2.10 shows some examples of this. The position of the maximum amplitude of the envelope (the overall shape of the EXAFS function) shifts towards higher k values when the atomic number of backscattering atoms increases. This phenomenon is demonstrated in Figure 2.10a–c when the atomic number of the backscattering atoms increases from

7(N) to 46 (Pd). Another useful observation is that the increase in frequency of the EXAFS spectrum indicates a longer distance between the absorbing atom and backscattering atom in a single scattering as shown in Figure 2.10, or a longer path length in the multiple scattering.

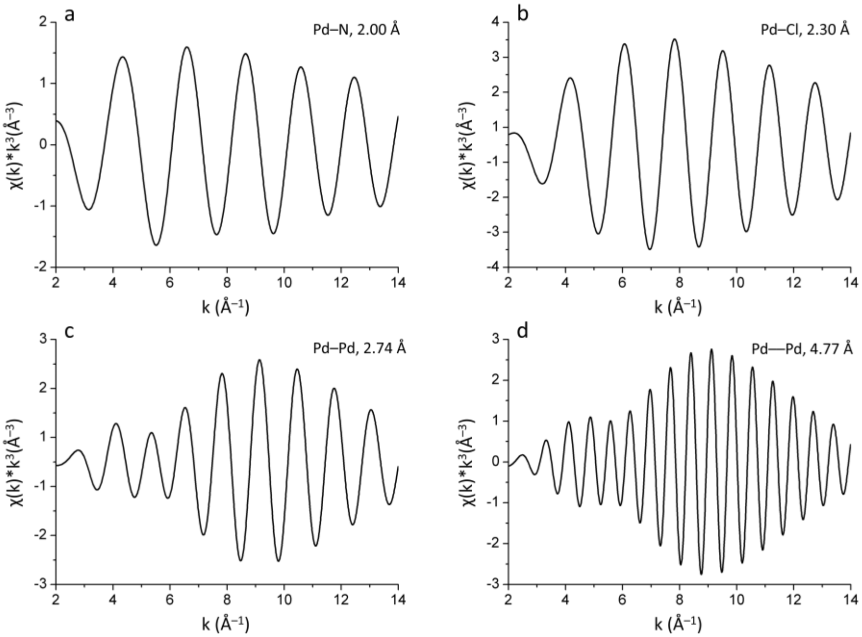

Figure 2.10. Theoretical Pd k^3-weighted EXAFS spectra of various single scattering: (a) Pd–N, (b) Pd–Cl, and (c,d) Pd–Pd with different scattering path lengths. The figure demonstrates the correlations between the features of EXAFS spectra (frequency and envelop) and the nature of the backscattering atoms and the scattering path lengths.

Through a series of deductions, the EXAFS equation is expressed as:

$$\chi(k) = \sum_j \frac{N_j S_0^2(k)}{k R_j^2} \left| f_{eff}(k) \right|_j \exp\left(-2k^2\sigma_j^2\right) \exp\left(\frac{-2R_j}{\lambda_k}\right) \sin\left[2kR_j + \phi_{ij}(k)\right] \tag{4}$$

i: Absorbing atom

j: A specific coordination shell of the absorbing atoms where the scattering atoms are identical and have about the same scattering path.

N: Coordination number

R: Distance between the absorbing atom *i* and backscattering atom in the *j* shell in single scattering, or half of the total path length in multiple scattering

S_0^2: Many-body amplitude reduction factor
f_{eff}: Photoelectron scattering amplitude
σ^2: Mean-square disorder in the distance of R
λ: Photoelectron inelastic mean free path
ϕ: Phase shift induced by the coulomb potential of the absorbing atom *i* and backscattering atom in the *j* shell

2.3.2 Data treatment and analysis

EXAFS data provide local structure information of the absorbing atoms, and require data processing. Several computer programs have been developed to treat EXAFS data, such as Demeter,[18] Larch,[19] VIPER,[20] and EXAFSPAK.[21] Figure 2.11 describes the general procedures of the data treatment.

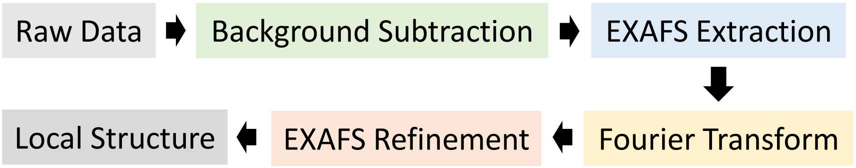

Figure 2.11. General procedure of EXAFS data treatment.

In this thesis, all the EXAFS spectra were processed by the EXAFSPAK package. The background subtraction is the first step of the data treatment. This step corrects the effects of the undesirable atoms and their electrons (total absorption), including the absorbance of the sample cell windows. It consists of pre-edge subtraction and spline removal. The first process is fairly straight forward, while the spline removal process plays a crucial role in extracting a reliable EXAFS spectrum. The $\mu_{spline}(k)$ function is approximated $\mu_0(k)$ and it corresponds to the X-ray absorption of the "isolated" absorbing atom. EXAFS equation can therefore be expressed as:

$$\chi(k) = \frac{[\,\mu_{data}(k) - \mu_{spline}(k)]}{\mu_{spline}(k)} \qquad (5)$$

Parameters, such as the region for spline subtraction, the order of the spline and the number of data points, significantly influence the resulting spline. After the background subtraction, the EXAFS data can be extracted which is in reciprocal space. Fourier transformation of the EXAFS data is then performed to convert the data into real space. In order to extract useful structural information, the experimental k^3-weighted EXAFS oscillations are analyzed by non-linear least-squares refinements of the data to the EXAFS equation. Refinement of model parameters is then performed, including number of backscattering atoms or specific scattering paths (*N*), mean interatomic distances or half of the total path length in multiple scattering (*R or d*), Debye-Waller factor coefficients (σ^2) and threshold energy (E_o). The standard deviations of the refined parameters are obtained from the refinement. The *ab initio* program package FEFF7 is used to calculate the theoretical phases and amplitudes.[22] A reasonable fit between the experimental data and the EXAFS function with the refined structure parameters can provide reliable local structure information of the absorbing atom. It should be noted that the distances read in Fourier transformed EXAFS spectra are not phase corrected (*ϕ in Equation 4)*. The true distances are determined from the EXAFS refinements. For a well-defined interaction, the accuracy of the distances given for an individual complex is between ±0.005 and ±0.02 Å. The EXAFS spectrum of solid palladium acetate and its Fourier transformed spectrum are displayed in Figure 2.12 as an example.

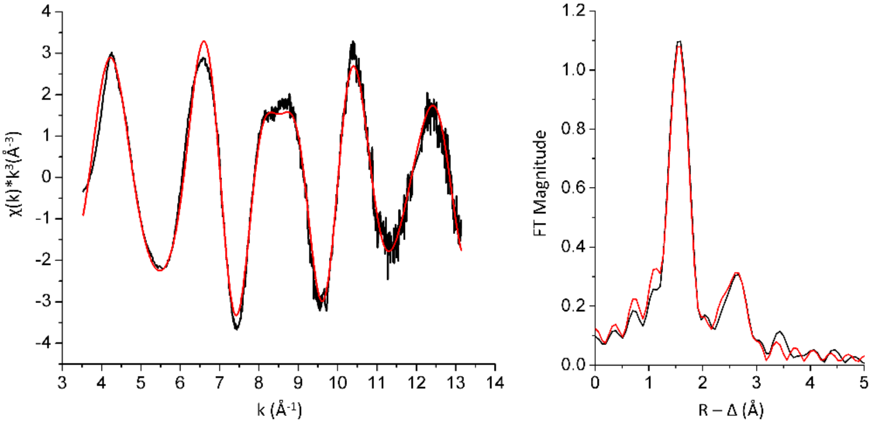

Figure 2.12. Pd K-edge k^3-weighted (left) EXAFS spectrum of $Pd(OAc)_2$, and (right) its Fourier transformed spectrum without phase correction, black curve – experimental, red curve – model. Data were collected at BM01 (SNBL), European Synchrotron Radiation Facility (ESRF).

2.4 *In situ* XAS and its application in catalysis

2.4.1 The interest of *in situ* XAS

During a chemical reaction, the species of interest often go through one or more transformations. The standard *ex situ* characterizations are limited in providing insights into such transformations leading to insufficient understandings or sometimes inaccurate interpretations of reaction mechanisms, which has raised the demand for *in situ* characterizations. Thanks to the development of synchrotron facilities, *in situ* XAS measurements have become more feasible. Experiments can be performed in various reaction environments following changes in the valence state and local structure of the absorbing atoms. In theory, the time for acquiring one full XAS spectrum in a state of the art beamline can be reduced to only a few seconds using the quick scan or energy dispersive technique. Certain compromise on time resolution is often necessary to acquire data with reasonable S/N ratio. The reaction system itself has a significant impact on data collection, and a good understanding of both the chemistry of the reaction and the XAS measurement always play a key role in a successful experiment.

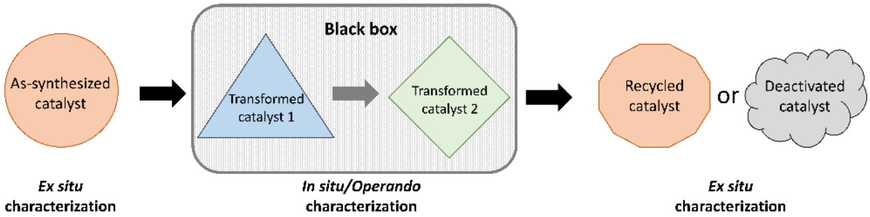

Figure 2.13. Schematic illustration of possible catalyst transformation over the course of a catalytic reaction and the corresponding characterization methods. The distinctive shapes represent different forms of the catalyst at different stages of the reaction.

Catalysis is one of the areas in chemistry where *in situ* XAS is particularly useful.[23–28] Knowledge of speciation and structure of the active catalyst during a reaction is crucial in understanding their behavior and acquiring information about the reaction mechanism. This information can not only shed light on reaction mechanism, but also provide opportunities to develop new catalysts with higher activities and longer lifetimes. Figure 2.13 schematically describes the possible transformations of a catalyst from its as-synthesized form until the end of the reaction. The “starting” and “ending” points are fairly easy to characterize by *ex situ* approaches, yet the forms of the catalyst during the reaction remain hidden in a “black box”, here *in situ* methods are desired.

2.4.2 *In situ* XAS in solid-gas based catalytic reactions

The great demand for understanding catalysts under certain reaction conditions has promoted the design and fabrication of various *in situ* cells based on the specific reaction conditions required. In recent years, a lot of work has been focused on solid-gas heterogeneous catalytic systems, such as the Fischer-Tropsch process.[29–33] This is mostly because the design and construction of *in* *situ* cells for solid-gas heterogeneous systems are relatively simple. Another reason is that such cells are suitable for a wide range of elements. Their design is typically based on the gas-flow setup,[34] and is schematically illustrated in Figure 2.14. The solid catalyst is packed tightly in the middle part of the capillary. The inlet of the reactor is connected to one or several gas sources which allows reactants to flow into the capillary, make contact with the catalyst and react. Usually, a capillary reactor can retain a higher pressure, for example 20 bar (1 bar = 100 000 Pa), with finely controlled working temperature of up to a few hundred degrees Celsius.[35]

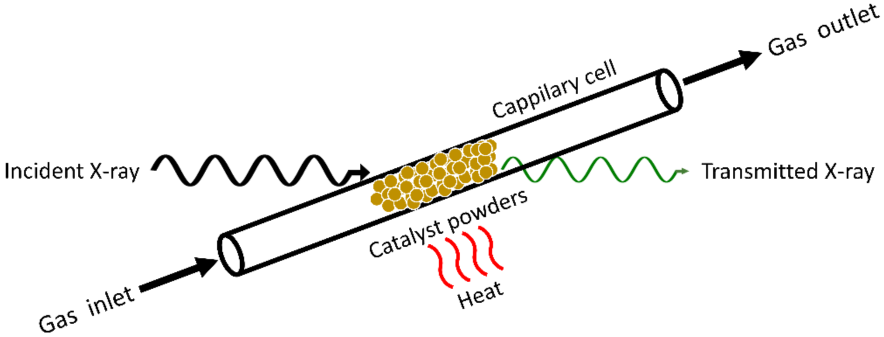

Figure 2.14. Typical design of a capillary cell for *in situ* XAS measurements of solid catalysts during solid-gas heterogeneous catalytic reactions.[25]

2.4.3 *In situ* XAS in suspension/solution based catalytic reactions

Solid-liquid heterogeneous reactions and liquid homogeneous reactions are also important types of catalytic systems, such as palladium catalyzed carbon-carbon coupling reactions. However, the status of the catalyst during these reactions has been explored considerably less in comparison to solid-gas systems. This is mainly due to the generally complex design and manufacture of suitable *in situ* reactors, as the reaction conditions are more demanding. Usually a mixture of several components are involved, for instance, substrate, solvent, acid/base, and the catalyst, which either dissolves or remains as a separate phase. In addition, proper stirring and a volume of several mLs, as well as the ability to withstand hydrothermal conditions, are key requirements for a reactor. Therefore, it has been fairly challenging to construct a reactor which meets these requirements and collects *in situ* XAS data with reasonable S/N ratio. Despite these demands, a few well-working *in situ* reactors have been reported based on sophisticated design and good control of the chemical conditions. Generally, they can be classified into flow reactors,[36–38] and batch reactors[39,40] using either the transmission mode[38,40] or the fluorescence mode of the XAS measurement[36,37]

The main focus in this thesis is the solid-liquid heterogeneous and liquid homogeneous catalytic systems using *in situ* XAS as the main approach to probe the catalytic species over the course of the measurements.

2.4.4 *In situ* reactor used in the thesis

A custom-made reactor shown in Figure 2.15 was utilized for all the *in situ* XAS and PXRD measurements discussed in this thesis.[40] The reactor was developed at the Christian-Albrechts University (Kiel, Germany) in collaboration with the beamline staff at the P08 beamline, PETRA III, DESY (Hamburg, Germany). The reactor was originally designed to study the synthesis of metal-organic frameworks (MOFs) under solvothermal conditions by PXRD. It was realized later that the rector could also be used as a batch reactor for XAS measurements of the catalytic reactions, which evoked much interest and opened up many opportunities.[41]

The reaction vessel is a 6 mL Duran glass vial with a 10 mm inner diameter and 1.0 mm wall thickness. The vial is held in an aluminum casing, which is wrapped by a heating mantle made by copper wires. The targeted working temperature can be achieved within one minute, and then stabilized by a combination of resistive heating and cooling with compressed air. A PTFE-coated thermocouple is used to monitor the temperature of the reaction mixture continuously. The temperature is remotely controlled by a computer program. The reaction mixture is homogenized by stirring a magnetic bar placed at the bottom of the vial and the magnetic field is generated under the base of the aluminum casing. In order to start a chemical reaction or alter the chemical conditions during the measurement, there are two tubes embedded into the cap of the reactor. They are connected to two 5 mL glass syringes operated by a NEMESYS syringe pump. This setup allows the remote controlled introduction of reagent or another chemical at suitable timing to study the catalyzed reaction. The windows on the protective cage, the heating mantle and the aluminum casing allow standard transmission XAS experiments. X-ray beams with relatively high energies are preferred in order to effectively penetrate the glass walls of the vial and the reaction mixture. Up to the preparation of this thesis, the K-edge XAS spectra of several elements in the second row of the transition metals have been collected using this reactor, such as zirconium (Zr), molybdenum (Mo), ruthenium (Ru) and palladium (Pd). *In situ* XAS data with sufficient quality for analysis were acquired.

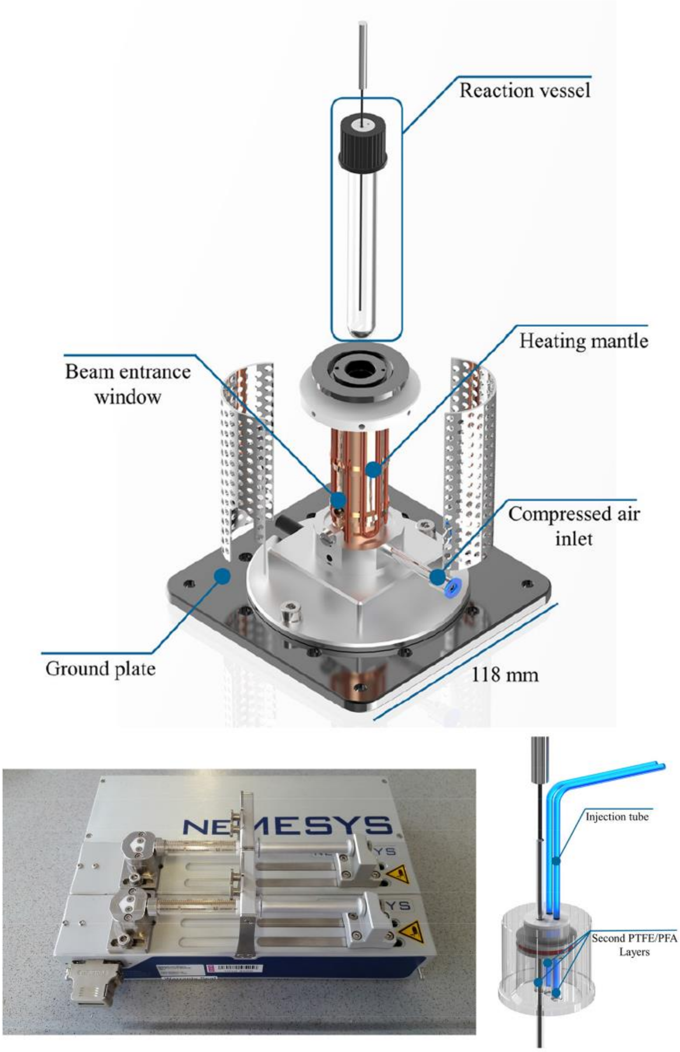

Figure 2.15. Exploded-view illustration of a custom-made reactor for *in situ* XAS. (Reprint with permission from *Rev. Sci. Instrum.* 2017, 88 (10), 104102. Copyright 2017, AIP Publishing.)

2.4.5 Combinations of *in situ* XAS and other techniques

In many recent *in situ* studies of catalytic processes, XAS is also often combined with other techniques and measured simultaneously to gain a more thorough understanding of the catalyst and the reaction.[27] Each technique has certain advantages when studying specific aspects of catalysis, as well as limitations. Figure 2.16 shows some of the *in situ* techniques that can be coupled with XAS.

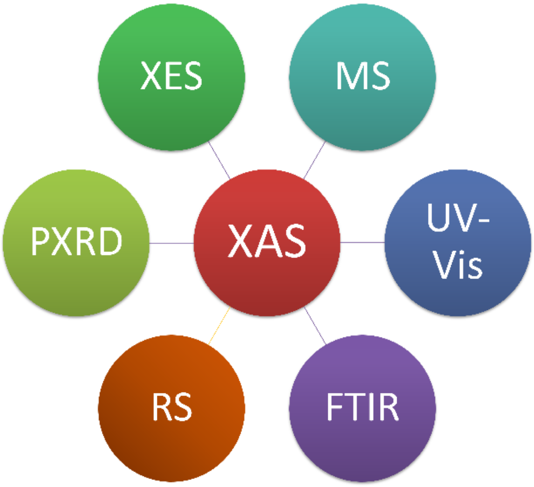

Figure 2.16. Examples of the *in situ* techniques that can be combined with XAS. (PXRD, Powder X-ray diffraction; FTIR, Fourier transform infrared spectroscopy; MS, mass spectrometry; XES, X-ray emission spectroscopy; UV-Vis, Ultraviolet-visible spectroscopy; RS, Raman spectroscopy)

Powder X-ray diffraction (PXRD) is a useful co-technique to XAS in the case of crystalline heterogeneous catalysts. It can monitor the crystallinity of catalysts, catalyst supports, or formation of new crystalline species during reactions.[33,41–43] The harsh reaction conditions may trigger changes in crystallinity and crystalline phase. This information is important for understanding the activity and recyclability of catalysts. The reactor in Figure 2.15 can be used for such purposes if experimental set-ups for both XAS and PXRD are available, and exchange between the detectors is quick, for example, as at beamlines BM01, at the ESRF, Grenoble, France,[35] and beamline P64 at the Petra III Extension, DESY, Hamburg, Germany.[44]

Fourier transform infrared spectroscopy (FTIR) is another spectroscopic method that can be operated in an *in situ* manner and is often coupled with XAS in catalysis research. It is an important analytical method to identify chemical bonds. For example, it is used to probe the adsorbed gas reactant species, such as carbon monoxide, on the metal catalyst or the catalyst support during a gas-solid heterogeneous reaction.[45–51]

To detect the product of a catalytic reaction in real time, mass spectrometry (MS) can be attached to an XAS experiment. Normally, it is applied in the solid-gas catalytic systems where the generated products flow out through the outlet of the reactor and are quantitatively examined directly.[50,52–55] The conversion rate of the reactants to products can be correlated to the activity of the catalyst species at a specific stage of the reaction.

X-ray emission spectroscopy (XES) is a so-called photon-in - photon-out element-specific technique. The energy dependence of emitted photons is the base of XES analysis. XES provides important information about the electronic structure of the element studied and the nature of the bound ligands, for instance, XES can distinguish carbon, nitrogen and oxygen ligands bound to a metal center of interest, which can be difficult by XAS as the bond distances are small and their backscattering abilities are almost the same. These properties make XES very useful in catalysis investigations.[23] Many of the state of the art XAS beamlines, such as beamline Balder at MAX IV, Lund, Sweden,[56] will be equipped with XES detectors, which makes it possible to measure XAS and XES simultaneously.

Furthermore, *in situ* techniques like Raman spectroscopy (RS) and ultraviolet-visible spectroscopy (UV-Vis) are also helpful in the study of catalysis due to their high sensitivity to molecules and transition metal ions.[31,48,57,58]

2.5 Strategies of the XAS data collection, treatment and evaluation in this thesis

2.5.1 *In situ* data collection

As discussed above, data quality can be an issue when conducting *in situ* XAS measurements on suspension based catalytic reactions. To be able to conduct successful experiments, modification of the experiment conditions and compromise on different measurement parameters become necessary.

The concentration of the absorbing element was typically increased to improve S/N ratio in comparison to standard laboratory experiments. However, the capacity of loading metal species onto catalyst support is often limited and a large amount of solid catalysts can also cause a stirring problem. Therefore, a balance of different measurement parameters was normally necessary, such as the integration time at each energy step, the time resolution and the reaction time. As both XANES and EXAFS data were utilized in our studies, one full EXAFS scan was recorded before starting the next one. Considering that the reactions studied in this thesis take one hour or more and the influence of the integration time for the counting statistics, a full XAS scan (800-1000 eV) was normally collected in 3.5–6 min.

The constantly upgrading beamline facilities will allow us to conduct *in situ* measurements that are applicable to reaction systems requiring higher time resolution.

2.5.2 *In situ* data treatment

For an entire *in situ* measurement, it was relatively rare that all EXAFS spectra were of sufficient quality to be treated. XANES spectra, on the other hand, could be used to fill the "gap". One example is Pd@MOF catalyzed Heck reaction which is elaborated in Chapter 3. During the heating ramp, several of the EXAFS spectra became too noisy to be treated. However, their XANES spectra could be compared during this "noisy" stage and they overlapped well on top of each other. This means that local structures of the absorbing atoms were comparable and the treated EXAFS spectra should be able to reflect the untreatable ones.

Another strategy dealing with noisy data is averaging a few *in situ* scans to improve the S/N ratio. This can be applied to reactions where the local structures of the absorbing atoms alter slowly enough for a set of scans to be considered as the same. One example is supported Pd complexes catalyzed undirected C–H acetoxylation reaction in Chapter 4. The loading of the Pd is low with regard to *in situ* measurement. However, since the change of Pd species was sufficiently slow, a set of EXAFS spectra were averaged and the resulting data were then treated.

2.5.3 A "true or false" question in data evaluation

Satellite peaks are known as a feature in the Fourier transformed data of the EXAFS spectra, and they appear at shoulder positions of the main peaks of single scatterings. Satellite peaks become disturbing if there are multiple distinct ligands bound to absorbing atoms. For example, the peak corresponding to Pd–Cl happens to be at the position of the satellite peak of Pd–Pd. In such case, it becomes necessary to be able to identify if the peak is a pure satellite peak or if it contains information about the Pd–Cl bond. To understand this question, the factor that determines the shape and intensity of the satellite peaks needs to be explored. Figure 2.17 shows Fourier transformed EXAFS data of palladium foil. The k ranges chosen for the Fourier transform are (a) 2–13, (b) 2–11 and (c) 2–9 Å^{-1}. The prominent peak in each figure corresponds to Pd–Pd single scattering, and the "shoulder" on the left side is the satellite peak. It can be clearly seen that as the applied k range decreases, this satellite peak becomes more pronounced.

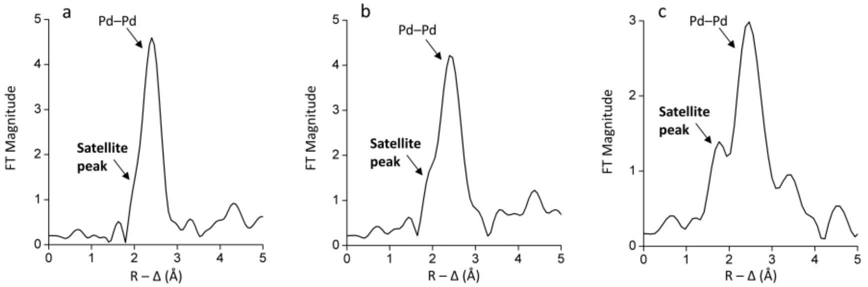

Figure 2.17. Fourier transformed k^3-weighted EXAFS spectra of palladium foil using different EXAFS ranges (a) 2–13, (b) 2–11 and (c) 2–9 $Å^{-1}$. The Fourier transformed EXAFS data are not phase corrected. (Reprinted with permission from *J. Am. Chem. Soc*. 2018, 140 (26), 8206–8217. Copyright (2018) American Chemical Society.)

With this knowledge, one can estimate if a peak is a pure satellite peak of a strong single scattering or if it is comprised of another contribution. In Chapter 3 Pd@MOFs were used to catalyze the Heck reaction. At a later stage of the *in situ* measurement, a distinct peak at ca. 1.9 Å was detected. The first impression was that it consists of Pd–Cl in addition to the satellite peak of Pd–Pd. To further confirm if there were Pd–Cl bonds, the experimental data were fit with and without a single scattering between Pd and Cl. The EXAFS range used to perform Fourier transform was varied as well. Figure 2.18a-b compares the fit of Fourier transformed data when the EXAFS range is set at 2.5–12.0 $Å^{-1}$. Obviously, the introduction of Pd–Cl single scattering leads to a noticeable improvement in the fit and the differences are marked by green circles. The EXAFS range was then decreased to 2.5–10.0 $Å^{-1}$. Besides the more prominent peak at ca. 1.8 Å, the fit was also improved when including Pd–Cl single scattering as can be seen in Figure 2.18c-d. To make our conclusion from EXAFS analysis more reliable, inductively coupled plasma atomic-emission spectroscopy (ICP-OES) was used. Not only was the presence of Cl confirmed, the calculated molar ratio of Pd/Cl was also consistent with the refinement result of EXAFS. At this point, it was concluded that it is TRUE that there are Pd–Cl bonds in the catalyst.

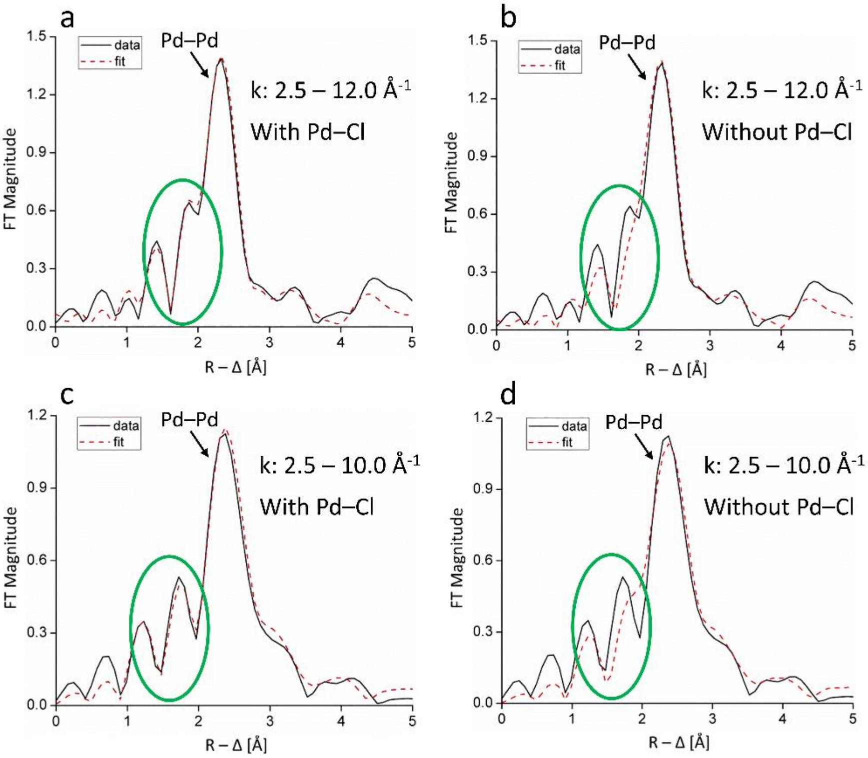

Figure 2.18. Fitting results of Pd K-edge EXAFS spectra and the corresponding Fourier transform at 85 min of the *in situ* measurement, (a-b) using an EXAFS range of 2.5–12.0 Å^{-1} with (a) and without (b) Pd–Cl single scattering in the refinements, (c-d) using an EXAFS range of 2.5–10.0 Å^{-1} with (c) and without (d) Pd–Cl single scattering in the refinements. The Fourier transformed EXAFS data are not phase corrected. (Reprinted with permission from *J. Am. Chem. Soc*. 2018, 140 (26), 8206–8217. Copyright (2018) American Chemical Society.)

2.5.4 The importance of chemical insights in EXAFS data evaluation

The structural information from EXAFS data is in one dimension and is an average of the irradiated part of the sample. When extracting structures in three dimensions, there is a risk that multiple models can fit the spectra. The *in situ* measurement of Pd@MOF catalyzed Heck reaction in Chapter 3 is a good example of this risk. When the Pd nanoclusters were formed from the mononuclear Pd complexes, there were two scenarios that could be derived from the fit of the EXAFS spectra. The first scenario being that all the complexes transformed into clusters instantly, and the enhancing signal of Pd–Pd was explained by a gradual growth of the average particle size. The scenario is a continuous transformation of the complexes into clusters, and the average size of the clusters was relatively stable. The chemical understanding of the reasonable behaviors of the Pd atoms was considered in order to deduce the correct outcome. First, there was no obvious driving force in the reaction system that could trigger an instant altering of the Pd complex into metallic clusters within one XAS scan (ca. 3.5 min). It would also be difficult for the Pd atoms to retain as a dimer (or trimer) during the data collection as these species were expected to be unstable in air, due to their small size and lack of ligands that can enhance stability, such as phosphine ligands.[59–61] These reasons help to exclude the first scenario. A continuous transformation from one species to the other, therefore, is more reasonable.

Another risk occurs when identifying ligands with similar atoms bound to the absorbing atoms. For example, a typical EXAFS spectrum cannot distinguish if a single scattering is between Pd and O or Pd and N. However, the same work used in Chapter 3 was used to elucidate the bonding situation. At the beginning of the *in situ* measurement, the two Cl^- ligands bound to Pd were replaced by other ligands. The bond distances suggested that substituted ligands should be N or O, and they both were available in the reaction mixture. The solvent of the reaction is comprised of H_2O and dimethoxyethane (DME). The existence of H_2O made it possible to take advantage of the stability constants of Pd–Cl, Pd–N and Pd–O to provide insights into the changes in the binding ligands to Pd. It was found that ligands binding through nitrogen atoms to Pd(II) were significantly more stable than chloride complexes, which in turn were more stable than complexes with ligands binding through oxygen. This relationship explains why Pd–Cl was replaced in the first place, and why Pd would prefer N–ligands instead of O– ligands.

There are more discussions in the following chapters where the chemical knowledge of catalysis was used when interpreting the EXAFS data to gain a more accurate understanding of the catalytic species.

3 Probing the Evolution of Palladium Species in Pd@MOF Catalysts Mediated C–C Coupling Reactions by *In Situ* XAS (Paper I)

3.1 Palladium supported in metal-organic frameworks

Metal-organic frameworks (MOFs), also referred to porous coordination polymers (PCP), are a large class of crystalline porous materials that are constructed from metal ions/clusters and organic linkers.[62–67] The high porosity, enormous internal surface area, together with the exceptionally wide choices of both the inorganic and organic building components, have imparted great potentials of MOFs in applications including gas storage/separation, catalysis and sensing.[68–70]

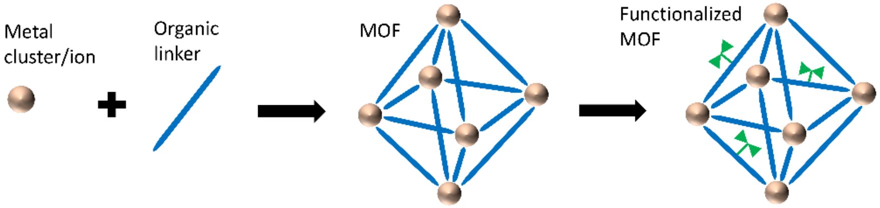

Figure 3.1. Schematic illustrations of MOF synthesis, and an example of functionalization.

The merits of MOFs make them applicable as catalyst supports. Numerous palladium catalysts embedded on different MOFs (Pd@MOFs) have been developed through either direct synthesis or post-synthetic immobilization approaches. MIL-101[71] and MIL-88B[72] are used as the MOF supports for Pd(II) and Pd(0) catalysts in this work (here labeled Pd(II)@MIL-101-NH_2, Pd(0)@MIL-101-NH_2, Pd(II)@MIL-88B-NH_2 and Pd(0)@MIL-88B-NH_2). These two MOFs are constructed from terephthalic acid and a trivalent metal salt, but under different reaction conditions. Chromium(III) compounds are the most common metal precursor due to the high stability of the synthesized MOFs, and it is applied in all the MOF materials used in this thesis. The synthesis routes of MIL-101 and MIL-88B are described in Figure 3.2.

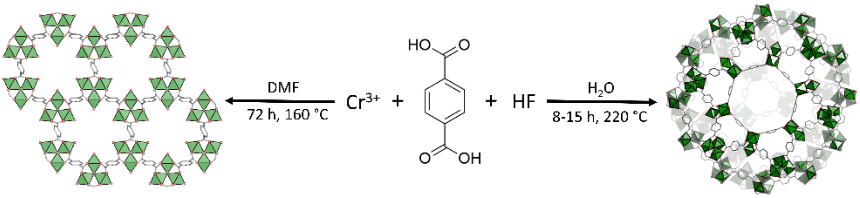

Figure 3.2. Synthesis conditions of MIL-101 and MIL-88B.

In the case of catalysis, MIL-101 allows the transportation of relatively large substrates into the framework, while MIL-88B is more robust, making them attractive candidates as catalyst supports. The strategy of anchoring Pd(II) complexes on the MOFs involves the use of amino-functionalized terephthalic acid as the linker in the frameworks which forms coordination bonds to the Pd complexes. The Pd(II) pre-catalysts can be further reduced by $NaBH_4$ generating Pd nanoparticles as catalysts.[73] These supported Pd nanoparticle catalysts have been developed in our groups and exhibited good catalytic activity and recyclability in several reactions, including Suzuki-Miyaura reaction,[73–75] C–H activation/halogenation reactions,[76] and aerobic oxidation of alcohols.[10]

3.2 XAS characterization of the synthesis of Pd(II/0)@MIL-101-NH_2 and Pd(II/0)@MIL-88B-NH_2

Since loading of Pd is limited and distribution is irregular throughout the frameworks, it becomes challenging to characterize the structure of the Pd catalytic centers by regular in-house instruments. XAS, on the other hand, can probe directly Pd in both complex and aggregate forms on MOFs.[10,11,77–80] All the Pd@MOFs used in this thesis contain ca. 7–8 wt% of Pd which was optimized in the reactivity studies.[73] During the synthesis of Pd(II/0)@MIL-101-NH_2, the Pd species are studied from the Pd(II) precursors to the as-synthesized catalysts, and further compared with the Pd foil. Their XANES spectra are presented in Figure 3.3. Figures 3.3a and b show the XANES spectra of the overall synthesis procedure of the Pd(0)@MOFs. The features of the spectra after the absorption edges are distinct for each sample revealing different coordination environments of the Pd atoms and the edge positions reflect their oxidation states. In the case of Pd@MIL-101-NH_2 (Figure 3.3a), the spectrum of $Pd(CH_3CN)_2Cl_2$ consists of two small peaks (red), while the spectrum of Pd(II)@MIL-101-NH_2 displays one broad peak (blue). Pd species clearly transformed when the Pd precursor was mixed with MIL-101-NH_2. It is also noted that the Pd K-edge positions of $Pd(CH_3CN)_2Cl_2$ and Pd(II)@MIL-101-NH_2 are almost on top of each other and are ca. 4 eV above the edge position of the Pd foil (black) which has an oxidation state of 0. Pd(II)@MIL-101-NH_2 is then reduced by $NaBH_4$ aiming to generate Pd(0)@ MIL-101-NH_2. Transmission electron microscopy confirms the formation of Pd nanoparticles in the previous studies.[73,75] Interestingly, features of the XANES spectrum of the reduced sample (green) still has distinguishable differences compared to the Pd foil, and its edge position is below Pd(II) samples, but still well above the Pd foil. These signs hint that Pd(II) species and Pd nanoparticles co-exist in the reduced sample. The observations from XANES spectra of Pd(II/0)@MIL-101-NH_2 synthesis correlate well with the results from Pd(II/0)@MIL-88B-NH_2 as shown in Figure 3.3b, indicating that Pd in Na_2PdCl_4 goes through a similar transformation over the curse of the synthesis. Moreover, as-synthesized Pd(II)@MIL-101-NH_2 and Pd(II)@MIL-88B-NH_2 are selected and compared in Figure 3.3c. The edges of these two samples indicate that they have exactly the same oxidation state, +II. The features after the edges show small but observable differences, suggesting a similar coordination environment of Pd in these two samples with only slight variations. This is reasonable when considering the difference in precursors as well as MOFs. On the other hand, XANES spectra of Pd(0)@MIL-101-NH_2 and Pd(0)@MIL-88B-NH_2 exhibit almost identical features and edge positions implying the comparable compositions of Pd.

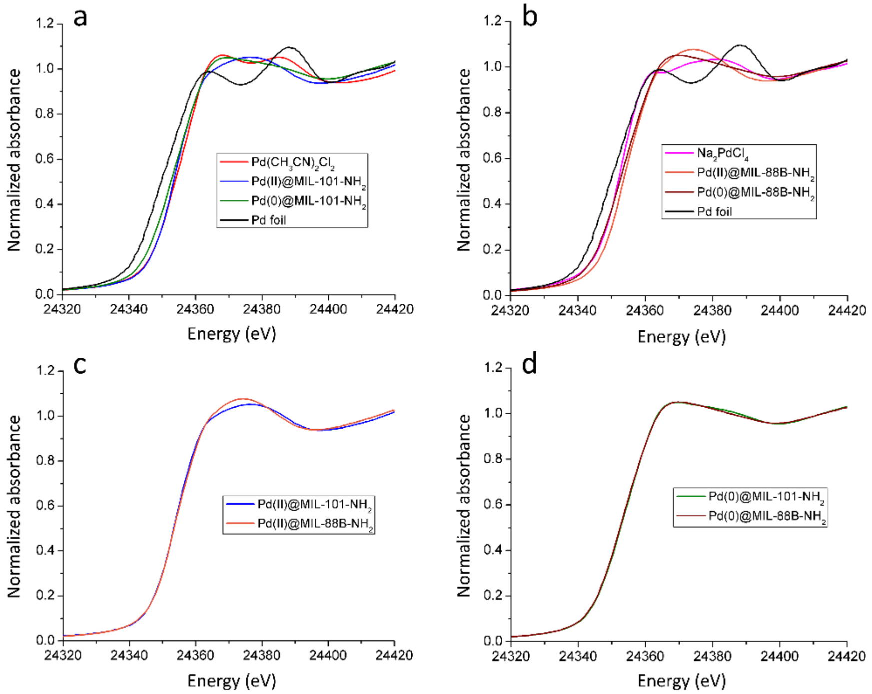

Figure 3.3. Normalized Pd K-edge XANES spectra of Pd precursors, as-synthesized Pd(II/0)@MOFs and Pd foil. (a) Synthesis of Pd@MIL-101-NH_2. (b) Synthesis of Pd@MIL-88B-NH_2. (c) Comparison of as-synthesized Pd(II)@MIL-101-NH_2 and Pd(II)@MIL-88B-NH_2. (d) Comparison of as-synthesized Pd(0)@MOFs and Pd(0)@MIL-88B-NH_2.

The samples discussed in Figure 3.3 are further explored by EXAFS spectra as shown in Figures 3.4 and 3.5 to determine the specific coordination environments of Pd. The refinement results are summarized in Tables 3.1 and 3.2. Figure 3.4 and Table 1 refer to the synthesis of Pd(II/0)@MIL-101-NH_2. The k range is fixed at 2.0–13.0 Å^{-1} for all the EXAFS spectra to ease the comparison. In both Pd(CH_3CN)$_2$$Cl_2$ and Pd(II)@MIL-101-$NH_{2,}$ one Pd atom on average is bound to two N– and two Cl–ligands. However, their EXAFS spectra show significant differences. The bond distance of Pd–N and its mean-square disorder (σ^2) in Pd(II)@MIL-101-NH_2 have larger values than in Pd(CH_3CN)$_2$$Cl_2$ suggesting different types of N–ligands in the pre-catalyst. This indicates a successful synthesis of Pd(II) complexes onto the MOF from its precursor. After Pd(II)@MIL-101-NH_2 was mixed with $NaBH_4$, the Pd–Cl peak disappeared, meanwhile, a prominent peak corresponding to Pd–Pd bond was observed. This proves the formation of metallic Pd species, which is supported by the EXAFS of Pd foil reference in Figure 3.4d. Considering the lower coordination number and shorter bond distance of the Pd–Pd in the catalyst in comparison with Pd foil, the metallic Pd species were estimated in the form of nanoparticles, which was also proved by TEM characterizations in previous works.[73,75,76] Surprisingly, another peak with pronounced magnitude at the position of Pd–N or Pd–O was also observed. Due to the absence of the signal from Pd—Pd in PdO,[81–83] this peak is probably attributed to Pd–N. The observations from EXAFS spectra agree with the XANES spectra, and they lead to a scenario where both Pd nanoparticles and unreduced complexes coexist in Pd(0)@MIL-101-NH$_2$.

Table 3.1. *Refined coordination number (N), distance (d/Å), mean square disorder (σ^2/Å^2), and amplitude reduction factor (S_0^2) in the synthesis of Pd(II/0)@MIL-101-NH$_2$. Underscored parameters were optimized from several trials and were fixed in the individual refinements.*

Samples	*1st shell*	*N*	*d*	*σ^2*	S_0^2
Pd(CH$_3$CN)$_2$Cl$_2$	Pd–N	<u>2.0</u>	1.966(2)	0.0013(2)	0.88(3)
	Pd–Cl	<u>2.0</u>	3.292(2)	0.0026(2)	
Pd(II)@MIL-101-NH$_2$	Pd–N	<u>2.0</u>	2.114(8)	0.012(2)	1.17(4)
	Pd–Cl	<u>2.0</u>	2.298(1)	0.0032(2)	
Pd(0)@MIL-101-NH$_2$	Pd–N/O	<u>2.0</u>	2.030(1)	0.0044(1)	0.90(2)
	Pd–Pd	<u>3.0</u>	2.732(1)	0.0102(1)	
Pd foil	Pd–Pd	<u>12.0</u>	2.741(1)	0.0054(1)	0.83(2)

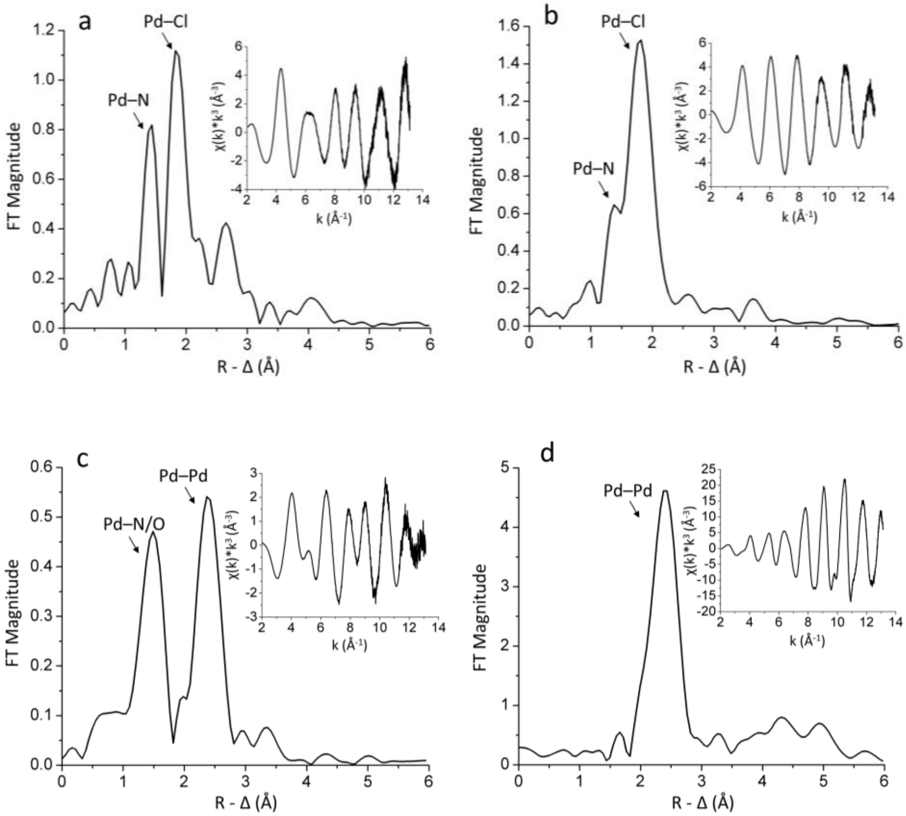

Figure 3.4. Fourier transformed k^3-weighted EXAFS spectra of (a) Pd(CH_3CN)$_2$$Cl_2$, (b) Pd(II)@MIL-101-$NH_2$, (c) Pd(0)@MIL-101-$NH_2$, and (d) Pd foil. The spectra are not phase corrected and the corresponding EXAFS spectra are displayed as an inset with a range fixed at 2.0 – 13.0 Å^{-1}.

The EXAFS spectra and the refinement results of the synthesis of Pd(II/0)@MIL-88B-NH_2 are shown in Figure 3.5 and Table 3.2, respectively. The Fourier transformed EXAFS spectrum of Na_2PdCl_4 only consists of one dominant peak corresponding to Pd–Cl bond with a coordination number of four. After the precursor was mixed with MIL-88B-NH_2, Pd–N bond appeared, and both Pd–N and Pd–Cl have a coordination of two in Pd(II)@MIL-88B-NH_2. This confirms that two of the Cl^- ligands bound to Pd in the precursor were replaced by N– ligands, and Pd(II) complexes were embedded onto the framework. Pd(0)@MIL-88B-NH_2 have a similar feature as Pd(0)@MIL-101-NH_2 which is also the case for their XANES spectra in Figure 3.3d. It implies that both Pd(0)@MOFs consist of comparable Pd species.

Table 3.2. *Refined coordination number (N), distance (d/Å), mean square disorder (σ^2/Å^2), and amplitude reduction factor (S_0^2) in the synthesis of Pd(II/0)@MIL-101-NH$_2$. Underscored parameters were optimized from several trials and were fixed in the individual refinements.*

Samples	*1st shell*	*N*	*d*	*σ^2*	*S_0^2*
Na_2PdCl_4	Pd–Cl	4.0	2.305(1)	0.0029(1)	0.73(1)
Pd(II)@MIL-88B-NH$_2$	Pd–N	2.0	2.051(2)	0.0031(2)	0.90(2)
	Pd–Cl	2.0	2.287(1)	0.0035(1)	
Pd(0)@MIL-88B-NH$_2$	Pd–N/O	2.5	2.033(1)	0.0058(2)	0.85(2)
	Pd–Pd	2.5	2.734(1)	0.0102(1)	

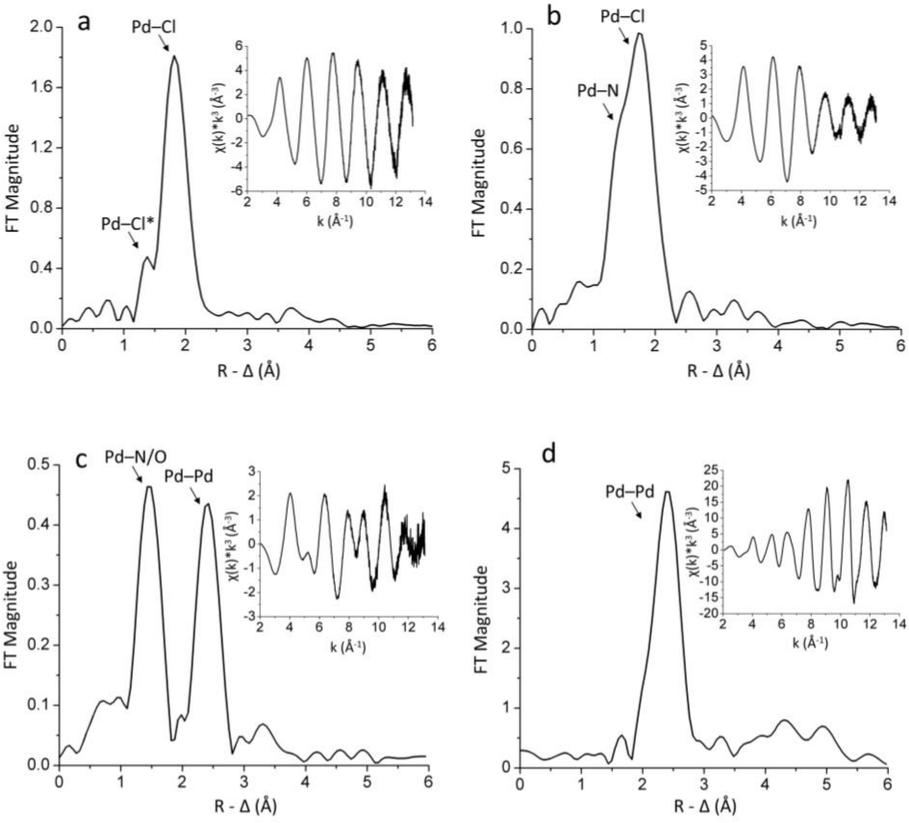

Figure 3.5. Fourier transformed k^3-weighted EXAFS spectra of (a) Na_2PdCl_4, (b) Pd(II)@MIL-88B-NH$_2$, (c) Pd(0)@MIL-88B-NH$_2$, and (d) Pd foil. The spectra are not phase corrected and the corresponding EXAFS spectra are displayed as an inset with a range fixed at 2.0 – 13.0 Å^{-1}. *The peak at ca. 1.4 Å in (a) is a satellite peak of Pd–Cl single scattering.

It is noted that although in both Pd(II)@MIL-101-NH_2 and Pd(II)@MIL-88B-NH_2 the coordination number of N– ligands to Pd is two, the magnitude of the peak corresponding to Pd–N bond in Pd(II)@MIL-101-NH_2 is lower than in Pd(II)@MIL-88B-NH_2. This is caused by the bigger mean square disorder value of the first catalyst sample, implying different types of N– ligands. Based on the EXAFS analysis of the Pd(II)@MOF catalysts, the Pd precursors and the chemical environment during the synthesis of the catalyst, we proposed that each Pd atom in Pd(II)@MIL-101-NH_2 is bound to one –NH_2 on the linker, and one nitrile ligand from the original precursor, while both of the N-ligands bound to Pd in Pd(II)@MIL-88B-NH_2 are –NH_2. Figure 3.6 depicts the coordination structures of the two Pd(II)@MOF catalysts.

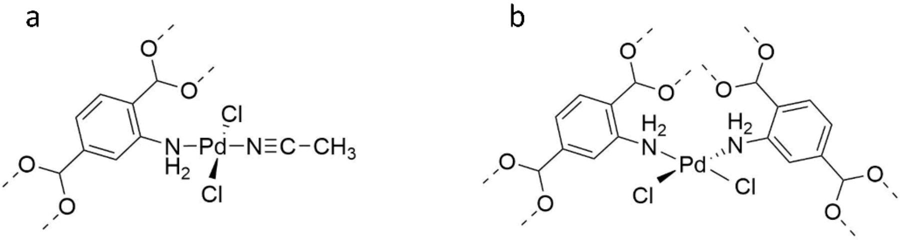

Figure 3.6. Coordination structures of (a) Pd(II)@MIL-101-NH_2 and (b) Pd(II)@MIL-88B-NH_2. (Figure adapted from Paper I.)

3.3 Nature of the active Pd species and catalyst deactivation during Pd(II)@MOFs catalyzed Heck coupling reaction

3.3.1 The Heck coupling reaction

The Heck coupling reaction (also called Mizoroki-Heck reaction) is an important chemical approach for synthesizing substituted alkenes from unsaturated halides and alkenes catalyzed by palladium.[84] The catalysis is via a Pd(0)/Pd(II) process where the Pd(0) is firstly oxidized to Pd(II) by oxidative addition of C–X (X: halide ions), which is followed by migratory insertion and beta-hydride elimination steps. The catalytic cycle terminates with a reductive elimination where the Pd(0) compound is regenerated.

3.3.2 Catalytic reaction condition designed for *in situ* measurements

Due to the beam interferences from the reactor and the reaction mixture, the catalyst loading was increased to ca. 18 mol%, together with the doubled concentration of reagents in comparison to the standard conditions. As described in scheme 3.1, *p*-iodobenzonitrile (0.04 mmol, 92 mg), *tert*-butyl acrylate (1.5 equiv), sodium acetate (2 equiv, base, 66 mg), and Pd@MOF catalyst (0.075 mmol, ca. 100 mg for 8 wt% Pd loading) were mixed in H_2O (1 mL) and Dimethoxyethane (DME) (3 mL) in the vial. The reaction temperature was raised from 60 to 90 °C. Although the reaction conditions were modified from the standard conditions, control experiments affirmed that no differences, other than an increased reaction rate, were observed. Hence, the knowledge derived from the *in situ* experiment can be used to explain a general catalytic reaction.

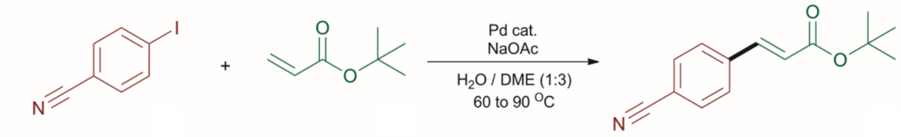

Scheme 3.1. The Heck coupling reaction for *in situ* measurements. (Scheme adapted from Paper I.)

To maximize the understanding of the catalytic active species under the specific reaction conditions, the *in situ* experiment was designed in a sequence of operations illustrated in Figure 3.7. *Step one (t = -20–0 min)*: *p*-iodobenzonitrile, NaOAc, Pd(II)@MIL-101-NH_2, together with 1 mL H_2O and 2 mL DME were added into the vial. The mixture was homogenized by stirring and maintained at room temperature. Meanwhile, *tert*-butyl acrylate was deliberately dissolved in 1 mL DME and loaded in the syringe attached to the reactor (see Figure 2.15, Section 2.4.4). Data collection was then started to check the behavior of the pre-catalyst when the olefin had not been added and there was no catalytic reaction initiated. *Step two (t = 0 min)*: the 1 mL *tert*-butyl acrylate solution was injected into the vial, and 1 mL headspace air in the vial was extracted accordingly to prevent overpressure. *Step three (t = 0–10 min)*: The temperature of the reaction was raised to 60 °C instantly in less than 1 min, and kept for 10 min. *Step four (t = 10–30 min)*: The temperature was increased stepwise by 10 °C every 10 min until it reached 90 °C. *Step five (t = 30–90 min)*: The temperature was held at 90 °C for 1 hour to assure the reaction was completed. *Step six (t = 90–115 min)*: The reaction mixture was cooled down to room temperature in a rate of 3 °C/min while the data acquisition was continued.

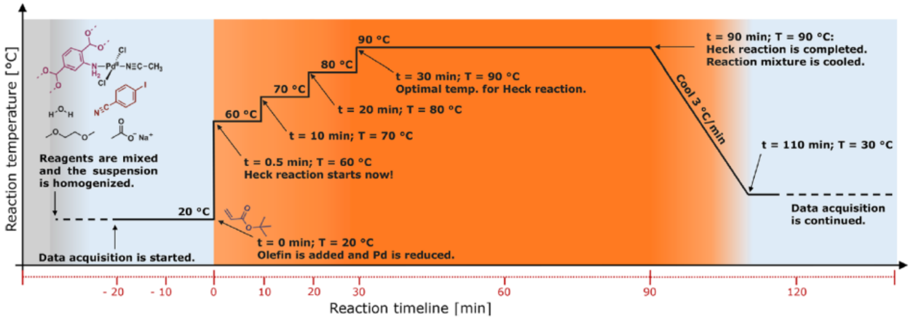

Figure 3.7. Timeline of the *in situ* XAS and PXRD measurements. (Reprinted with permission from *J. Am. Chem. Soc*. 2018, 140 (26), 8206–8217. Copyright (2018) American Chemical Society.)

3.3.3 Kinetics of the Pd(II)@MOF precatalysts catalyzed Heck reaction

The kinetic profile of the Heck reaction catalyzed by Pd(II)@MIL-101-NH$_2$ was first studied and presented in Figure 3.8 (blue curve). The experiment was performed under the conditions designed for *in situ* XAS and PXRD described above. To our surprise, an efficient conversion was already initiated since the beginning of the reaction using either of the catalysts when the temperature was 60 °C. Moreover, an unexpected plateau followed after the fast conversion in the case of Pd(II)@MIL-101-NH$_2$ at ca. 70–80 °C, reflecting a sudden diminished activity of the catalyst. The conversion restored when the temperature was increased to 90 °C and continued in a regular kinetic profile where the activity decreased as the reagents were consumed. This unusual stepwise feature of the kinetic profile provided the first hint of different mechanisms being dominant during each step of the reaction. To support our speculation here, the kinetic profile of Pd(II)@MIL-88B-NH$_2$ catalyzed reaction was also examined (Figure 3.8, green curve). During the initial stage of the reaction at 60 °C, the catalyst exhibited a similar profile compared to Pd(II)@MIL-101-NH$_2$ with a subtly higher reaction rate. This observation suggests a similar catalytic mechanism. Nevertheless, when the reaction proceeded to ca. 70–80 °C, the reaction rate slowed down to some extent instead of being almost completely suppressed with the activity as in the previous case, implying a slightly different mechanism. The reaction rate also recovered at 90 °C as for Pd(II)@MIL-101-NH$_2$ which indicates a comparable behavior of the catalysts at this stage. The unexpected observations from both of the Pd(II)@MOF catalysts intrigued the interests of identifying the Pd species over the course of the reaction to gain more insights into the reaction mechanisms. It should also be noted that both of the

Pd(II)@MOF pre-catalysts suffered from deactivations after the first run of the Heck reaction.

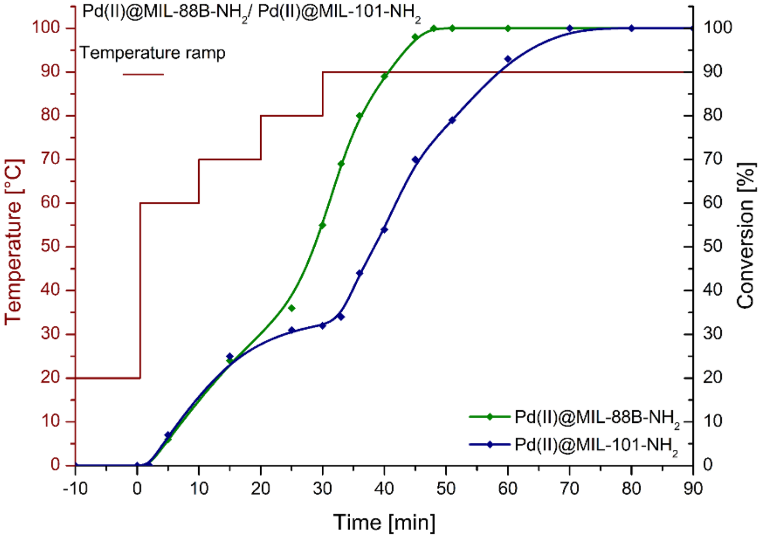

Figure 3.8. Kinetic profiles for Pd(II)@MIL-101-NH$_2$ and Pd(II)@MIL-88B-NH$_2$ catalyzed Heck reaction under the *in situ* measurement conditions. The curves were generated based on the marked data points. (Reprinted with permission from *J. Am. Chem. Soc*. 2018, 140 (26), 8206–8217. Copyright (2018) American Chemical Society.)

3.3.4 Simultaneous *in situ* XAS and PXRD measurements

The customized reactor described in section 2.4.4 was used for both *in situ* XAS and PXRD measurements. The XAS measurements were conducted at Pd K-edge (24.35 keV)[12] in transmission mode. A Pd foil was measured simultaneously and its first inflection point was used to individually calibrate the energy for all the spectra. *In situ* XAS and PXRD data were collected alternatively by switching measurement modes. Each XAS spectrum took ca. 3.4 min and five successive XAS scans were collected in a set. Acquisition of five PXRD patterns was followed which took ca. 1 min. Together with the time spent on swapping the measurement modes, about 2.4 min in total was the time gap between two XAS measurement sets. All the XAS and PXRD data in this project were collected at beamline BM01B at ESRF, Grenoble, France.

3.3.5 *In situ* XAS measurement and data analysis

To probe the active Pd species during the Heck reaction, *in situ* XAS was used as the main investigation method. Due to the more distinct behavior of Pd(II)@MIL-101-NH_2, as presented in the previous section, it was chosen as the main catalyst to be explored in this work. Firstly, XAS spectra of the as-synthesized catalyst and the first *in situ* scan (t = -20 min in Figure 3.7) were selected and compared in Figure 3.9 to understand the behavior of the as-synthesized catalyst in the initial stage of the *in situ* measurement. It can be seen that both the XANES and Fourier transformed (FT) EXAFS spectra show visible changes as soon as the as-synthesized catalyst was added to the reaction mixture at room temperature, before the catalytic reaction was started. The peak in the XANES spectrum after the edge becomes broader relative to the as-synthesized catalyst. However, the edge positions of both spectra are almost identical, indicating that Pd at the beginning of the measurement remained in the form of Pd(II) complex, but in a different coordination environment.

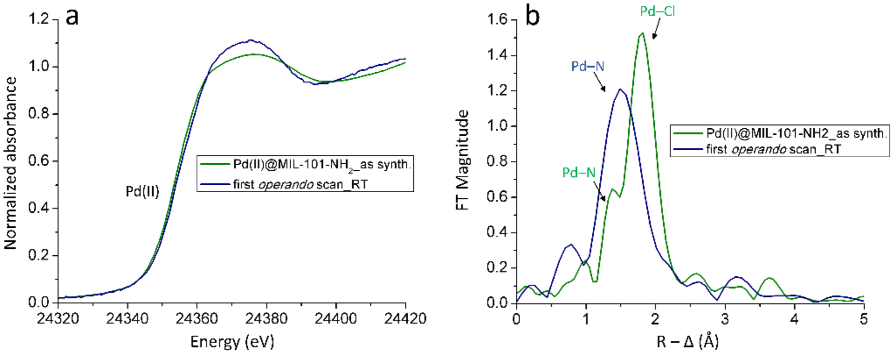

Figure 3.9. Pd K-edge XANES spectra (a) and Fourier transformed k^3-weighted EXAFS spectra (b) of as-synthesized Pd(II)@MIL-101-NH_2 and its first *in situ* scan at room temperature.

The FT EXAFS spectra (Figure 3.9, right) revealed that Cl– ligands in the as-synthesized catalyst were replaced by two N– ligands presumably from *p*-iodobenzonitrile after it was added to the reaction mixture. This is because N–ligands form more stable Pd complexes by several orders of magnitude than Cl– and O– ligands in aqueous media.[85–89] During the first *in situ* scan, each Pd atom on average was bound to four N– ligands with a bond distance of 2.083(6) Å which is shorter than the Pd–N bond in the as-synthesized catalyst (Table 3.1), implying the substitution of another type of N– ligand.

An overview of the XANES spectra during the entire *in situ* measurement is presented in Figure 3.10. The first couple of XANES spectra have the same edge features, appearing as one smooth peak, indicating an unchanged coordination environment of Pd. At a later stage, the smooth peak starts to gradually split into two smaller peaks showing a change in the Pd speciation.

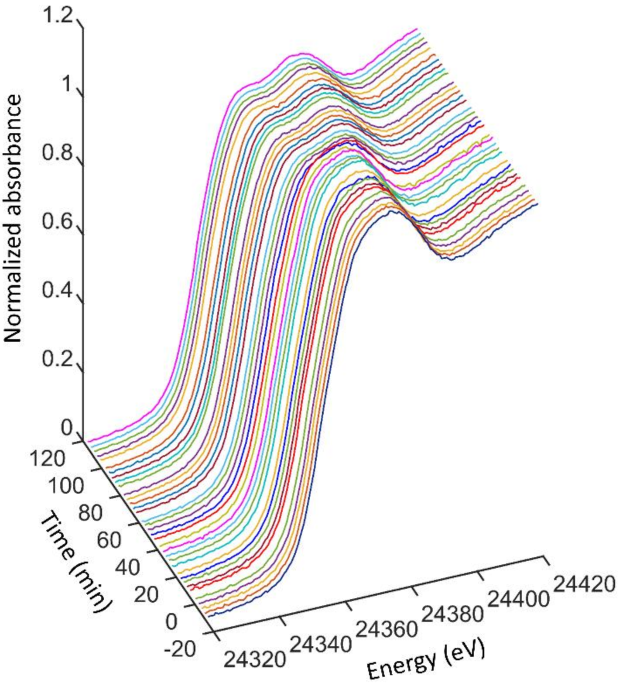

Figure 3.10. Normalized Pd K-edge XANES spectra of Pd(II)@MIL-101-NH_2 catalyzed Heck reaction as a function of measurement time. (Reprinted with permission from *J. Am. Chem. Soc*. 2018, 140 (26), 8206–8217. Copyright (2018) American Chemical Society.)

To follow the changes more accurately and clearly, representative XANES spectra were selected and displayed in Figure 3.11, including the as-synthesized catalyst and Pd foil as references. After the transformation of the catalyst when added to the reaction mixture at RT, the XANES spectra overlap and are comprised of almost identical features until 27 min when the reaction was at 80 °C (Figure 3.11a). This observation reveals that the Pd atoms retained as mononuclear Pd complexes with a similar coordination environment during this measurement period. The edge positions of the *in situ* spectra are almost identical and locate close to the edge of the as-synthesized Pd(II) catalyst. These observations indicate that the Pd complexes have an oxidation state of +II. As the reaction was heated to 90 °C from 31 min, changes of the XANES spectra occurred (Figure 3.11b). The peak after the edge of the *in situ* XANES spectra in Figure 3.11a gradually broadened and split into two smaller peaks, which resembles the features of the Pd foil. This is an indication that the mononuclear Pd(II) complexes were reduced and transformed into metallic Pd aggregates. Meanwhile, the edge position was slowly and constantly shifting towards lower energy, which is direct evidence of decreased mean oxidation state of Pd during this period of measurement. It is noted that the Pd K-edge of the recycled catalyst positions roughly right in the middle of the Pd foil and mononuclear Pd(II) complexes. This denotes that the Pd in the recycled catalyst has an average oxidation state of ca. +I.

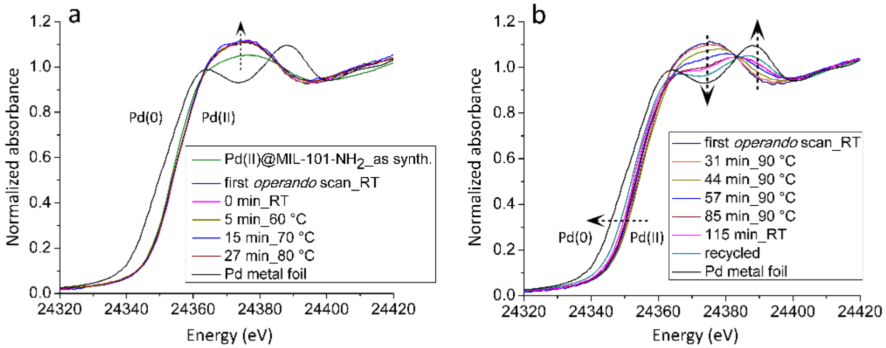

Figure 3.11. Selected *in situ* Pd K-edge XANES spectra of a) Pd(II)@MIL-101-NH_2 catalyst showing the as-synthesized catalyst, the heating steps and Pd metal reference, b) first *in situ* scan, 90 °C, cooling back to RT, recycled catalyst and Pd metal. (Reprinted with permission from *J. Am. Chem. Soc*. 2018, 140 (26), 8206–8217. Copyright (2018) American Chemical Society.)

The corresponding *in situ* EXAFS spectra were further analyzed and refined to probe the specific coordination environments of Pd in Pd(II)@MIL-101-NH_2 during the reaction. Figure 3.12 shows the *in situ* FT-EXAFS spectra as a function of measurement time. EXAFS spectra collected at 24 min and 34–38 min were excluded due to the untreatable data quality. The FT-EXAFS spectrum of the as-synthesized catalyst is shown frontmost as the starting point, and the spectrum of the recycled catalyst is the last one along the time line representing the ending point. It has been discussed in Figure 3.9b that the Cl– ligands bound to Pd in the as-synthesized catalyst were substituted immediately by another two N– ligands when the catalyst was added to the reaction mixture at RT. This was derived from the disappearance of the peak in FT-EXAFS spectrum corresponding to Pd–Cl single scattering. The FT-EXAFS spectrum of the re-formed mononuclear Pd(II) complexes consists of one main peak at ca. 1.5 Å (without phase correction) representing the four coordinated N– ligands. This main peak remains unchanged while no significant peaks at positions outside 1.5 Å are observed, suggesting that Pd is only in the form of mononuclear complexes. Considering that the Heck reaction was already initiated since t = 0, Pd–C bonds were expected when the reagents reacted with Pd, and the peak at ca. 1.5 Å can be interpreted as Pd–N/C bonds, which cannot be resolved by EXAFS due to their similar bond lengths. These FT-EXAFS spectra with similar peaks are in good agreement with the same part of the XANES spectra. Together, they indicate that mononuclear Pd(II) complexes with on aveage four coordinated N/C– ligands were the dominating Pd species when the reaction was at RT (t = 0) until 80 °C (t = 27 min).

When the temperature reached 90 °C (t = 31 min), a peak at ca. 2.3 Å (without phase correction) appeared, corresponding to Pd–Pd bonds. This peak then grew in intensity progressively during the measurement showing an increasing amount of metallic Pd. Interestingly, while the Pd–Pd peak became more prominent, another peak at ca. 1.9 Å emerged which can be attributed to Pd–Cl distances or a satellite peak from Pd–Pd. The detailed discussion can be found in Section 2.5.3 and it proves the existence of Pd–Cl bonds. In addition, inductively coupled plasma atomic-emission spectroscopy (ICP-OES) was also used to determine the element composition of the recycled catalyst. A significant amount of Cl (1.05 wt%) was detected and the molar ratio of Pd/Cl is ca. 1.2 according to the ICP-OES results. As the peaks for Pd–Pd grew, the peak for Pd–N/C shrinked. At the end of the measurement and in the recycled catalyst, the Pd–Pd peak became dominant with the Pd–Cl peak at the shoulder position. The changes of the EXAFS spectra after the reaction was heated to 90 °C are consistent as well with the XANES spectra in Figure 3.11b. The formation of metallic Pd caused the shift of the edge towards lower energies. The formation of the Pd–Cl bonds indicates the presence of Pd(II) in the system which could be induced by the oxidation of the Pd atoms on the surface of small Pd aggregates. This explains the average oxidation state (+I) of the recycled catalyst, reflected by its edge position, as a result of a mixture of Pd(0) and Pd(II) species.

Following the direct observations of the *in situ* FT-EXAFS spectra, detailed coordination parameters of the Pd catalysts were obtained by fitting their EXAFS spectra. A maximum of three coordination shells of Pd···Pd, one shell of Pd–N/C and Pd–Cl were used to optimize the refinement. The model used to fit Pd···Pd was the crystalline structure of Pd metal in face-centered cubic packing. The experimental EXAFS spectra and their best fit can be found in the supporting information of Paper I. Table 3.3. summarizes the key fitting parameters of the first coordination shell including the bond distances and the number of bonds. One of the complexities of EXAFS data is its average nature. When two Pd species co-exist, the fraction of a certain species should be considered when calculating the real number of a bond. In Table 3.3, the number of Pd–Pd was calculated by dividing the refined number of Pd–Pd by the fraction of Pd nanoclusters. The result was then utilized to deduce the average size of the Pd aggregates fromed *in situ*. Surprisingly, the calculated size was smaller than 1 nm in diameter in a spherical model. Each aggregate on average is made of ca. 13 Pd atoms and they can be caterogrized as Pd nanoclusters. The size of the Pd nanoclusters was found significantly smaller than the nanoparticles in commercial catalysts, such as Pd@C,[90,91] Pd@Al_2O_3[91,92] and Pd@polymers.[37] Furthermore, the mean bond distances of Pd–Pd were refined to 2.65–2.67 Å, which is noticeably shorter than the distances in bulk Pd metal (2.74 Å) and even Pd nanoparticles with a size of ca. 2 nm (≥ 2.71 Å). This is attributed to the relatively small size of the Pd nanoclusters transformed. It is known that the Pd–Pd bond shrinks if it involves surface atoms of a particle compared to the interior atoms, due to the lower CN in the first case.[93] The relationship between the bond distance and coordination number has also been studied by all-electron density function[94] and EXAFS refinements[95], which also supports our conclusions here. The Pd–Cl bond was detected for the first time after 57 min when the conversion reached 95%. It is noted that the bond distances of the re-formed Pd–Cl bonds were determined to 2.35–2.42 Å, which was significantly longer than a typical Pd–Cl bond, such as in the as-synthesized Pd(II)@MIL-101-NH_2. This implied that the Pd bound to Cl could be the surface atoms of the Pd nanoclusters where the Pd atoms had a higher coordination number which resulted in the prolonged bond distance. Furthermore, there were no EXAFS signals corresponding to $PdCl_2$ observed, such as Pd–Cl–Cl or Pd–Cl–Pd–Cl scatterings.

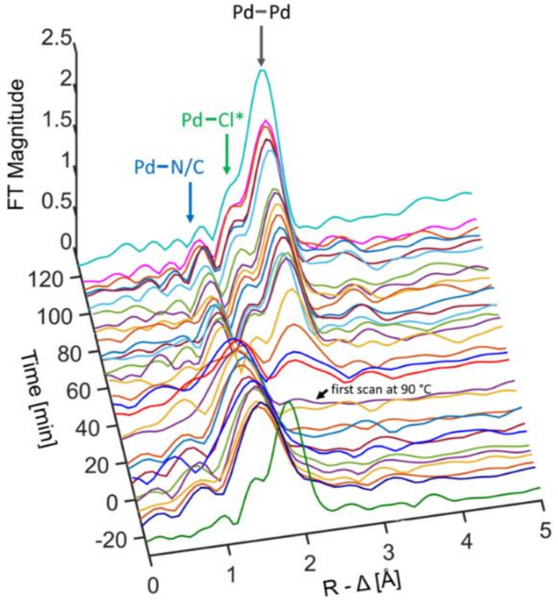

Figure 3.12. Fourier transformed k^3-weighted EXAFS spectra as a function of measurement time probing the local structure of Pd atoms. Pd bonds are marked and correlated to the FT signals. *The peak at ca. 1.9 Å consists of the signal of Pd–Cl single scattering and the satellite peak of Pd–Pd single scattering. The spectra are not phase corrected. (Reprinted with permission from *J. Am. Chem. Soc*. 2018, 140 (26), 8206–8217. Copyright (2018) American Chemical Society.)

Table 3.3. *Refined distances (d/Å), and mean number of distances (N) in selected scans using Pd(II)@MIL-101-NH₂ catalyst. (Table adapted from Paper I)*

Catalyst	**d(Pd-N/C) (Å)**	**N[a]**	**d(Pd-Cl) (Å)**	**N[a]**	**d(Pd···Pd) 1st shell (Å)**	**N[a,b]**
As synth.	2.114(8)	2.0	2.298(1)	2.0	-	-
First scan	2.083(6)	4.0	-	-	-	-
31 min	2.056(4)	3.8	-	-	2.710(7)[c]	0.4(8.0)[c]
44 min	2.037(6)	3.4	-	-	2.674(5)	0.8(4.0)
47 min	1.993(9)	2.9	-	-	2.666(7)	1.8(4.5)
50 min	2.026(8)	2.8	-	-	2.655(4)	2.7(6.0)
57 min	1.980(6)	1.3	2.37(1)	0.4	2.654(4)	2.8(5.6)
63 min	1.956(5)	1.0	2.35(1)	0.7	2.653(4)	3.1(5.6)
73 min	1.979(7)	0.8	2.38(2)	1.0	2.662(3)	3.2(4.9)
85 min	1.959(7)	0.9	2.38(1)	1.0	2.662(3)	3.7(4.9)
115 min	1.978(7)	0.8	2.384(7)	1.0	2.662(2)	4.2(5.3)
Recycled	-	-	2.415(3)	1.0	2.689(1)	6.5
Pd foil	-	-	-	-	2.741(1)	12.0

[a] Values were optimized from several trials and were fixed in each single refinement. [b] The N values in parentheses are the true numbers of Pd–Pd in the 1st shell calculated by taking into account the fractions of Pd nanoclusters. [c] The values of bond distance and N of Pd–Pd in the 1st shell at 31 min contain relatively big errors in addition to the standard deviation due to the limited EXAFS signal of Pd–Pd.

The fractions of the mononuclear Pd(II) complexes and Pd nanoclusters over the course of the transformation were estimated by linear combination fit (LCF) of the XANES spectra, and the results are presented in Figure 3.13. The XANES spectra of the first *in situ* scan and the recycled catalyst were used as references for mononuclear Pd complex and Pd nanoclusters, respectively. The results show that Pd remained in the mononuclear complex form at the beginning of the measurement and started to transform into nanoclusters from 31 min untill 115 min. Generally, the transformation proceeded faster when it was initiated, appearing as a steep slope in Figure 3.13. It then gradually slowed down towards the end of the *in situ* measurement. The full transformation was completed in the recycled catalyst as discussed above. The LCF fit of the XANES spectra can be found in the supporting information of Paper I.

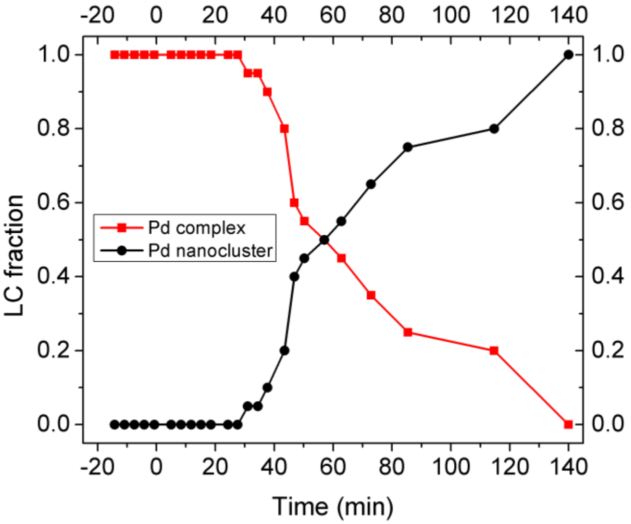

Figure 3.13. Fractions of mononuclear Pd(II) complexes and Pd nanoclusters in the catalyst derived from linear combination fit of XANES spectra over the course of the measurement time. (Reprinted with permission from *J. Am. Chem. Soc*. 2018, 140 (26), 8206–8217. Copyright (2018) American Chemical Society.)

3.3.6 Insights into the catalytic active species in the first stage of the measurement

3.3.6.1. In situ formation of Pd(0) and a competition between catalytic reaction and aggregation

After achieving an understanding of the Pd species over the course of the entire measurement, there are a few mysteries that haven't been illustrated. The first one is the formation of Pd(0) from the pre-catalyst which is the initial status of Pd when it entered the catalytic reaction cycle. It was found that a combination of H_2O and olefin can reduce Pd(II) in the pre-catalyst rapidly while olefin itself becomes oxidized in a Wacker-type process.[96] This happened when olefin was added to the reaction mixture at t = 0 min. To prove this process, additional in house experiments were performed. Pd(II)@MIL-101-NH_2 was used in the same reaction conditions as those of the XAS measurement except a higher Pd loading (30 mol %). Proton nuclear magnetic resonance (^{1}H NMR) captured the signals of aldehyde from α-formylacetate derivative at 9.9 – 9.6 ppm when olefin was oxidized. The necessity of H_2O for reducing Pd(II) was also examined by control experiments. Pd(II)@MIL-101-NH_2 was stirred for 10 min at room temperature with the olefin using only DME, and then a mixture of DME and H_2O as the solvents. The resulting catalysts were characterized by transmission electron microscopy (TEM). No Pd nanoparticles were detected in the first experiment even when the reaction mixture was heated to 60 °C, as shown in Figure 3.14a, while Pd nanoparticles were clearly visible in the second experiment, as shown in Figure 3.14b. A representative color change from light green to dark green-black was also noticed in the second experiment suggesting the reduction. The observations here confirmed how Pd(0) was derived from the Pd(II) pre-catalyst.

Interestingly, only mononuclear Pd(II) complexes were recognized during the *in situ* XAS measurement as we concluded previously. All these observations indicate a scenario that the *in situ* formed atomic Pd(0) triggered the Heck reaction and was re-oxidized directly by the aryl iodide substrate in an oxidative addition step of the catalytic cycle. The key point here is that the atomic Pd(0) was so active that it entered the catalytic cycled before they aggregated. Furthermore, the resting state of Pd intermediate in the catalytic cycle of the Heck reaction has an oxidation state of +II, which explains the absorption edge position in Figure 3.11a.

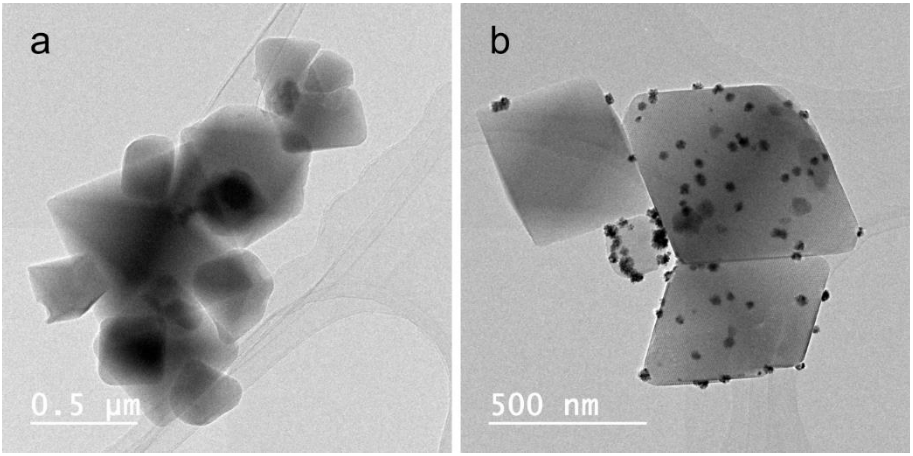

Figure 3.14. TEM images of Pd(II)@MIL-101-NH_2 exposed to olefin and DME with (a) and without H_2O. (Reprinted with permission from *J. Am. Chem. Soc*. 2018, 140 (26), 8206–8217. Copyright (2018) American Chemical Society.)

3.3.6.2. The secrecy of the plateau in the kinetic profile

Another question concerns the plateau region in the kinetic profile of Pd(II)@MIL-101-NH_2 (Figure 3.15, solid blue line). It is now known that this sudden diminishing of the reaction rate happened before mononuclear Pd complexes started to transform into Pd nanoclusters. The plateau feature should be attributed to possible changes in the coordination environment of the mononuclear Pd complexes. To gain a better understanding here, a control experiment was performed where the kinetic profile of Pd(II)@MIL-101-NH_2 catalyzed Heck reaction at 60 °C was investigated (Figure 3.15 dashed blue line). To our surprise, the reaction ceased after one turnover. Based on this information, it was assumed that the Pd complexes in the pre-catalyst lost their coordination to the MOF linkers. XAS data provided a hint to support this assumption, where the Pd–N mean distance in the pre-catalyst was 2.114(8) Å and this distance decreased to 2.056(4) Å at 31 min. The loss of nitrogen donor (Ar–NH_2 in the MOF) led to insufficient electron density on Pd to participate in the second catalytic cycle. It can be imagined that the mobile mononuclear Pd complexes tended to aggregate when the temperature was maintained at 60 °C. Thus, the plateau in the stepwise heating condition was likely due to the decreased amount of mononuclear Pd complexes bound to the MOF linker. In this case, an electron rich ligand, such as aniline, Ar–NH_2, seems to be crucial to retain the activity of Pd at 60 °C. We then designed another experiment where aniline, a homogeneous model for the MOF linker, was added in stoichiometric amounts to the reaction mixture and the reaction temperature was again kept at

60 °C. Interestingly, full conversion was reached with the addition of aniline (Figure 3.15 dotted blue line), and the shape of its kinetic profile suggested a homogeneous reaction. This was examined by TEM and energy dispersive X-ray spectroscopy (EDS) where the catalyst at different stages of the catalytic reaction was characterized. Pd was presented while no Pd nanoparticles were detected before the catalytic reaction was completed. This information confirms that oxidative addition is faster than aggregation when a nitrogen donor ligand (Ar–NH_2) was bound to Pd.

The mobile mononuclear Pd complexes were inactive at 60 °C, their activity at 90 °C was explored by adding a second load of reagents at 70 min when the Pd nanoclusters already had their surface covered by Cl– ligands. A full conversion was achieved in 70 min demonstrating that the mobile mononuclear Pd complexes recovered their activity at a higher temperature. Their activity should also be higher than the Pd nanoclusters considering their size and available coordination sites.

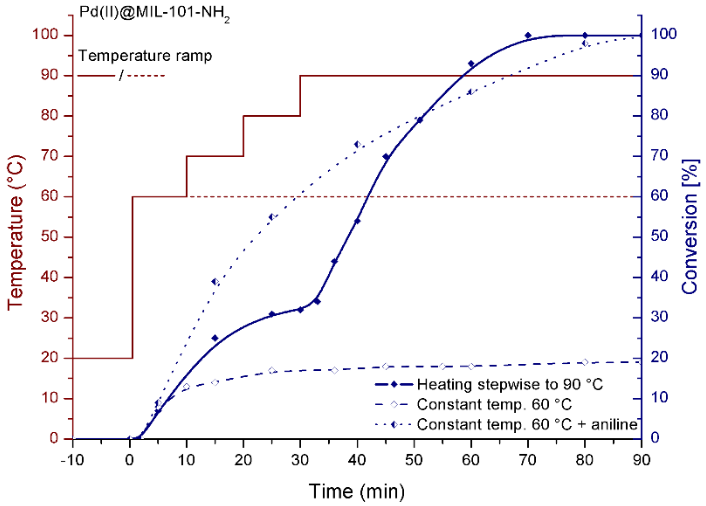

Figure 3.15. Kinetic profiles for Pd(II)@MIL-101-NH_2 catalyzed Heck reaction under various reaction conditions. The curves were generated based on the marked data points. (Reprinted with permission from *J. Am. Chem. Soc*. 2018, 140 (26), 8206–8217. Copyright (2018) American Chemical Society.)

3.3.7 The stability of the framework and the catalyst distribution

In situ PXRD was used to monitor the crystallinity of the frameworks. It revealed that both MIL-101-NH_2 and MIL-88B-NH_2 retained their crystallinity through the entire measurement showing that the MOFs were stable under the conditions used in the catalysis reactions. This excludes the possibility of MOF degradation causing the changes of Pd species.

3.3.8 Schematic evolution of Pd species and their activities

Based on all the discussions above, we were able to unveil the whole evolution of the Pd species and it is schematically visualized in Figure 3.16. In summary, mononuclear Pd(II) complexes were bound to the linkers of the MOF in the as-synthesized catalyst. The two Cl– ligands were then replaced instantly by N–ligands when the as-synthesized catalyst was added to the reaction mixture at room temperature. Pd(II) was *in situ* reduced to atomic Pd(0) upon the addition of olefin when the reaction temperature was raised to 60 °C. These Pd species were active at 60–80 °C and entered the catalytic cycle directly. Pd(0) was then oxidized during the oxidative addition step before it had the chance to aggregate. These mononuclear Pd complexes detached from the linker after one turnover and became mobile in the reaction mixture. The temperature was further increased to 90 °C. At this stage, the mobile mononuclear Pd complexes started to gradually transform into Pd nanoclusters. At 57 min when the conversion was close to 100%, the free Cl– ligands in the reaction mixture began to bind to Pd again on the surface of the Pd nanoclusters. At the end of the *in situ* measurement, Pd nanoclusters with Cl– ligands on the surfaces became the dominating species and a complete transformation was achieved in the recycled catalyst.

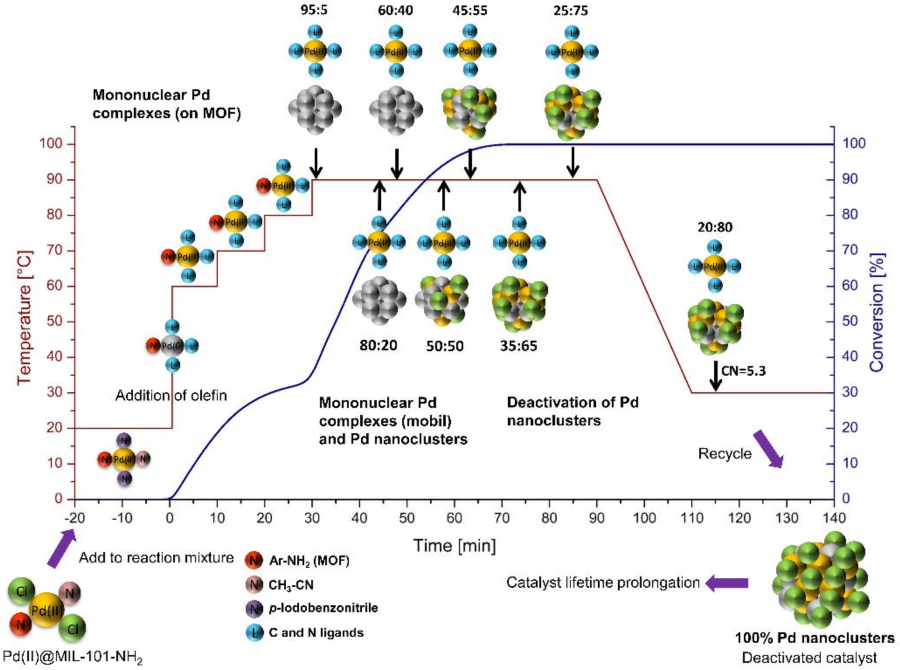

Figure 3.16. Proposed evolution of Pd species during the Heck coupling reaction catalyzed by Pd(II)@MIL-101-NH$_2$. (Reprinted with permission from *J. Am. Chem. Soc*. 2018, 140 (26), 8206–8217. Copyright (2018) American Chemical Society.)

3.3.9 Prolongation of the catalyst lifetime

By understanding the evolution of the Pd species and their activities, it became possible to improve the usage of the current catalyst. In this work, it had been realized that the recycled catalyst lost its activity dramatically. It was proposed that the deactivation results from the coverage of Cl– ligands on Pd nanoclusters. The lifetime of the catalyst could be extended by adding new loads of reagents before the positioned Pd nanoclusters became the dominating species. The catalyst mixture continued to convert new reagents to products effectively for at least 3 cycles. The experiment also suggested that the catalyst was suitable for a continuous flow mode where the deactivation of Pd species could be prevented or postponed.

3.3.10 *In situ* XAS measurement of Pd(II)@MIL-88B-NH$_2$ catalyzed Heck reaction.

The XANES and Fourier transformed EXAFS spectra of Pd(II)@MIL-88B-NH$_2$ catalyzed Heck reaction exibit similar features and changes in comparison to

Pd(II)@MIL-101-NH_2 (Figures 3.10–3.12). This indicates that the Pd species in MIL-88B-NH_2 and MIL-101-NH_2 went through a comparable evolution during the *in situ* measurements, which supports the conclusions drawn in MIL-101-NH_2. One thing that needs to be pointed out is that the kinetic profile of Pd(II)@MIL-88B-NH_2 catalyzed Heck reaction didn't show an obvious plateau as observed in Pd(II)@MIL-101-NH_2 (Figure 3.8). Previously, we have investigated the coordination environment of Pd in Pd(II)@MIL-88B-NH_2. The result showed that each Pd atom was bound to two amino ligands in a chelating fashion (Figure 3.6b).[10] This configuration could bind the Pd complexes better onto the MOF linker and there was a higher probability that the Pd complexes remained partially bound to the linker after the first turnover in comparison to the case of Pd(II)@MIL-101-NH_2. A control experiment where the experiment was maintained at 60 °C, was also performed and the reaction rate slowed down after one turnover but was not completely suppressed, in comparison to the case of Pd(II)@MIL-101-NH_2. The result agreed well with our understanding of the activity of the mononuclear Pd complexes at temperatures lower than 90 °C.

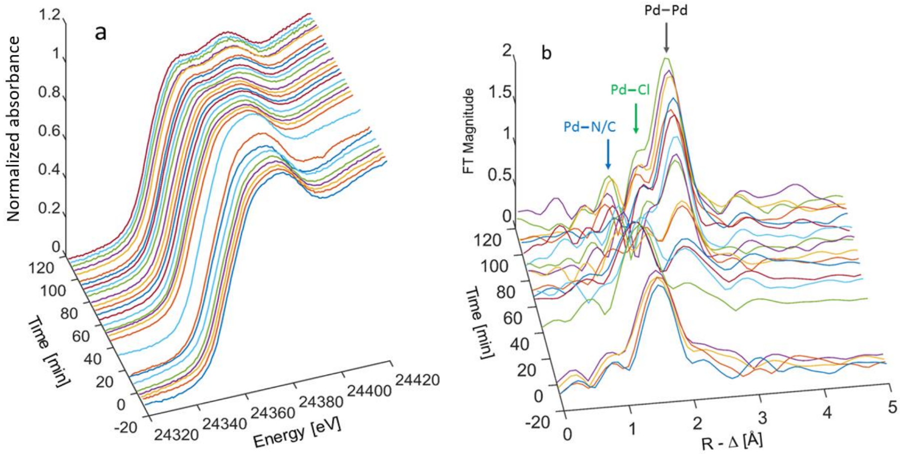

Figure 3.17. (a) Normalized Pd K-edge XANES spectra and (b) Fourier transformed k^3-weighted EXAFS spectra of Pd(II)@MIL-88B-NH_2 catalyzed Heck reaction as a function of measurement time. *The peak at ca. 1.9 Å consists of the signal of Pd–Cl single scattering and the satellite peak of Pd–Pd single scattering. The spectra are not phase corrected. (Reprinted with permission from *J. Am. Chem. Soc*. 2018, 140 (26), 8206–8217. Copyright (2018) American Chemical Society.)

3.4 Conclusion

The evolution of Pd species in the Pd(II)@MOFs during the Heck coupling reaction was elucidated using *in situ* XAS as the main approach. Different active Pd species were identified at different stages of the measurement. The deactivation mechanism of the catalyst was also revealed, and it was caused by the coverage of Cl^- ions on the surface of the transformed Pd nanoclusters. Lifetime prolongation of the catalyst was then achieved by the improved design of reaction process. More importantly, this work demonstrated the opportunities of using *in situ* XAS to study similar catalytic systems using our customized *in situ* reactor.

4 *In Situ* XAS Study of the Pd Species in a Supported Pd(II) Carbene Complex Catalyst and its Homogeneous Analog during an Undirected C–H Acetoxylation Reaction (Paper II)

4.1 Introduction

N–Heterocyclic carbene palladium complexes (Pd–NHC) are a family of organopalladium compounds that have been widely used in homogenous catalysis, such as cross-coupling reactions.[97–99] Great efforts have been put on developing heterogeneous catalysts based on Pd-NHC complexes due to the demand for recyclability and novel chemical reactivity.[100–102] Recently, reduced graphene oxide (here labeled rGO) was successfully used as a catalyst support on which an anthracene-tagged Pd(II)-NHC complex (here labeled **1**) was immobilized through π-interactions.[103] Figure 4.1. schematically describes the immobilization of **1** onto rGO, forming **1**@rGO. The benefit of this non-covalent approach is that the need to modify the homogenous Pd complex and the support is minimized.[103–105] In previous works, **1**@rGO was used as an active and recyclable catalyst in undirected C–H oxygenation of benzene.[103] However, the experimental evidence of the reaction mechanism was still missing, which motivated us to apply *in situ* XAS to gain insights into the Pd species during the reaction.

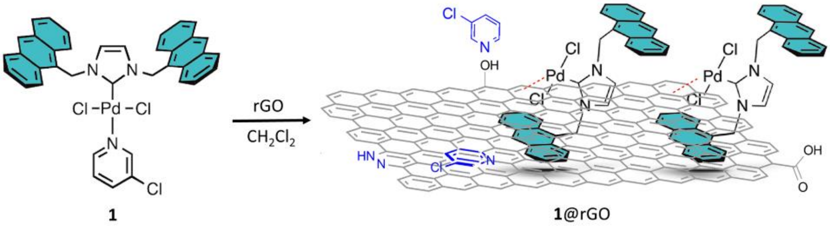

Figure 4.1. Immobilization of **1** on rGO. (Reprinted with permission from *Catal. Sci. Technol.* 2019, 9 (8), 2025–2031. Copyright (2019) The Royal Society of Chemistry.)

4.2 XAS characterizations of the synthesis of **1**@rGO

The structure of **1** had been confirmed by ^{1}H- and ^{13}C-NMR. Pd atoms in **1** had an oxidation state of +II. Each Pd atom was bound to two Cl– ligands, an anthracene-tagged NHC complex, and one pyridine.[103] When **1** was immobilized onto rGO, the characterization of the catalyst became difficult. Pd- and Cl-XPS were previously used to determine the valence state of these elements, which then helped to predict the local structures of Pd in **1**@rGO.

In this project, XAS was chosen as it probed the local structure of the Pd atoms directly. The XANES spectra of the as-synthesized catalysts are shown in Figure 4.2 together with the Pd foil reference. The edges of these two spectra overlap well, indicating an oxidation state of +II for the Pd in 1@rGO. The edge positions of the catalysts are at higher energies than the Pd foil, but the edge shift is not as big as in the cases of Pd(II)@MOFs (Figure 3.3a–b). It is known that the edge position of an element is determined by its electron density. Not only the oxidation state can influence the edge position, but also the type of coordinated ligands. In the current catalysts, anthracene-tagged NHC ligand has a strong electron donating effect to the Pd(II) atoms, which then increases the electron density of Pd and further presses the edge position to lower energy. While in the case of Pd(II)@MOF, such an effect from ligands is not obvious. This is a good example of demonstrating the sensitivity of edge position to the ligand types. The features of the XANES spectra after the edges are also similar between as-synthesized **1** and **1**@rGO suggesting comparable Pd local structures in these two catalysts.

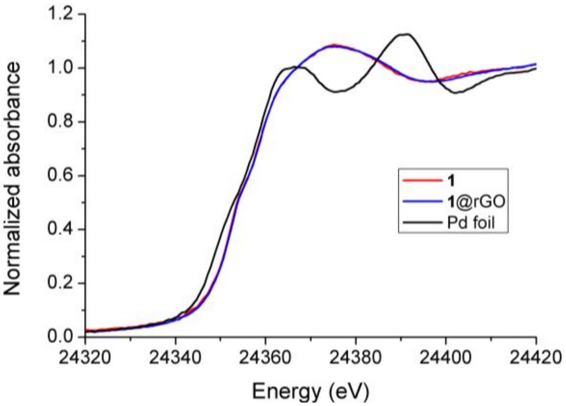

Figure 4.2. Pd K-edge XANES spectra of as-synthesized **1** and **1**@rGO catalysts and Pd foil. (Figure adapted from Paper II)

The specific coordination environments of the catalysts were explored by EXAFS analysis. Figure 4.3 shows the EXAFS spectra and their FTs, as well as the best fits. The EXAFS spectra of the catalysts also appeared to be similar. Both FTs contained a pronounced peak at the position matching Pd–Cl bond. The bond lengths were refined to 2.29–2.30 Å and the number of bonds to each Pd atom was determined to be 2. Another peak at ca. 1.25 Å, without phase correction, was observed in both FT spectra. It was known that in **1** each Pd was bound to one NHC– ligand and one pyridine ligand (Figure 4.1). The low intensity of this peak reflected a large bond distance distribution. This indicates that there are two types of C– or N– ligands as well in **1**@rGO. It is also noted that the peak position is at a shorter distance than in the typical case. This was attributed to the average of the single scattering signals of Pd–N/C and the satellite peak of Pd–Cl. In **1**@rGO, one Pd–C/N bond was determined at 1.95 Å which agrees well with the distance from Pd to NHC ligand.[101,103] Another Pd–C/N bond distance was determined to 2.18 Å with a relatively large error, 0.08 Å. Cl–XPS, in an earlier study, showed that the pyridine ligand dissociated from Pd when **1** was embedded on rGO. One possibility was that the Pd atoms were π-bonded to a C=C bond of the rGO support as shown in Figure 4.1. Importantly, it can be concluded that the heterogeneous Pd(II)–NHC complex was successfully prepared.

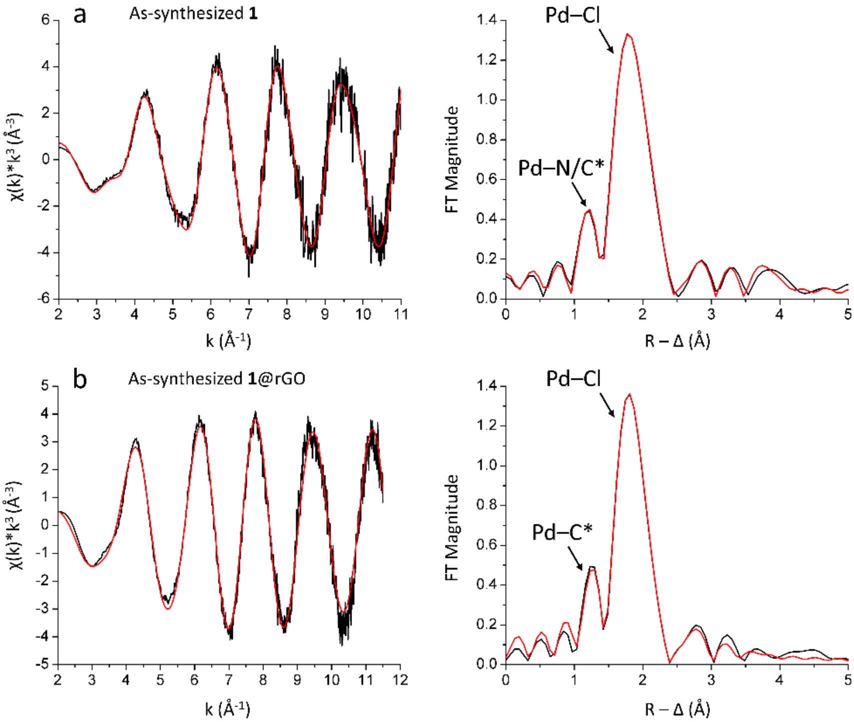

Figure 4.3. Fit of Pd K-edge EXAFS spectra and the corresponding Fourier transformed spectra of (a) as-synthesized **1** and (b) **1**@rGO, black curve – experimental, red curve – model. *The peak at ca. 1.25 Å consists of the signal of Pd–C/N single scatterings and the satellite peak of Pd–Cl single scattering. The spectra are not phase corrected. (Reprinted with permission from *Catal. Sci. Technol.* 2019, 9 (8), 2025–2031. Copyright (2019) The Royal Society of Chemistry.)

4.3 *In situ* XAS measurements of Pd(II)-NHC catalyzed undirected acetoxylation reaction

4.3.1 Catalytic reaction and *in situ* XAS measurement condition

After the characterization of the catalysts, an *in situ* XAS study was performed to follow the change in the Pd speciation during an undirected C–H acetoxylation reaction. Scheme 4.1 illustrates the reaction, and the reactor described in Figure 2.15 was used in the experiment. Benzene (1.75 g, 22.44 mmol, 21.77 equiv.) was the substrate, and (diacetoxyiodo)benzene (0.33 g, 1.03 mmol, 1 equiv.) was used as oxidant. Both **1**@rGO (0.10 g, 2.5 wt% Pd loading, 2.3 mol% with respect to the oxidant) and its analog **1** (0.07 g, 9.2 mol% with respect to the oxidant) were used respectively and compared. Together with glacial acetic acid

(1.50 mL) and acetic anhydride (0.17 mL), all the compounds were added into the vessel of the reactor in the preparation lab and moved to the experiment hutch. The *in situ* XAS measurement was then started while the reaction mixture was stirred and heated instantly to 92 °C.

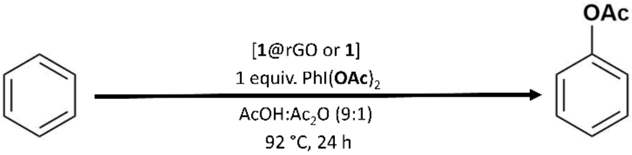

Scheme 4.1. Undirected C–H acetoxylation reaction of benzene over **1**@rGO catalyst using $PhI(OAc)_2$ as an oxidant. (Reprinted with permission from *Catal. Sci. Technol.* 2019, 9 (8), 2025–2031. Copyright (2019) The Royal Society of Chemistry.)

The data collection was performed in transmission mode at the Pd K-edge. An energy range from 24.00 to 25.00 keV was typically applied. The time resolution was set at ca. 6 min with the consideration of data quality. A Pd foil was also measured simultaneously and its first inflection point was used to individually calibrate the energy of all spectra. All XAS data were collected at beamline P64 at Petra III Extension, DESY, Hamburg, Germany.

4.3.2 *In situ* XANES spectra and analysis

The **1**@rGO catalyzed reaction was measured first. One of the challenges in this measurement was the low concentration of Pd (ca. 7 mM) leading to a relatively low S/N ratio. The changes in the recorded data were generally slow which made it possible to average groups of seemingly identical XAS spectra to improve the statistics. This strategy was discussed in Section 2.5.2. Representative XANES spectra were selected and divided into two stages based on the trend in the changes. Figure 4.4a shows the XANES spectra of the as-synthesized **1**@rGO and *in situ* spectra from the beginning of the reaction until ca. 80 min of the measurement. The interesting observation here was that the edge of the catalyst shifted towards higher energies, accompanied by an increase of the white line intensity. It had been reported that the increase in oxidation state of Pd in molecular complexes could lead to the rise of the white line.[106,107] An edge shift towards a higher energy is a strong indication of an increase in the oxidation state, yet it could also be caused by replacement of the ligands. However, the only strong electron-pair donor to Pd in **1**@rGO was the NHC ligand, which formed a fairly strong bond to Pd with a calculated bond energy of 45–50 kcal·mol^{-1}.[108] In addition, **1**@rGO showed good recyclability and the NHC ligand was regarded as the key factor which maintained the activity of the catalyst. This chemical information suggested that NHC is retained during the reaction. Moreover, the introduction of the oxidant also aimed to oxidize Pd(II). Therefore, the edge shift in Figure 4.4a could be concluded as a result of partial oxidation of Pd(II). Although the edge shift was not significant, ca. 1 eV, it was clearly visible. Due to the average nature of XAS, a shift of 1 eV corresponded to ca. 25% of the expected edge shift from Pd(II) to Pd(IV). This scenario was reasonable as the lifetime of Pd(IV) intermediate in a catalytic cycle was expected to be relatively short. This shows that Pd(II) is the dominating oxidation state in the reaction mixture for this specific period of time. Pd(II) could also be oxidized to Pd(III) which tended to form dimers.[109,110] However, no Pd---Pd distance from possible dimers were observed in the Fourier transforms.

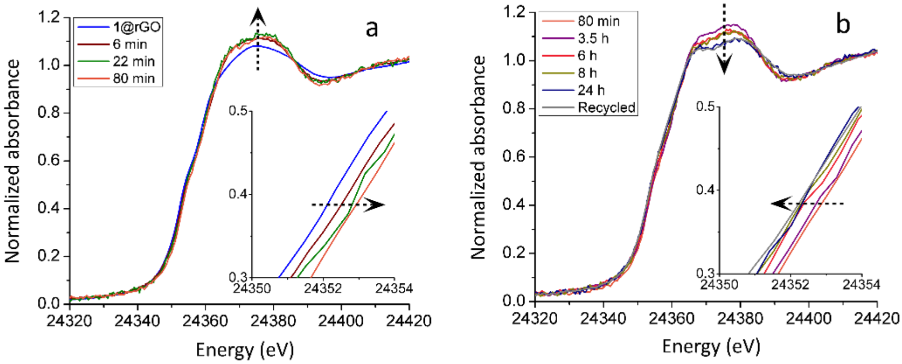

Figure 4.4. *In situ* Pd-K edge XANES spectra of **1**@rGO catalyzed C–H acetoxylation of benzene. (a) The first stage of the measurement when the edge shifted towards higher energy. (b) The second stage of the measurement when the edge shifted towards lower energy. (Reprinted with permission from *Catal. Sci. Technol.* 2019, 9 (8), 2025–2031. Copyright (2019) The Royal Society of Chemistry.)

In the second stage, the absorption edge started to shift backwards to lower energy from 80 min until the end of the measurement, 24 hours, with a generally decreasing trend of the white line intensity. The XANES spectrum of the recycled catalyst had almost identical features in comparison to the spectrum of the catalyst after 24 h. This means that the changes in XANES spectra ceased after 24 h. Through the discussion in the first stage, it could be deduced that the changes in the second stage were connected to a decreasing average oxidation state. The pronounced round peak right after the edge gradually decreased in intensity and split into two small peaks. As discussed in the previous project, this splitting indicates the formation of metallic Pd.

Considering the relatively delicate changes of the *in situ* XANES spectra when studying **1**@rGO catalyst, its analog **1** was also studied under similar reaction conditions to support the analysis and conclusion. The advantage of running *in situ* XAS measurement on **1** was that it was a homogeneous system, which means a better control of the Pd concentration and homogeneity of Pd in the reaction mixture. The *in situ* data had a significantly increased S/N ratio as it was possible to raise the concentration of Pd complex to ca. 35 mM. Although the reaction rate of **1** catalyzed reaction was expected to be faster than **1**@rGO catalyzed reaction due to the higher Pd concentration, the reaction mechanism should not be affected and the results should be comparable.

The changes of the XANES spectra displayed in Figure 4.4 basically had the same trend as in Figure 4.3. From the as-synthesized **1** to ca. 78 min (Figure 4.4a), the white line intensity raised constantly and the major change in the spectra occurred between the as-synthesized catalyst and the first *in situ* scan. Meanwhile, an increase in the edge position was observed indicating an increase in the average oxidation state of Pd. Figure 4.4b shows the XANES spectra from 78 min to 33 h of the *in situ* measurement. Here the edge position gradually shifted to lower energies. The white line intensity dropped and the peak after the edge disappeared with a subtle feature of splitting. These observations imply a decrease in the average oxidation state of Pd and formation of metallic Pd species.

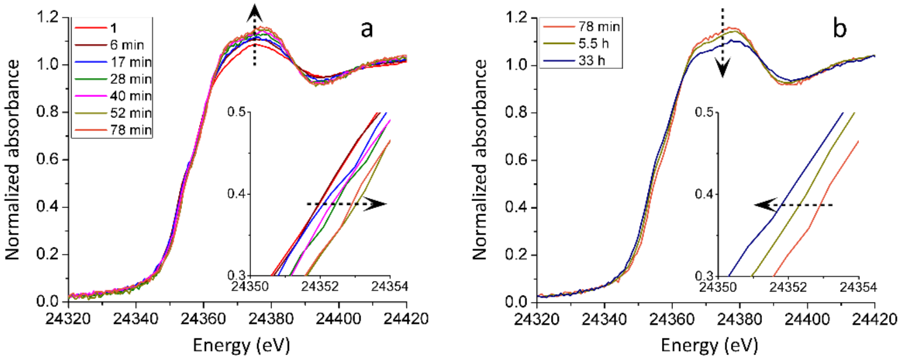

Figure 4.4. *In situ* Pd-K edge XANES spectra of **1** catalyzed C–H acetoxylation of benzene. (a) The first stage of the measurement when the edge shifted towards higher energy. (b) The second stage of the measurement when the edge shifted towards lower energy. (Reprinted with permission from *Catal. Sci. Technol.* 2019, 9 (8), 2025–2031. Copyright (2019) The Royal Society of Chemistry.)

It was also noted that the edges of the last XANES spectra of both **1**@rGO and **1** catalyzed reactions returned to positions close to that of the as-synthesized catalysts. The XANES features after the edge, however, exhibited significant differences. This reveals that the Pd at the end of the measurement had an average oxidation state of ca. +II, the same as the as-synthesized catalysts, but with a different composition. The XANES spectra are given in Figure 4.5.

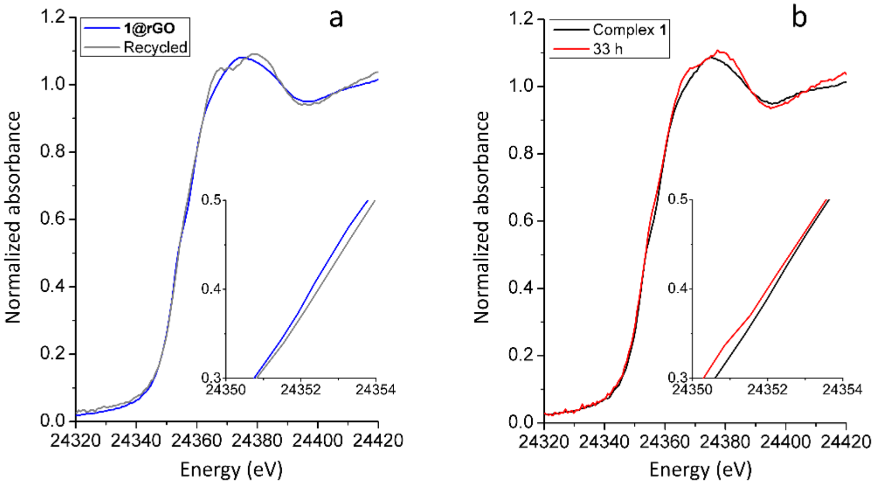

Figure 4.5. Pd K-edge XANES spectra of (a) as-synthesized **1**@rGO and the recycled **1**@rGO, and (b) as-synthesized **1** and **1** at 33 h of the *in situ* measurement. (Reprinted with permission from *Catal. Sci. Technol.* 2019, 9 (8), 2025–2031. Copyright (2019) The Royal Society of Chemistry.)

4.3.3 *In situ* EXAFS spectra and analysis

The specific coordination environments of the Pd in **1**@rGO and **1** during the reaction were explored by *in situ* EXAFS spectra, and their corresponding FTs are shown in Figure 4.6. To ease the comparison of the FTs at different times, the range of all the EXAFS spectra was unified to 2–9 Å^{-1}. The fit of the selected EXAFS spectra can be found in Section S4 of the supporting information of Paper II. Table 4.1 summarizes the refinement results of the first coordination shell of Pd. It should be noted that with the current EXAFS range, the peaks corresponding to Pd–N and Pd–Cl in FTs merge into one broad peak. In Figure 4.6a it can be seen that the main peak has an obvious shift towards a shorter distance from the as-synthesized **1**@rGO to 6 min, indicating an instant local structure change at the beginning of the reaction. Refinement of the catalyst at 6 min showed that each Pd on average was bound to three L ligands (L ligands: C, N and/or O ligands) with a mean bond length of 2.01 Å, and one Cl– ligand with a mean bond length 2.32 Å. From 6 min onwards, the changes of EXAFS spectra progressively slowed down until 80 min. Another shift occurred after 3.5 h where the main peak shifted further towards to shorter mean distance.

Refinement of the EXAFS data revealed that the remaining Cl– ligand bound to Pd was replaced by another L ligand resulting into a four coordinated PdL_4 complex. Meanwhile, a subtle but distinct signal on the right side of the main peak emerged which could be fitted by introducing a Pd–Pd bond with a mean number of 0.8. This signal gradually grew in intensity at 8 h and further at 24 h, with a mean number of Pd–Pd distances of 3.5. The catalyst after 24 h and the recycled catalyst contain the same XANES profile and were regarded to be comprised of similar Pd species. Their FTs, however, do not appear to be identical and this is due to the different S/N ratios of EXAFS causing artificial noise signals. The presence of Pd–Pd bonds was the evidence of the formation of metallic Pd, and its mean bond distance was refined at ≤2.70 Å, which proves the formation of Pd nanoclusters in the second stage of the experiment.

As the homogeneous analog of **1**@rGO, *in situ* EXAFS spectra of **1** catalyzed reaction were also analyzed. Figure 4.6b displays the FTs and the *k* range applied was also deliberately fixed to 2–9 $Å^{-1}$ for comparison purposes. Generally, the FTs exhibited the same trend of changes in comparison to the **1**@rGO system. The main peak shifted towards shorter distance stepwise because of the dissociation of Cl– ligands. A peak in the FTs corresponding to the Pd–Pd single scattering also emerged and grew in the later stage of the experiment, indicating a continuous formation of metallic Pd species. The rate of changes between **1**@rGO and **1** were not exactly the same, for example, a mean number of 1.5 Pd–Cl distances gave the best fit at 6 min in the case of **1**. This can be explained by the higher concentration of Pd in the **1** catalyzed reaction. This slight mismatch can also relate to the relatively higher catalytic efficiency of **1**@rGO under the same reaction conditions reported earlier.[103] The slower substitution of Pd–Cl in **1** might imply a slower activation of the catalyst. To gain a better understanding of the activation phenomenon, an XAS spectrum of **1** was collected at room temperature and was found to be identical to the spectrum of as-synthesized **1**. This result demonstrates that the heating was necessary to trigger the activation of catalyst and initiate the reaction.

Importantly, the consistency in the observed XAS spectra in both the heterogeneous **1**@rGO and its homogenous analog **1** consolidate the reliability of the conclusions of the Pd species evolution over the course of the undirected C–H acetoxylation reaction.

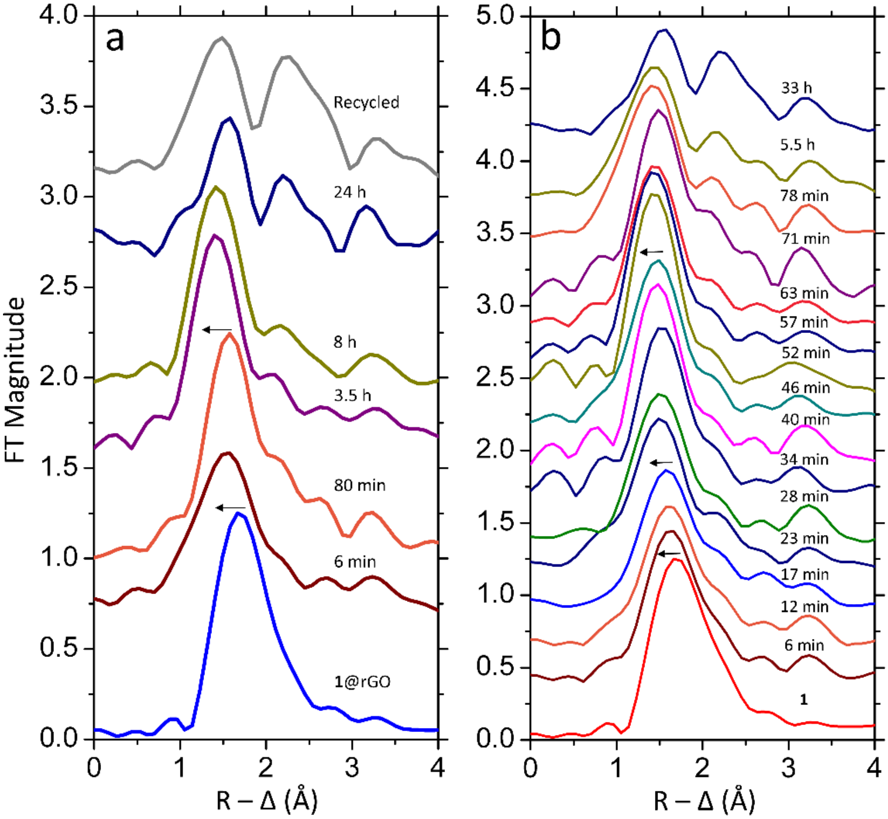

Figure 4.6. *In situ* Fourier transformed k^3-weighted EXAFS spectra as a function of measurement time of (a) **1**@rGO and (b) **1** catalyzed reactions. The spectra are not phase corrected and the EXAFS range applied were fixed at 2–9 Å^{-1} to facilitate comparison. (Reprinted with permission from *Catal. Sci. Technol.* 2019, 9 (8), 2025–2031. Copyright (2019) The Royal Society of Chemistry.)

Table 4.1. *Refined distances (d/Å), mean number of distances (N) and Debye-Waller factor (σ^2/Å^2) in selected scans using **1**@rGO and **1** as catalysts. Single scattering at outer shells and multiple scatterings are not included in the table. Underscored parameters were optimized from several trials and were fixed in the individual refinements. (Table adapted from Paper II.)*

Catalyst	**d (Pd-L)**[a]	**N**[b]	**σ^2**	**d (Pd-Cl)**	**N**	**σ^2**	**d (Pd-Pd)**	**N**	**σ^2**
As synth. 1@rGO	1.953(6) 2.18(8)	1.0 1.0	0.0017(7) 0.007(8)	2.293(9)	2.0	0.0045(9)	–	–	–
6 min (22, 80min)	2.013(6)	3.0	0.009(1)	2.320(6)	1.0	0.007(2)	–	–	–
3.5 h	2.020(4)	4.0	0.006(1)	–	–	–	2.68(2)	0.8	0.007(2)
8 h (6 h)	2.015(7)	3.5	0.005(2)	–	–	–	2.70(4)	1.0	0.005(4)
Recycled (24 h)	1.966(4)	2.0	0.004(2)	–	–	–	2.652(4)	3.5	0.010(4)
As synth. 1	1.95(1) 2.17(8)	1.0 1.0	0.003(2) 0.005(9)	2.301(6)	2.0	0.0015(9)	–	–	–
6 min	2.00(1)	2.5	0.009(1)	2.293(8)	1.5	0.0023(7)	–	–	–
40 min	2.017(7)	3.0	0.003(1)	2.29(3)	1.0	0.003(1)	–	–	–
78 min	2.034(3)	4.0	0.0036(2)	–	–	–	2.65(2)	0.5	0.005(1)
5.5 h	2.032(2)	3.5	0.0043(4)	–	–	–	2.709(7)	1.0	0.010(1)
33 h	2.025(9)	3.0	0.007(2)	–	–	–	2.69(1)	3.0	0.012(2)

4.3.4 Additional discussion of metallic Pd aggregates

TEM, as a more visual approach, also proved the presence of Pd nanoparticles in the recycled **1**@rGO. Meanwhile, the Pd signal was detected over the entire observable sample area and it confirms the existence of Pd species other than Pd nanoparticles, such as small nanoclusters and mononuclear complexes. The TEM and EDS images can be found at the supporting information of Paper II.

It has been realized in the catalysis study that the oxidant PdI(OAc)$_2$ were thermally degraded over time under the current reaction condition.[101] This could be the trigger of the formation of metallic Pd aggregates.

4.3.5 Recyclability

Recyclability study showed that **1**@rGO mostly retained its activity for at least four runs in the undirected acetoxylation of benzene. This could be explained by the Pd complexes retained after the reaction. Interestingly, the GC result showed that the yield of acetoxybenzene slowly decreased from 50% (first cycle) to 46%

(fourth cycle) under lab conditions. By eliminating the possibility of Pd leaching, it is proposed that the formation of metallic Pd species could cause the decrease in efficiency of the recycled catalyst. Meanwhile, it is expected that the amount of metallic Pd species formed in the *in situ* measurement is larger than under lab conditions due to the relative lower amount of oxidant used in the *in situ* measurement.

4.4 Conclusion

By using *in situ* XAS as the major tool, the changes in the mean oxidation state and local structures of Pd atoms in **1**@rGO and its homogeneous analog **1** were revealed over the course of undirected C–H acetoxylation of benzene. Both catalysts basically followed the same transformation route. Cl^- ligands were replaced by L ligands stepwise in the first stage of the reaction while a small fraction of Pd(II) in the as-synthesized catalysts were oxidized to Pd(IV). At a later stage, metallic Pd species gradually formed as the oxidant was consumed and decomposed. The mean oxidation state of Pd decreased simultaneously and ended at a mean value of +II. A mixture of several Pd species including Pd(II) complexes as the major component and small amounts of Pd aggregates and Pd(IV) complexes were proposed. Moreover, these observations provided experimental evidence for a Pd(II)-Pd(IV)-Pd(II) catalytic mechanism which was reported in computation studies.[111]

5 *In Situ* XAS Investigation of the Deactivation and Reactivation Mechanisms of a Heterogeneous Palladium(II) Catalyst during the Cycloisomerization of Acetylenic Acids (Paper III)

5.1 Introduction

The beauty of catalysts is their ability to facilitate reactions with desired products fast and in high yields. The catalytic species of many catalysts transform in the reaction environments. The catalysts can suffer from deactivation if the transformed species are not active, which leads to unwanted efficiency loss of the catalysts. Therefore, the understanding of the deactivation mechanism of the catalysts is important, as it opens up measures to avoid the deactivation or reactivate the catalysts through modifications of the reaction conditions. Pd(II) complex immobilized on amino-functionalized siliceous mesocellular foam (Pd(II)-AmP-MCF) has been used as a Pd(II) heterogeneous catalyst for cycloisomerization of acetylenic acids.[112] Despite the fact that Pd(II)-AmP-MCF showed high efficiency for this transformation, the catalyst was found to lose activity when pent-4-ynoic acid was transformed over repeated reactions. It was also realized that the leaching was negligible in this process. These observations indicated that the Pd(II) complexes likely transformed into another form to some extent, and this new form was expected to be inactive as catalyst. Intriguingly, the activity of the catalyst was possible to restore effectively by treating it with an oxidant, benzoquinone (BQ). The preliminary explanation in the previous work was that the deactivation was caused by the formation of Pd(0) species which was inactive and can be reactivated by the process of oxidation.[112]

After realizing this phenomenon, it became interesting to gain more insights into the deactivation as well as the reactivation mechanisms. In this work, XAS was used to elucidate the Pd species during the cycloisomerizations of two different acetylenic acids, 5-hexynoic acid (here labeled substrate **1**) and 5-phenylpent-4-ynoic acid (here labeled substrate **2**) to probe the active and inactive catalytic species. With these understandings, a control experiment was designed with the purpose to prevent the deactivation to occur, and this process was monitored by *in situ* XAS as well. Importantly, the knowledge acquired from this work is valuable for prolonging the usage of the catalyst, and provide guidelines in customizing the reaction process to circumvent the deactivation of the catalyst.

5.2 *In situ* XAS measurements of Pd(II)-AmP-MCF catalyzed cycloismoerization of acetylenic acids

5.2.1 Catalytic reaction and *in situ* XAS measurement conditions

The Pd species in the unused Pd(II)-AmP-MCF has been studied by EXAFS. Each Pd in the catalyst was bound to two nitrogen donor ligands from the amino groups on the catalyst support, and two chloride ligands from the Pd precursor Li_2PdCl_4.[113] Detailed analysis of the EXAFS spectrum can be found in Section 6.2, Chapter 6. The reactor described in Figure 2.15 was used to perform the reactions. The reaction mixtures for *in situ* XAS measurements consisted of Pd(II)-AmP-MCF (120 mg, 7–8 wt% Pd loading, 7.7 mol%), substrate **1** (2.85 mmol) or substrate **2** (1.44 mmol), toluene (2 mL), trimethylamine (TEA, 0.7 mmol). The reaction mixtures were stirred during the measurement and the reaction temperature was kept at 50 °C. Scheme 5.1 describes the reaction conditions.

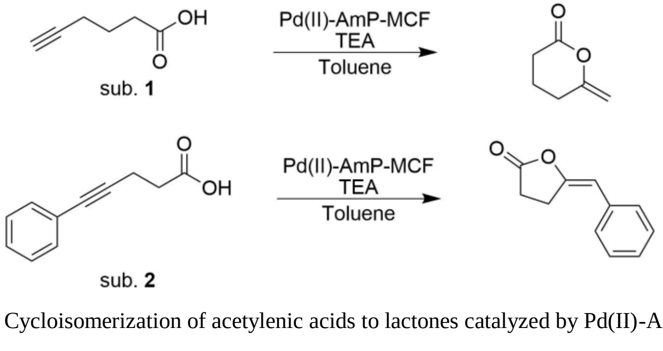

Scheme 5.1. Cycloisomerization of acetylenic acids to lactones catalyzed by Pd(II)-AmP-MCF.

The catalyst during the reactions was followed by *in situ* XAS measurements, and the recycled catalysts were measured using standard sample holders for powders. The XAS data were collected in transmission mode at Pd K-edge with a typical energy range from 24.00 to 25.00 keV. A Pd foil was measured simultaneously and its first inflection point was used to calibrate the energy of the spectra. The time resolution of XAS scans was ca. 6 min with a consideration of the reaction rate and the data quality. All XAS data were collected at beamline P64 at the Petra III Extension, DESY, Hamburg, Germany.

5.2.2 XAS spectra and analysis

Before the *in situ* XAS measurements, the recycled catalysts after catalyzing substrate **1** (here labeled recycled **1**) and **2** (here labeled recycled **2**) were measured and compared with the unused catalyst to quickly recognize if any changes occurred to Pd. The comparison of their XANES spectra are shown in Figure 5.1 including a spectrum of Pd foil. Between the unused catalyst and the recycled **1**, a minor change was observed in the region after the absorption edge, and the edge position shifted towards a lower energy. These observations suggest that the Pd species in the unused catalyst changed slightly during the reaction and the change might be caused by reduction of Pd(II) of a minor fraction of the catalyst. Interestingly, the XANES spectrum of the recycled **2** exhibited obvious changes and the features after the edge are similar to those observed in the spectrum of the Pd foil. Its edge position was also close to the Pd foil. The XANES spectrum of recycled **2** strongly indicates that metallic Pd aggregates were formed and being the dominating Pd species.

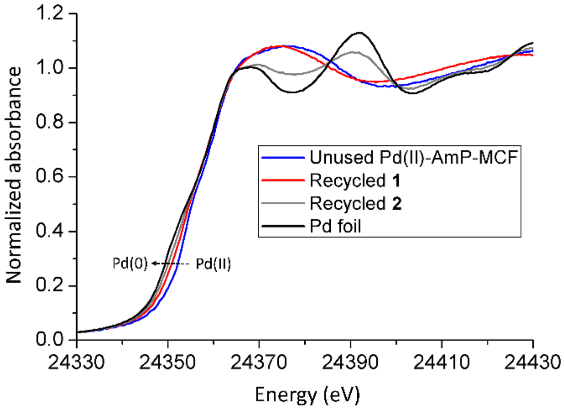

Figure 5.1. Pd K-edge XANES spectra of unused Pd(II)-AmP-MCF, recycled catalyst **1** and **2**, and Pd foil reference.

The EXAFS spectra of the unused and recycled catalysts were also analyzed to probe the local structure of Pd. The Fourier transformed EXAFS data are displayed in Figure 5.2, and the refinement parameters of the first coordination shell are summarized in Table 5.1. The number of major peaks in the Fourier transformed EXAFS spectra and their positions are different. In the unused Pd(II)-AmP-MCF (Figure 5.2a), two main peaks are present in the first coordination shell which correspond to Pd–N and Pd–Pd bonds, respectively.[113] Only one dominating peak appeared in Figure 5.2b and it is at the position matching Pd–N or Pd–O bonds. The bond length was refined at 2.03 Å and the average number bound to each Pd atom was about 2. The values of the bond length and its Debye-Waller coefficient are close to those in the unused catalyst. This hints that the N– ligands bound to Pd in the unused catalyst likely remained in the recycled **1**. Meanwhile, the average number of Pd–Cl bonds decreased to ca. 0.8 meaning that a substantial amount of the Cl– ligands detached from Pd. A small signal corresponding to Pd–Pd was detected as well indicating the formation of metallic Pd species which agrees with the edge shift observed in Figure 5.1. In recycled **2**, the Pd–Pd signal is dominating (Figure 5.2c) meaning that recycled **2** consists of mostly metallic Pd aggregates. A minor peak at the position of Pd–O/N was also observed which could be due to the oxidized surface of the Pd aggregates or the remained N– ligands bound to Pd.

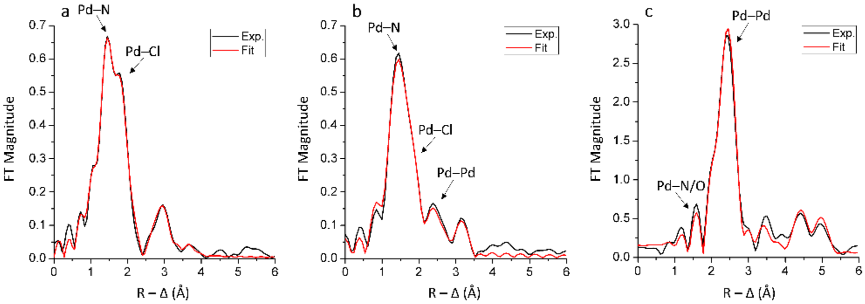

Figure 5.2. Fourier transformed k^3-weighted EXAFS spectra of (a) unused Pd(II)-AmP-MCF and the recycled (b) **1** and (c) **2**. The spectra are not phase corrected. The k ranges used to perform Fourier transform are 2–13, 2–10 and 2–12 Å^{-1}, respectively.

From the measurement above, it can be concluded that the Pd species in the unused Pd(II)-AmP-MCF altered during the cycloisomerization of the acetylenic acids and the recycled catalysts had different compositions. In order to further understand the process of the changes, *in situ* XAS measurements were performed individually using these two substrates. *In situ* XANES spectra are shown in Figure 5.3, and it can be seen that the change of Pd occurred instantly when catalyzing substrate **1** and almost ceased after 6 min. This means that the

Pd in the unused catalyst evolved to a similar state as in the recycled catalyst at the beginning of the reaction and retained a comparable structure afterwards. Therefore, the analysis of Pd species in recycled **1** can be used to understand the Pd speciation during the measurement. On the other hand, the Pd species went through a gradual transformation when catalyzing substrate **2** based on the observation in Figure 5.3b. Over the course of the measurement, the peak after the edge in the unused catalyst became broader and split into two smaller peaks, meanwhile the edge position shifted towards lower energies continuously, and the feature resembling metallic Pd became more pronounced. It is worth mentioning that a spectrum at 31 min was also collected and shown in the supporting information of Paper III. This spectrum is not displayed here because of the noisy data, yet its features after the edge can still be identified showing similarities to that of recycled **2**. This indicates that the change was almost complete at 31 min of the *in situ* measurement.

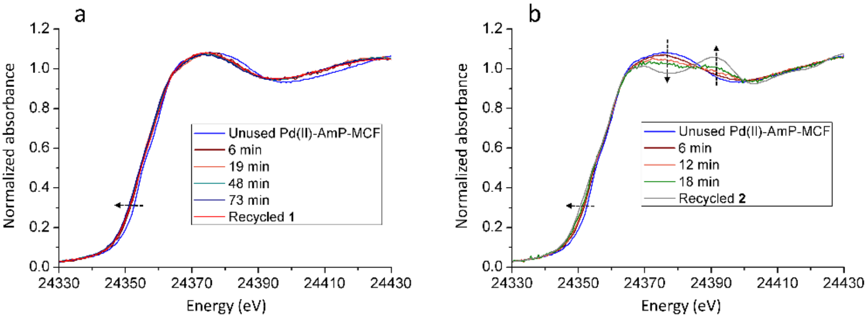

Figure 5.3. Representative *in situ* Pd K-edge XANES spectra of Pd(II)-AmP-MCF catalyzed cycloisomerization of substrate (a) **1** and (b) **2** as a function of the measurement time.

Following these results, a component in the reaction mixture acting as the reducing agent was expected. Due to the deactivation being much more significant in the case of recycled **2**, the following control experiments were focused on substrate **2**. The effect of the solvent was first investigated. An XANES spectrum of Pd(II)-AmP-MCF in toluene at 50 °C was collected and shown in Figure 5.4a. The spectrum contained identical features in comparison to the unused dry catalyst meaning that the catalyst was stable in toluene. Substrate **2** was then added and the XANES spectra are shown in Figure 5.4b. Only very minor changes of the spectra were captured indicating a fairly stable status of Pd. TEA was then added to the reaction mixture. During the experiment TEA was intended to be stored in the syringe attached to the reaction vessel. However, it was found that the vapor of TEA leaked into the vessel through the tubes even before the injection. Figure 5.4c shows the signals of metallic Pd when the TEA vapor was in contact with the catalyst, and this experiment confirmed that TEA was acting as the reducing agent.

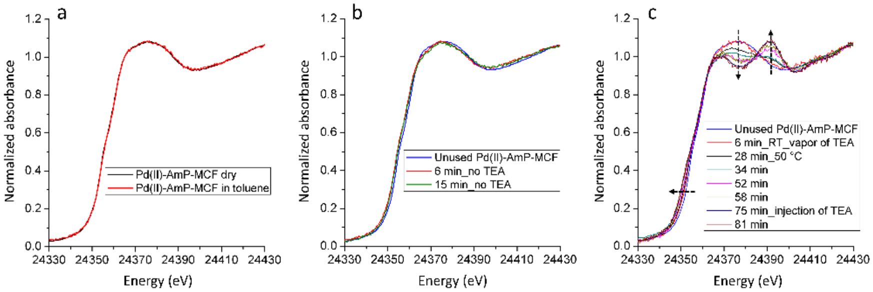

Figure 5.4. Pd K-edge XANES spectra of Pd(II)-AmP-MCF (a) in dry form and in toluene, (b) after the addition of substrate **2**, and (c) after the addition of TEA.

Following the experiment discussed in Figure 5.4, BQ was added to the reaction mixture at the end. Figure 5.5a exhibits the XANES spectra of the catalyst before and after the addition of BQ. It was found that the peaks after the absorption edge were damped upon the addition of BQ, meaning that the features resembling metallic Pd became less pronounced. The corresponding Fourier transformed EXAFS data are shown in Figure 5.5b-c. The spectrum in Figure 5.5b was fitted by including mainly Pd–Pd bonds and a small fraction of Pd–O bonds. The peak at ca. 1.9 Å (not phase corrected) in the experimental data can be fitted by the satellite peak of the Pd–Pd single scattering. Nevertheless, the peak at ca. 1.9 Å became more significant in Figure 5.5c and it cannot be fitted properly by solely the Pd–Pd single scattering. A signal corresponding to Pd–Cl was therefore necessary to achieve a good fit. The refinement details are summarized in Table 5.1. Although the difference between these two spectra is relatively small, it is crucial as it confirmed that a fraction of Pd transformed into the form of Pd(II) complex with Cl– ligands bound to the Pd centres. Although the amount of Pd(II) complexes seems limited, they were the active species formed by the introduction of BQ and were sufficient to catalyze additional reactions.

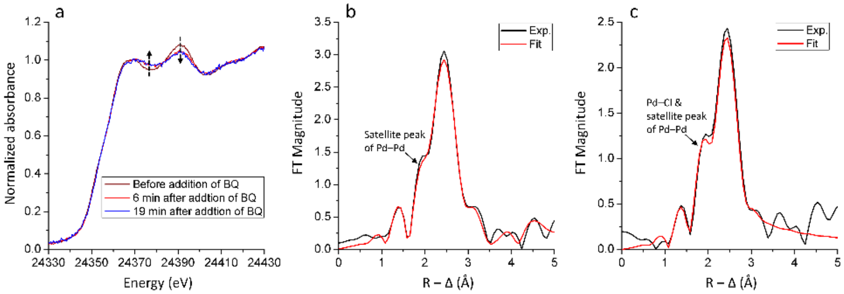

Figure 5.5. Representative *in situ* Pd K-edge (a) XANES and Fourier transformed k^3-weighted EXAFS spectra of Pd(II)-AmP-MCF (b) before and (c) after addition of BQ to the Pd aggregates. The spectra in Figure b-c are not phase corrected and converted from the same k range, 2–10.5 Å^{-1}.

By unveiling the deactivation and reactivation mechanisms, it was possible to design a strategy with the aim to prevent the deactivation process. In the following experiment, BQ was added before the addition of TEA to compete with the reduction. *In situ* XAS was used to monitor the status of Pd during this process and the results are shown in Figure 5.6. As discussed in Figure 5.4b, the addition of substrate **2** led to a slight change of the XANES spectrum, which was also detected in Figure 5.6a. Moreover, Figure 5.6a also includes XANES spectra of the catalyst after adding BQ, and this operation further caused a slight change in the region after the edge. TEA was then added to the mixture. Interestingly, the XANES spectra at this stage exhibited no changes meaning that the presence of BQ effectively prevented the extensive reduction of Pd.

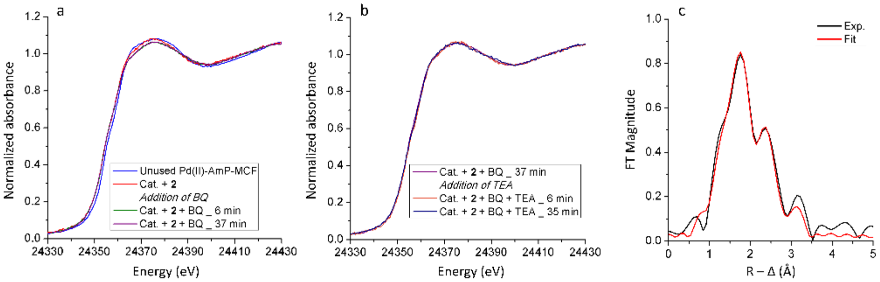

Figure 5.6. Representative *in situ* Pd K-edge XANES spectra of Pd(II)-AmP-MCF mixing with (a) the substrate and BQ, and (b) after the addition of TEA. (c) Fourier transformed k^3-weighted EXAFS spectra of Pd(II)-AmP-MCF after the addition of BQ. The spectrum in Figure 5.6c is not phase corrected and is Fourier transformed on the k range of 2–10 Å^{-1}.

Table 5.1. *Number of distances, N, mean distances, d/Å, and Debye-Waller coefficients, σ^2/Å^2, in the EXAFS refinements. The standard deviations in parentheses were obtained from k^3-weighted least square refinement of the EXAFS function $\chi(k)$ and do not include systematic errors of the measurement. Underscored parameters were optimized from several trials and were fixed in the individual refinements. (Table adapted from Paper III.)*

Samples	*Signal*	*N*	*d*	*σ^2*	S_0^2
Pd(II)-AmP-MCF	Pd–N	2.0	2.023(2)	0.0035(3)	0.93(2)
	Pd–Cl	2.0	2.294(2)	0.0058(2)	
Recycled catalyst 1	Pd–N/O	2.0	2.034(4)	0.0032(7)	0.93(5)
	Pd–Cl	0.8	2.337(5)	0.0035(9)	
	Pd–Pd	0.5	2.72(1)	0.011(2)	
Recycled catalyst 2	Pd–O	0.5	2.07(3)	0.004(3)	0.92(4)
	Pd–Pd	8.0	2.741(2)	0.0062(2)	
Catalyst before addition of BQ (substrate 2)	Pd–O	1.0	2.05(1)	0.003(2)	0.92(8)
	Pd–Pd	7.0	2.734(3)	0.0042(6)	
Catalyst after addition of BQ (re-activation)	Pd–O	0.6	2.05(4)	0.002(6)	0.9(1)
	Pd–Cl	0.6	2.35(3)	0.004(4)	
	Pd–Pd	7.0	2.726(5)	0.0064(8)	
Catalyst after addition of BQ (prevention of deactivation)	Pd–N/O	1.5	2.011(8)	0.002(2)	0.84(7)
	Pd–Cl	1.5	2.303(6)	0.003(1)	
	Pd–Pd	1.5	2.731(6)	0.0075(7)	

5.3 Recycling results and discussion

Recycling experiments were conducted to confirm the activity of the catalyst at different conditions. The catalyst was first examined by catalyzing substrate **1** for a few cycles and the result is summarized in Table 5.2. The activity of the catalyst retained until the fourth cycles, which agrees well with the conclusion from XAS analysis, showing that recycled **1** contained a significant amount of Pd(II) complexes.

***Table* 5.2.** *Recycling of the catalyst with substrate **1**.*

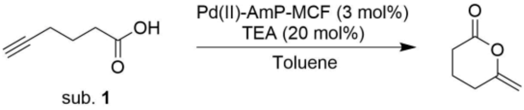

Cycle	NMR Yield (%)
1	78
2	74
3	75
4	25
5	34

On the other hand, the catalyst was not able to efficiently catalyze substrate **2** for the first cycle and became completely inactive in the second cycle, as shown in Table 5.3. The XAS analysis revealed that a large amount of metallic Pd aggregates were formed from the Pd(II) complexes when catalyzing substrate **2**. This transformation could be confirmed as the cause of the deactivation.

***Table* 5.3.** *Recycling of the catalyst with substrate **2**.*

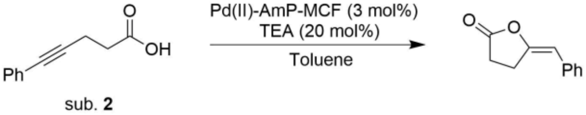

Cycle	NMR Yield (%)
1	42
2	<5

Recycled **1** and **2** were then used to catalyze 4-pentynoic acid, substrate **3**, which had a faster conversion rate, and the reactions were performed in the standard cycloisomerization condition reported.[112] The results showed that recycled **2** had lower activity than recycled **1** (Table 5.4, entries 1–2). Recycled **1** and **2** were then treated with 1 mol% of BQ which exhibited enhanced activities when catalyzing substrate **3** (Table 5.4, entries 3–4). Moreover, recycled **1** and **2** were also examined under the condition where 1 mol% of BQ was added to both substrates at the beginning. The results showed that the catalyst retained a high activity in the presence of BQ. The information here is consistent with the XAS analysis above where no obvious reduction occurred when BQ was present from the start.

*Table 5.4. Cycloisomerization of substrate **3** using recycled catalysts **1** and **2**.*

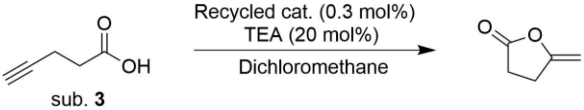

Entry	Catalyst	NMR Yield (%)
1	**1**	90
2	**2**	77
3[a]	**1**	99
4[a]	**2**	95
5[b]	**1**	99
6[b]	**2**	99

[a] 1 mol% of BQ used to reactivate the catalyst before the reaction.

[b] 1 mol% of BQ added in the beginning of the reaction.

5.4 Conclusion

In this work, the deactivation and reactivation of the Pd(II)-AmP-MCF catalyzed cycloisomerization of acetylenic acids were investigated by using mainly *in situ* XAS. It was found that the choice of the substrate significantly determined the change in the Pd species and further the activities of the recycled catalysts. Metallic Pd aggregates were proven to be the inactive catalytic species and TEA was found to be the reducing agent. Treatment of the deactivated catalyst with BQ was able to reactivate the catalyst by recovering a fraction of the Pd to active Pd complexes. Furthermore, a strategy for preventing the deactivation was designed by adding BQ to the catalyst and substrate **2** at the beginning of the reaction. Under this condition, the reduction of Pd was effectively prevented, and Pd was mainly retained in the form of complexes which exhibited high activities.

6 XAS Studies of Pd-AmP-MCF and Pd-CalB CLEA Heterogeneous Catalysts (Papers IV–V)

6.1 Introduction

In this chapter, two types of attractive heterogeneous Pd catalysts are discussed: Pd nanoparticles supported on siliceous mesocellullar foam, Pd(0)-AmP-MCF, and Pd nanoparticles supported on cross-linked CalB enzyme aggregates, Pd(0)@CalB CLEA. Both catalysts have been extensively studied in Bäckvall's group at Stockholm University. The procedures to synthesize the catalysts are described in Figure 6.1. Essentially, the catalyst supports were prepared first, following by impregnations of Pd(II) precursors. The Pd(II) pre-catalysts were then reduced by reducing agents generating supported Pd nanoparticles heterogeneous catalysts.

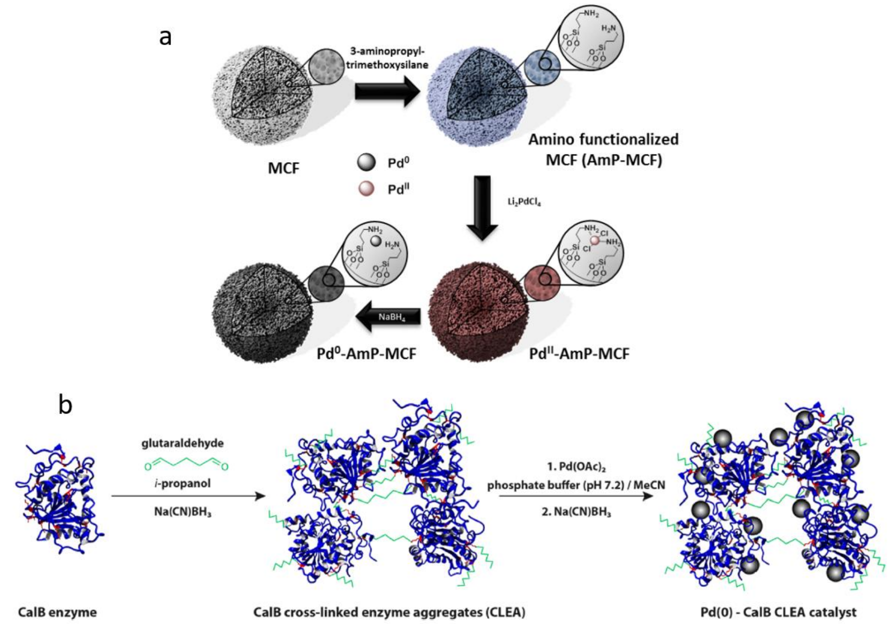

Figure 6.1. Synthesis of (a) Pd(0)-AmP-MCF (Reprinted with permission from *Chem. Eur*. 2017, 23 (52), 12886–12891. Copyright (2017) John Wiley and Sons.) and (b) Pd(0)@CalB CLEA heterogeneous catalysts. (Reprinted with permission from *ACS Catal*. 2017, 7 (3), 1601–1605. Copyright (2017) American Chemical Society.)

Pd0-AmP-MCF has been used as an effective catalyst in a wide range of reactions, such as water and alcohol oxidation, and the catalyst exhibited good recyclability with low metal leaching.[114–119] Pd(0)-CalB CLEA was successfully applied in a cascade reaction. The immobilized Pd catalyzed 4-pentynoic acid forming *exo*-cyclic vinyl lactone which was then utilized in a CalB-catalyzed kinetic resolution of sec-alcohols.[120]

TEM has been used as the standarded characterization technique to investigate the Pd nanoparticles in the Pd(0) catalysts. To gain a better understanding of the synthesis process, XAS was used to characterize both the Pd(II) pre-catalysts and the reduced Pd(0) catalysts. Moreover, the influence of different reaction conditions on the Pd species in the catalysts was also unveiled by XAS.

6.2 EXAFS study of Pd(II/0)-AmP-MCF

The specific coordination environments of Pd atoms in Pd(II/0)-AmP-MCF were probed by EXAFS. The EXAFS spectra and corresponding FTs are shown in Figure 6.2, and the refinement results are summarized in Table 6.1. Obviously, the main envelope positions of Pd(II) and Pd(0)-AmP-MCF are different indicating a significant difference of the backscattering atoms in these two catalysts. FTs of Pd(II)-AmP-MCF consists of two main peaks at the positions typical for Pd–N and Pd–Cl single scattering. The N donor ligands are the functionalized amino groups on the support, and Cl^- ions originate from the catalyst precursor, Li_2PdCl_4. Each Pd atom was on average bound to two N–ligands and two Cl^- ions at mean distances of 2.02 Å and 2.29 Å, respectively. A square-planar complex in *trans* geometry was preferred in the model fitting. Meanwhile, a peak at ca. 3.0 Å (without phase correction) was observed, and the refinement suggested Pd---Pd single scatterings at 3.07 Å and 3.42 Å. These results depicted a scenario of mononuclear $Pd(R–NH_2)_2Cl_2$ complexes embedded on the MCF support. The complexes were likely stacked on top of each resulting in Pd---Pd distances of 3.07 Å and 3.42 Å.

FTs of Pd(0)-AmP-MCF changed significantly in comparison to Pd(II)-AmP-MCF after the reduction, and displayed only one dominating peak corresponding to Pd–Pd single scattering in metallic palladium. Refinement revealed that each Pd atom on average was bound to ca. 6 Pd atoms, and the bond length was determined at 2.78 Å. The Pd–Cl contribution disappeared completely and the peak at ca. 2.0 Å (without phase correction) was actually attributed to the satellite peak of Pd–Pd single scattering. The signal of Pd–N became much less pronounced in the reduced catalyst, and a coordination number of ca. 0.7 with a distance of 2.00 Å gave the best fit. Considering the sample was exposed to air, the Pd nanoparticles could be partially oxidized or hydrolyzed. The bond at 2.00 Å could also be Pd–O or a mixture of Pd–N and Pd–O, which are not possible to resolve by EXAFS. Due to the presence of multiple species and the averaging nature of the EXAFS data, the real coordination number of Pd in the nanoparticles should be larger than 6. This was also reflected by the fairly long bond distance in comparison to the Pd nanoclusters as discussed in Chapter 3. The same principle was also applicable for estimating the real coordination number of Pd–O/N. TEM imaging confirmed the formation of Pd nanoparticles with a typical size of 2.5 nm in diameter. The nanoparticles were well distributed and covering the entire observing sample area. Importantly, it was proven that the reduction of the Pd(II) catalyst was effective, and Pd nanoparticles were the dominating species in this catalyst with a small fraction of PdO and even some Pd complexes.

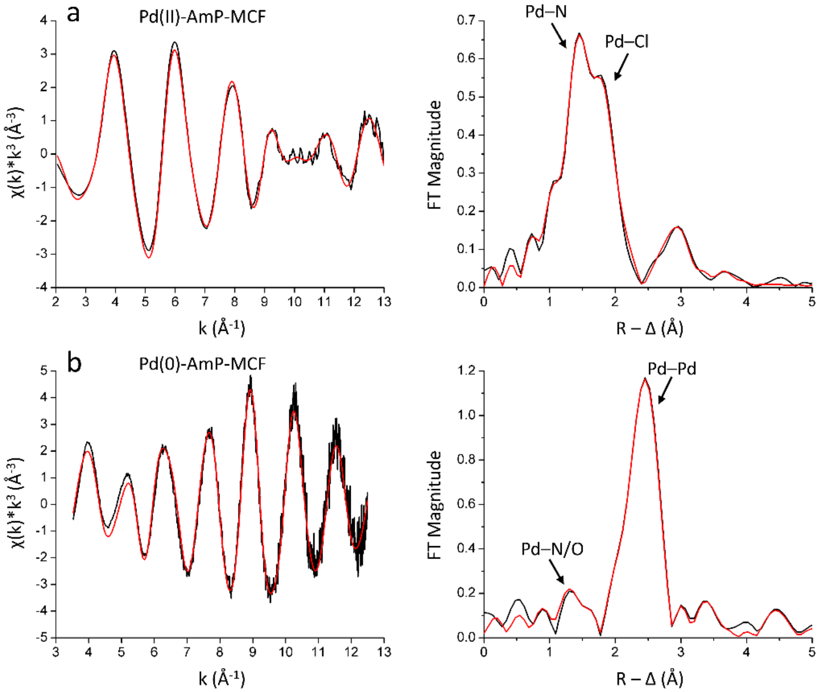

Figure 6.2. Pd K-edge EXAFS spectra (left) and Fourier transform data (right) of (a) Pd(II)-AmP-MCF and (b) Pd(0)-AmP-MCF. The single scatterings in the first coordination shell are assigned. Black curve – experimental, red curve – model. The spectra are not phase corrected. (Reprinted with permission from *Chem. Eur.* 2017, 23, 12886–12891. Copyright (2017) John Wiley and Sons.)

Table 6.1. Number of distances, N, mean distances, d/Å, and Debye-Waller coefficients, σ^2/Å^2, in the EXAFS studies of solid Pd^{II}-AmP-MCF and Pd^0-AmP-MCF at room temperature. The standard deviations in parentheses were obtained from k^3-weighted least square refinement of the EXAFS function χ(k) and do not include systematic errors of the measurement. Underscored parameters were optimized from several trials and were fixed in the individual refinements. (Table adapted from Paper IV.)

Samples	*Signal*	*N*	*d*	σ^2	S_0^2
Pd(II)-AmP-MCF	Pd–N	2.0	2.023(2)	0.0035(3)	0.93(2)
	Pd–Cl	2.0	2.294(2)	0.0058(2)	
	Pd---Pd	0.5	3.065(5)	0.0083(4)	
	Pd---Pd	1.0	3.415(6)	0.0094(4)	
	MS ($PdCl_2$)	2.0	4.59(2)	0.007(2)	
Pd(0)-AmP-MCF	Pd–O/N	0.7	1.995(4)	0.0048(4)	0.84(2)
	Pd–Pd	5.5	2.779(1)	0.0093(1)	
	Pd---Pd	2.0	3.85(1)	0.016(1)	

6.3 XAS study of Pd(II/0)-CalB CLEA and influence of the solvents in catalytic reactions

Using a similar approach, we also studied the synthesis of Pd(0)-CalB CLEA. Pd(II)-CalB CLEA pre-catalyst was prepared first which then was reduced to form Pd(0)-CalB CLEA. To study the effect of the reducing agents on the resulting Pd species, $NaBH_3CN$ and $NaBH_4$ were utilized, respectively, and the reduced catalysts were studied by XAS. The XANES spectra of these samples, together with a Pd foil as the metallic Pd reference, are shown in Figure 6.3. The Pd K-edge position of Pd(II)-CalB CLEA is ca. 4 eV above the Pd foil, which is the typical edge position for a Pd(II) compound. This means that the Pd in the pre-catalyst is retained as Pd(II) after the immobilization of the Pd(II) precursor. The edge positions of the catalysts after the reduction exibit an obvious shift towards lower energy, but still above the Pd reference foil. The reduction occurred without that any other strong electron donors were present in the reaction systems. Meanwhile, it seems that a relatively small amount of Pd was not effectively reduced, which was observed in both reduced catalysts. As the main profile feature of the XANES spectrum of the pre-catalyst, the smooth peak after the absorption edge became flatten after the reductions and empirically represented by the formation of metallic Pd species. The features were, however, not as pronounced as the Pd foil or the Pd nanoparticles, indicating multiform coordination environments of the Pd atoms in the reduced catalysts. The Pd species in these two catalysts are expected to be similar based on the minor differences of their XANES spectra.

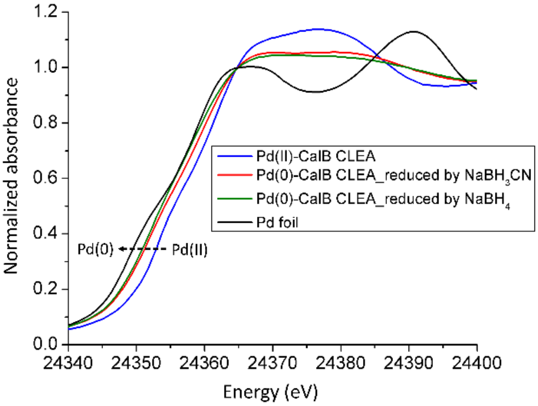

Figure 6.3. Pd K-edge XANES spectra of the pre-catalyst and the reduced catalysts using different reducing agents, as well as the Pd foil.

The EXAFS data of these samples were then analyzed and their FTs with the best fit are presented in Figure 6.4. The refinement of the pre-catalyst suggests that each Pd atom on average binds four ligands at a mean bond length at 2.034 Å. The bond length agrees well with oxygen, nitrogen and carbon donor ligands from the enzyme support. Distances between the Pd atoms and the enzyme support were also found at distances longer than 3.0 Å. Their back FTs imply that the backscattering atoms are lighter than Pd, which indicates the successful impregnation of $Pd(OAc)_2$ onto the support. For the catalysts after the reduction treatments, two pronounced peaks are presented in their FTs as shown in Figure 6.4b-c and they correspond to Pd–C/N/O and Pd–Pd bonds, respectively. Pd–Pd bonds with a mean distance of 2.72 Å in these two catalysts confirmed the formation of metallic Pd species and they were in the form of nanoparticles as further characterized by TEM. The contribution from Pd–C/N/O distances to the EXAFS function is more significant in the enzyme supported catalyst than in the one supported on MCF as shown in Figures 5.2b and 6.4b-c. One explanation is that the Pd(II) species in the pre-catalyst was not completely reduced. Re-oxidation of the Pd nanoparticles is another possible scenario as the catalyst was stored and measured in air. The average number of Pd–Pd distances in the catalyst reduced by $NaBH_4$ was refined to a slightly higher value than the catalyst reduced by $NaBH_3CN$, while their σ^2 values are comparable. XPS measurement on these two catalysts also showed the same difference as the analysis of XAS. However, these two reduced catalysts had comparable compositions in general.

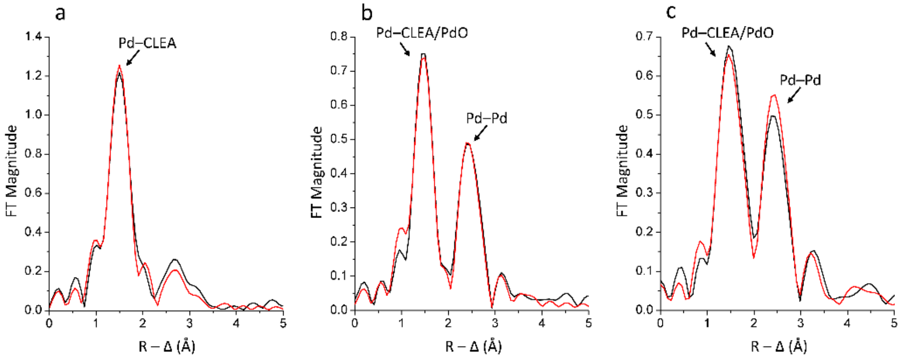

Figure 6.4. Fourier transformed k^3-weighted EXAFS data and the best fit of (a) the pre-catalyst, (b) the catalyst reduced by $NaBH_3CN$, and (c) the catalyst reduced by $NaBH_4$. The single scatterings in the first coordination shell are assigned. Black curve – experimental, red curve – model. The spectra are not phase corrected.

Pd(0)-CalB CLEA reduced by $NaBH_4$ was then used in the DKR of 1-phenylethylamine. This catalyst was found to have a higher activity which might be due to the slightly larger fraction of Pd(0) species. Deactivation occurred when 1,4-dioxane was used as the solvent and the recycled catalyst was studied by XAS. Tetrahydrofuran (THF) was another solvent used during the solvent optimization experiments although recyclability of the catalyst was not specifically studied. The XANES spectra of the recycled catalyst in these two solvents are shown in Figure 6.5, together with the catalyst before the reaction and the Pd foil. The peak shape after the edge altered from the unused catalyst to the recycled catalyst from 1,4-dioxane. Interestingly, the spectrum of the catalyst recycled from THF exhibited split peaks resembling the Pd foil. This observation suggests metallic Pd species became dominating. Meanwhile, the edge positions of the recycled catalysts moved closer to the Pd foil indicating a further decrease of the average oxidation state of the Pd atoms.

EXAFS analysis was employed on these two recycled catalysts and the FTs are shown in Figure 6.6. The relative intensities of Pd–C/N/O became lower in comparison to the fresh catalyst suggesting a decreased fraction of such component. For the recycled catalyst from dioxane, the bond distance of Pd–Pd was determined to be 2.75 Å, which obviously is longer than in the fresh catalyst and in the range of a bulk metal, which implies relatively large average particle size of Pd. TEM also detected larger aggregates. To our surprise, a pronounced peak at ca. 1.8 Å (without phase correction) emerged as shown in Figure 6.6a. The distance was refined to 2.29 Å and the average number of this distance is 1.0. The distance agrees with a Pd–Cl or Pd–S bond. S-XPS measurement showed no significant change between the fresh catalyst and the recycled catalyst. Therefore, this peak could be attributed to the Cl^- from impurity. Meanwhile, Pd leaching was found to be a minor issue. The overall large particle size and maybe also the chloride contamination should be the source of the dramatic decrease of the catalytic activity.

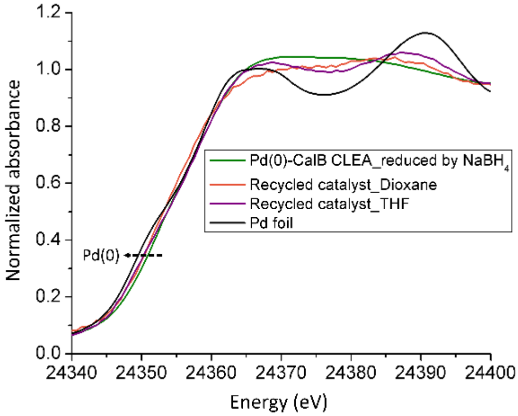

Figure 6.5. Pd K-edge XANES spectra of the catalyst reduced by $NaBH_4$, recycled catalysts from 1,4-dioxane and THF, and the Pd foil.

When using THF as the solvent, the FTs of the recycled catalyst exhibits a dominating peak corresponding to Pd–Pd bonds, and a relatively small peak is related to Pd–C/N/O bonds. The Pd–Pd bond distance was refined to 2.77 Å, which is considerably longer than the fresh catalyst and even the Pd foil. Two different Pd–C/N/O single scattering paths with distances of 1.89 Å and 2.04 Å were introduced to refine the first two minor peaks in Figure 6.6b. Although the recyclability experiment and TEM characterization were not conducted, one can predict that the activity of the catalyst using THF could diminish substantially based our estimated large Pd particle size.

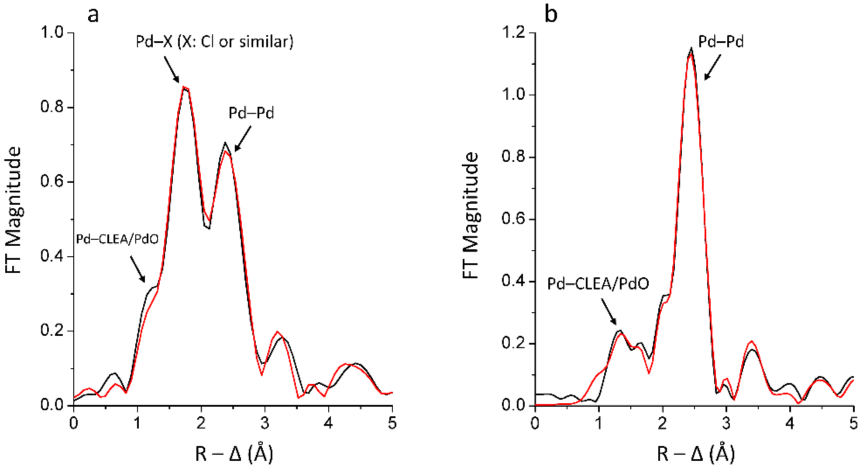

Figure 6.6. Fourier transformed k^3-weighted EXAFS data and the fit of the recycled catalysts from (a) 1,4-dioxane and (b) THF. The single scatterings in the first coordination shell are assigned. Black curve – experimental, red curve – model. The spectra are not phase corrected.

Table 6.2. *Number of distances, N, mean distances, d/Å, and Debye-Waller coefficients, σ^2/Å^2, in the EXAFS studies of the catalyst. The standard deviations in parentheses were obtained from k^3-weighted least square refinement of the EXAFS function $\chi(k)$ and do not include systematic errors of the measurement. Underscored parameters were optimized from several trials and were fixed in the individual refinements. (Table adapted from Paper V.)*

Samples	*Signal*	*N*	*d*	*σ^2*	S_0^2
Pd(II)-CalB CLEA	Pd–N/C	4.0	2.034(2)	0.0038(2)	1.03(3)
	Pd---N/C	4.0	3.331(7)	0.0093(8)	
	Pd---N/C	4.0	3.92(2)	0.012(2)	
Pd(0)-CalB CLEA (reduced by $NaBH_3CN$)	Pd–N/O	2.5	2.032(2)	0.0053(3)	0.99(3)
	Pd–Pd	3.0	2.719(3)	0.0122(3)	
	Pd---C/N/O	2.0	3.97(3)	0.010(1)	
	Pd---Pd	1.5	3.87(4)	0.019(6)	
	Pd---Pd	5	4.73(3)	0.031(7)	
Pd(0)-CalB CLEA (reduced by $NaBH_4$)	Pd–N/O	2.5	2.050(3)	0.0055(5)	0.94(4)
	Pd–Pd	3.5	2.715(3)	0.0118(4)	
	Pd---Pd	2.0	3.81(1)	0.016(1)	
	Pd---Pd	5.0	4.77(1)	0.018(1)	
Recycled Pd(0)-CalB CLEA (Reaction in dioxane)	Pd–N/C	1.0	2.04(2)	0.007(4)	0.89(9)
	Pd–Cl*	1.0	2.292(8)	0.003(1)	
	Pd–Pd	3.0	2.748(5)	0.0092(8)	
	Pd---Pd	1.5	3.79(1)	0.006(2)	
	Pd---Pd	5.0	4.72(2)	0.015(3)	
	Pd---N/C/O	3.0	4.21(2)	0.002(3)	
Recycled Pd(0)-CalB CLEA (Reaction in THF)	Pd–N/C	0.6	1.892(6)	0.0018(6)	0.82(2)
	Pd–N/C	1.0	2.044(4)	0.0017(4)	
	Pd–Pd	7.0	2.766(1)	0.0102(2)	
	Pd---Pd	3.0	3.836(4)	0.0113(4)	
	Pd---Pd	10.0	4.53(2)	0.025(2)	

*Backscattering atom could be Cl and/or atoms with similar size as Cl.

6.4 Conclusion

In this chapter, two types of heterogeneous Pd catalysts were explored, Pd-AmP-MCF and Pd-CalB CLEA. They are good examples to demonstrate the application of XAS to investigate the preparation of catalysts. Another conclusion of this XAS study is that it provides experimental evidence at atomic level that the choice of the solvent has a significant influence on the catalytic species, which further affects the recyclability. These observations can provide a guide for optimization strategy of a catalytic system.

7 *In Situ* Structure Determination of a Homogeneous Ruthenium Catalyst and its Activated Intermediates using XAS (Paper VI)

7.1 Introduction

Catalyst activation is an important process in many catalytic reactions and understanding the activation mechanism is beneficial to the development of new catalysts. However, explorations of the catalyst activation have been limited to computational[121,122] or experimental approaches, such as FT-IR and NMR,[123,124] which cannot probe the catalytic metal center directly. Meanwhile, the reaction intermediates are often transient and time-resolved techniques are necessary to capture these species. With proper manipulation of the reaction system, it has become possible to accumulate these intermediates and extend their lifetime for detection. Traditional methods, such as single-crystal X-ray diffraction, are powerful to determine the structures of the pre-catalysts. This technique, on the other hand, is limited when studying the structure of intermediates due to the difficulties to isolate and recrystallize pure intermediates. *In situ* XAS provides opportunities to probe the local structures of catalytic metal centers directly in real activation processes and in a time-resolved manner.

Metal-carbonyls are a type of common complexes in organometallic chemistry. They are widely used as reagents or catalysts in organic synthesis.[125] Dicarbonyl pentaphenylcyclopentadienylruthenium chloride (**1a**) is a transfer hydrogenation catalyst which was used as an effective racemization catalyst in DKR of a wide range of alcohols.[126–129] There have been many discussions of the mechanism for the hydride transfer of alcohols with **1a** and its related complexes.[121,122,124,130,131] Currently, the accepted mechanism proposes an activation step and it is described in Scheme 7.1.[125,127,132] First, potassium *tert*-butoxide is added to **1a** to produce an activated complex **3**. A sec-alcohol is then introduced to initiate an alcohol-alkoxide exchange forming the alkoxide complex **4**. **4** is an 18-electron complex which means a vacant site on Ru is required for the subsequent β-hydride elimination step. It has been proposed that a CO dissociation leads to a vacant site on Ru and β-hydride elimination generates a complex *Int*-**1**. The final Ru alkoxide complex *rac*-**4** is formed through hydride re-addition to the ketone and a CO coordination.

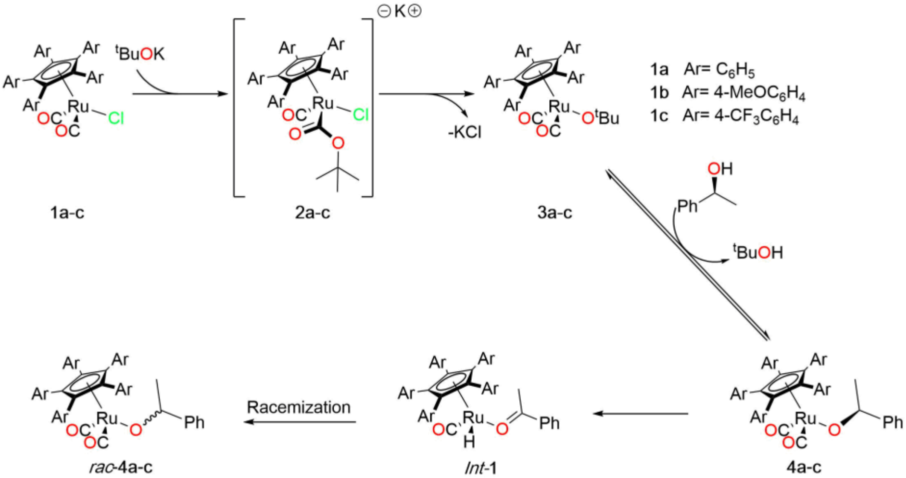

Scheme 7.1. Proposed mechanism of catalyst **1a** for racemization of sec-alcohols.

In earlier studies of the catalyst activation, computation suggested an acyl intermediate **2a** as depicted in Scheme 7.1. This intermediate was then detected experimentally by using *in situ* FT-IR under cryogenic condition. ^{13}C-NMR at low temperature also showed signals matching the acyl intermediate.[124]

7.2 *In situ* characterizations of the catalyst activation

7.2.1 The choices of the solvent and the Ar- group for optimal *in situ* measurements

Previously, *in situ* IR measurement of acyl intermediate **2a** had only been performed in toluene.[124] Based on an improved understanding of the reaction conditions, THF was used in the present study as it allows more catalysts to be dissolved resulting in a higher S/N ratio. This is particularly beneficial when it comes to XAS measurement using the *in situ* batch reactor in Figure 2.15.

Another merit of using THF is that it prolongs significantly the lifetime of **2a** without changing the reaction pathways. It was found that full conversion of **3a** can be achieved in less than 5 min in toluene, which is a limited amount of time for data collection. It also becomes more difficult to collect a sufficient amount of data to gain a full picture of the structural transformation. THF, on the other hand, slows the transformation of **1a** properly down to ca. 1 h giving us sufficient time to collect sufficient amount of data of good quality and quantity.

Besides the influence of the solvent, the Ar- group also plays an important role in the activation rate. 4-$MeOC_6H_4$ in **b** has a stronger electron donating ability to Ru than C_6H_5 in **a** leading to a higher electron density of Ru, while 4-CF_3-C_6H_4 in **c** has an electron withdrawing effect and lowers the electron density of Ru. Hence, a promoted reaction rate is expected in the case of **b**, and the reaction should be suppressed using **c**. **a,** as a compromised substitute, was chosen as the model for the *in situ* measurement due to the adequate XAS data collection time. The effect of the substitute Ar-groups was investigated by *in situ* XAS and are elaborated in the XAS discussion.

7.2.2 *In situ* IR measurements

In situ IR measurements were performed, and the results were compared with the previous studies in toluene.[124] The activation process followed the same mechanism when different solvents were used. The observed bands are assigned to the complexes in Scheme 7.1. Figure 7.1 shows the *in situ* IR spectra of the activation process. It can be seen that **1a** disappeared instantly when *tert*-BuOK (^{t}BuOK) was added, meanwhile **2a** emerged. This was followed by a gradual growth of **3a**. When the substrate, 1-phenylethanol, was added, the signals of the carbonyls in **3a** blueshifted rapidly to positions matching **4a** as shown in the supporting information of Paper VI.

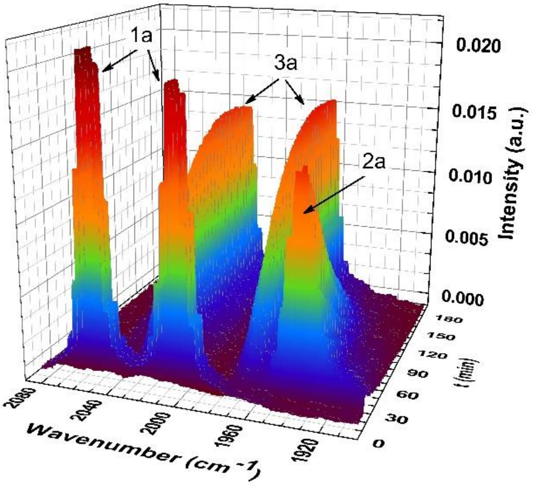

Figure 7.1. (a) *In situ* IR spectra of the activation of **1a** in THF through the addition of *tert*-BuOK.

7.2.3 *In situ* XAS measurements

The catalysts (0.1 mmol) were dissolved in 1.8 mL of dry THF and *tert*-BuOK (0.1 mmol) was then mixed after acquiring the first XAS spectrum. The XAS data were collected in transmission model at Ru K-edge which was assigned at 22117 eV.[12] A typical energy range from 200 eV below the K-edge up to 800 eV above the K-edge was used for the measurements. A time resolution of 5 min was chosen considering the S/N ratio and the reaction rate. Each XAS scan was internally calibrated with a Ru foil which was measured simultaneously with the catalyst. All the XAS spectra were collected at beamline P64, Petra III Extension, Deutsches Elektronen-Synchrotron (DESY), Hamburg, Germany. More details of the XAS experiments can be found in the supporting information of Paper VI.

Before the XAS measurements were performed on the catalysts under reaction conditions, the role of the solvent in triggering the activation was examined. **1a** was dissolved in both toluene and THF and their Ru K-edge XANES spectra were in principle identical to the dry **1a**. This indicates that **1a** retained the same structure in the solvents. Moreover, **1a**, **1b** and **1c** were all dissolved in THF and they all displayed very similar XANES spectra. It suggests that the local environment of Ru in these complexes were the same and the spectra could not probe the differently substituted cyclopentadienyl (Cp) ligands. The edge position of the dissolved catalyst was determined to 22125 eV verifying that the oxidation state of Ru was +II.

After gaining an understanding of the catalysts under static conditions, *in situ* XAS measurements were performed on the catalysts and XAS spectra in full range were collected every 5 min. Figure 7.2 shows the *in situ* Ru K-edge XANES spectra of **1a** (a) and **1b** (b) during the activation process. *tert*-BuOK, which was expected to trigger the activation, was added remotely after collecting the first spectrum. The spectra in bright colors were collected when the pre-catalyst was under the activation conditions. One additional spectrum after the addition of 1-phenylethanol to **1a** and **1b** was also recorded; these spectra are displayed in purple. An instant change occurred upon the addition of *tert*-BuOK. The prominent peak at ca. 22158 eV in **1a** (black line) almost disappeared 5 min into the measurement, which is a strong indication of a structural alternation around Ru. This “vanished” peak, however, gradually returned and increased in intensity in the following XAS scans. It stabilized in ca. 45 min with a slight shift to ca. 22160 eV and a lower intensity compared with the dry catalyst. Meanwhile, the first peak after the absorption edge also had a minor loss in intensity after the addition of *tert*-BuOK with a modest shift towards higher energy. These observations confirmed that Ru in **1a** underwent a sudden and significant change in the local structure when *tert*-BuOK was added. The altered structure slowly reverted to a configuration similar to the dry **1a**, yet not identical. Over the course of the activation, only minor changes in the edge positions were observed, which indicates that Ru retained the oxidation state +II.

Comparable changes were observed in the activation process of **1b** as shown in Figure 7.2b, which supported the generality of the structural evolution in this type of catalysts. Interestingly, it took only ca. 25 min for the “vanished” peak in **1b** to regain the intensity, and the reaction rate is obviously faster than the case of **1a**. This clearly shows the effect of the electron-rich substitute on the reactivity of the Ru center. In the case of **1c**, the addition of *tert*-BuOK still triggered the sudden disappearance of the peak at ca. 22158 eV. Nevertheless, the recovery of peak intensity was greatly suppressed and no obvious progress was observed even after one day. This is certainly caused by the electron-poor substitute as discussed above. It can be concluded that the first step of the activation process as shown in Scheme 7.1 occurred immediately and the same mechanism can be applied to all three catalysts as their spectra at 5 min are very similar. On the other hand, the reaction rate of the latter step of the activation was found to be highly dependent on the electron properties of the ligands, but it has no influence on the reaction path.

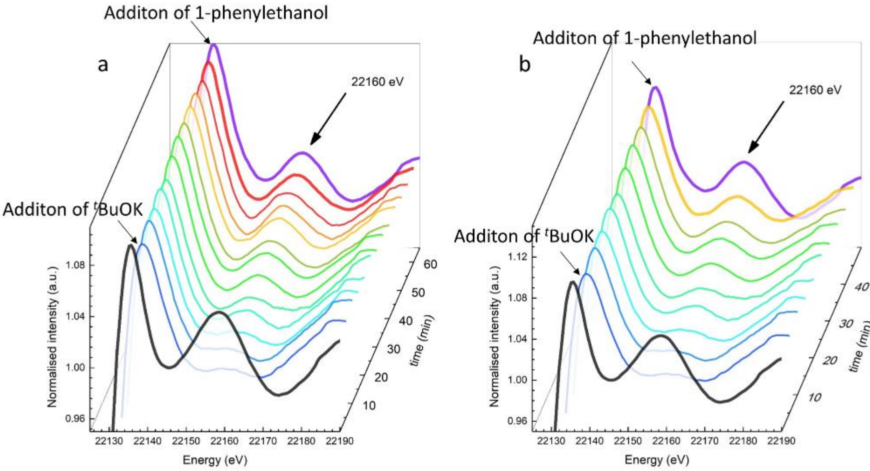

Figure 7.2. Normalized *in situ* Ru K-edge XANES spectra of (a) **1a** and (b) **1b** during the activation processes. The first spectra in black are catalysts before the reaction, and the last spectra in purple are spectra of the catalysts after the addition of 1-phenylethanol.

The pronounced changes of the characteristic peak at ca. 22160 eV in Figure 7.2 were further utilized to extract the reaction rates and to determine the half-life time, $t_{1/2}$, for the catalysts during the activation reaction. The normalized intensities of this peak as a function of the measurement time are shown in Figure 7.3 for both **1a** and **1b**. $t_{1/2}$ of the intermediate **2** in Scheme 7.1 was calculated at 28 min for **1a** and 6 min for **1b** under the current condition, while it was impossible to conduct calculation for **1c** with the acquired data.

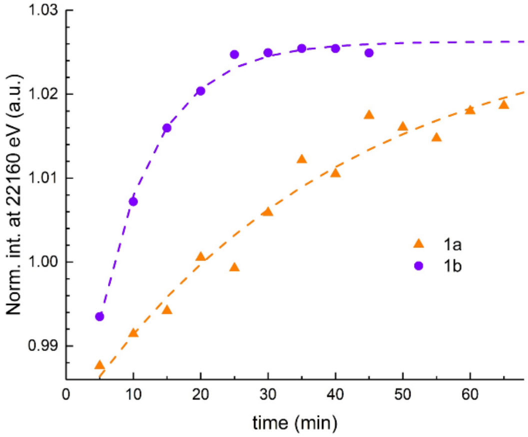

Figure 7.3. Normalized intensities of the peak at 22160 eV in Figure 7.2 as a function of measurement time during the activation reaction of **1a** and **1b**.

Moreover, a marginal change in the pre-edge feature was noticed. Upon the addition of *tert*-BuOK after 5 min, the pre-edge feature of **1a** became slightly more distinct as pointed out by the upward arrow in Figure 7.4a. This feature then decreased over the time of the experiment. This pre-edge feature can be correlated to the symmetry of ligands around Ru, and it decreased from the symmetrical **1a** to **2a**, and recovered to some extent when proceeding to **3a**.[133] Similar changes were also observed in **1b** as shown in Figure 7.4b. Basically, the minor changes of the pre-edge showed good consistency with the observation after the absorption edge and strengthened the conclusions discussed above.

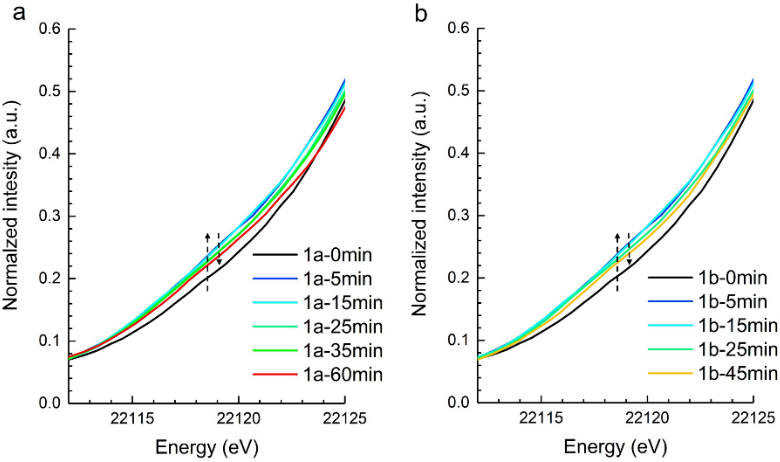

Figure 7.4. Normalized *in situ* Ru K-edge XANES spectra of (a) **1a** and (b) **1b** with a focus on the pre-edge area.

The specific coordination environments of Ru during the activation process were elucidated by analysis of the EXAFS data. Using the same strategy as in the discussion of the XANES spectra, FTs of the dissolved **1a** in both toluene and THF were compared as a starting point with the catalyst in the solid state showing similar features. This means that the structure of Ru was intact when it was dissolved in the solvents. The refinement of their EXAFS spectra revealed that the overall bond lengths between Ru to the ligands in the solvents were slightly longer than the dry state. This could be attributed to the solvation effect of the dissolved **1a**.

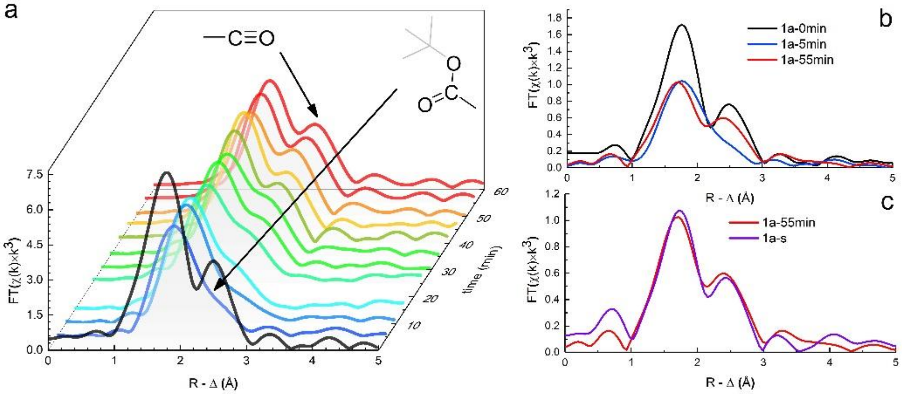

Figure 7.5. Fourier transformed k^3-weighted EXAFS data of the activation process of 1a. (a) All FTs displayed in three dimensions. (b) Selected FTs focusing on **1a** at 0 min (**1a**), 5 min (**2a**) and 55 min (**3a**). (c) FTs of **1a** at 55 min (**3a**) and the catalyst upon the addition of the 1-phenylethanol. The k range applied is 2–10 Å^{-1}, and the FTs are not phase corrected.

Activation of **1a** in THF was then chosen as the model reaction and the main results of the EXAFS refinements are summarized in Table 7.1. FT of **1a** in THF can be basically described with two peaks as shown in Figure 7.5. The peak at ca. 1.8 Å (without phase correction) was actually a result of three different single scattering events: Ru to C in CO ligand, Ru to C in Cp ring, and Ru to Cl (see Scheme 7.1). Their bond lengths were refined to 1.906(5), 2.240(8) and 2.436(8) Å, respectively, which are consistent with the bond lengths determined from the single crystal data of **1a**.[126] The other distinct peak appeared at ca. 2.5 Å (without phase correction) and it corresponds to the Ru---O (CO ligand) single scattering and Ru–C–O multiple scatterings (CO ligand). The intensity of the multiple scatterings was enhanced due to the focusing effect when the atoms involved are in a linear or close to a linear configuration. The distance was refined to 3.045(6) Å. Figure 7.5a shows the FTs of **1a** during the activation process and they correspond to the XANES spectra in Figure 7.2a. A prominent change was captured as well in FTs at 5 min as shown in Figure 5a-b. Firstly, the overall intensity decreased and this could be explained by the increased Debye-Waller coefficients from 0 to 5 min. Another change is that the second distinct peak diminished substantially in intensity at 5 min, and this indicates the loss or replacement of a CO ligand. The Cp ring, Cl^- ligands were retained according to the refinement as well as the Ru to C single scatterings. However, the number of multiple scattering among Ru and CO was refined to 1. This difference suggests that one of the CO ligands was likely replaced by another ligand, which didn't have the linear configuration, such as the acylester depicted in **2a** (Scheme 7.1).

The observation here is a direct experimental proof of the immediate replacement of CO ligand at atomic level. From 5 min and onwards, the intensity of the peak at ca. 1.8 Å (without phase correction) corresponding to the CO ligand gradually increased and became more and more distinct. This is an indication of that the substituted CO ligand re-bind to Ru. At the same time, the refinement showed that the Cl$^-$ ligand dissociated from Ru. At the end of the experiment, the best fit of the EXAFS spectrum suggested that on average each Ru atom was bound to one Cp ring, two CO ligands, and an additional ligand likely to be O– from *tert*-BuO. The structure agreed well with the active **3a** proposed in Scheme 7.1. Based on the refinements and the knowledge of the reaction, structure models of **1a** before the activation, the intermediate **2a,** and the active state **3a** as shown in Figure 7.6.

Table 7.1. *Refined distances (d/Å), mean number of distances (N) and Debye-Waller factor (σ^2/Å^2) in selected scans of the activation of* ***1a****. The letters in bold indicate the backscattering atoms specifically. Underscored parameters were optimized from several trials and were fixed in the individual refinements.*

Samples	*Signal*	*N*	*d*	σ^2
1a – 0 min	Ru–Cp	5.0	2.240(8)	0.0016(9)
(in the form of 1a)	Ru–C≡O	2.0	1.906(5)	0.0018(6)
	Ru–C≡O	2.0	3.045(6)	0.0062(5)
	Ru–Cl	1.0	2.436(8)	0.0044(5)
1a – 5 min	Ru–Cp	5.0	2.27(1)	0.0089(9)
(in the form of 2a)	Ru–C≡O	2.0	1.86(1)	0.013(2)
	Ru–C≡O	1.0	3.01(2)	0.0093(9)
	Ru–C–O$_{Acyl}$	2.0	2.697(8)	0.00361(8)
	Ru–Cl	1.0	2.346(6)	0.0062(9)
1a – 55 min	Ru–Cp	2.0	2.697(8)	0.00361(8)
(in the form of 3a)	Ru–C≡O	1.0	2.346(6)	0.0062(9)
	Ru–C≡O	5.0	2.28(2)	0.004(1)
	Ru–O–^{t}Bu	2.0	1.894(5)	0.0057(7)

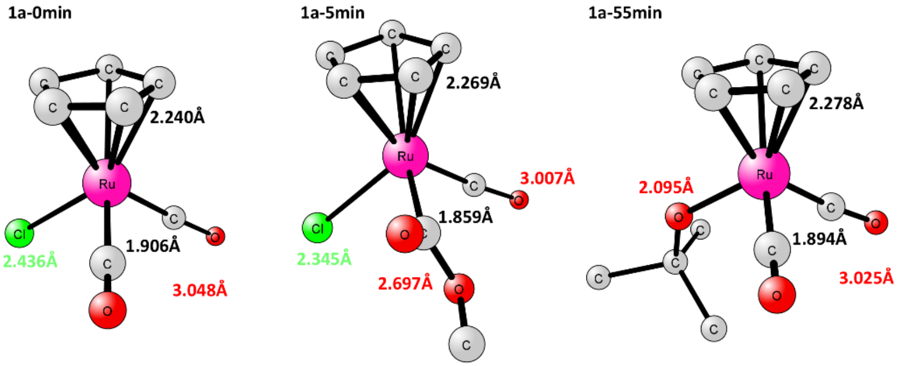

Figure 7.6. Structure models of **1a** at 0 min, 5 min (**2a**) and 55 min (**3a**) derived from the EXAFS refinement.

The EXAFS spectra of **1b** during the activation process exhibited similar patterns and trend of changes as shown in Figure 7.7a. The rate of the changes was faster for **1b**. The spectrum at 5 min shows the signals from **2b**. The possible coordination moieties were introduced to achieve good fit resulting in broken numbers of distances on average. The Debye-Waller factors generally were refined at large values, which could be caused by faster reaction and mixed species. The details can be found in the supporting information of Paper VI. The activation of **1c**, however, didn't proceed to the activated state. Figure 7.7b displays that **1c** went through a quick transformation into the intermediate **2c** at 5 min, but was thereafter inhibited. All these observations of EXAFS spectra were consistent with the corresponding XANES data.

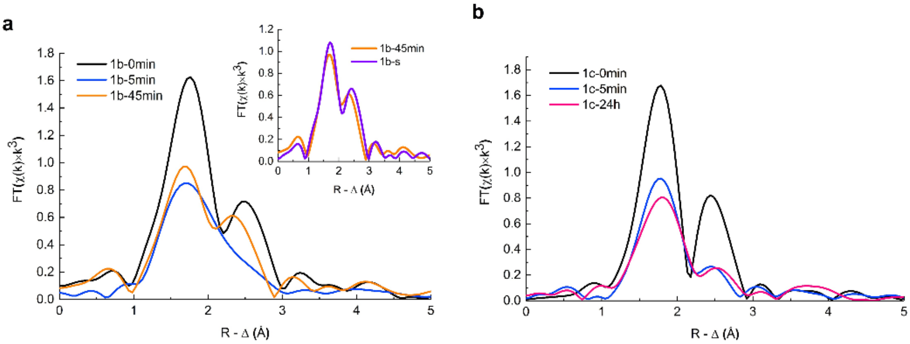

Figure 7.7. Selected Fourier transformed k^3-weighted EXAFS data of the activation processes of (a) **1b** and (b) **1c**. The inlet of (a) is the FTs of activated **1b** and catalyst upon the addition of the 1-phenylethanol. The *k*-range applied is 2–10 Å^{-1}, and the FTs are not phase corrected.

After characterizing the activation process of the pre-catalysts, the interaction of the activated catalysts and the substrate, 1-phenylethanol, was studied. The XANES spectra of the activated **a** and **b** mixed with the substrate are shown in Figure 7.2 (Purple color). The spectra resembled each other suggesting a similar structure. The refinement of their EXAFS spectra (Figure 7.5c and inlet of Figure 7.7a) further revealed that the hexa-coordination structure was retained after the catalytic reaction. Cp and two CO ligands were bound to Ru in both catalysts, while the last coordination site couldn't be confirmed. The uncertainty of the alkoxide ligand in the proposed **4a-b** seems an evidence of the dynamic equilibria with fast interconversions of the substrate molecules.

7.3 Conclusion

In summary, the present work demonstrated that *in situ* XAS is a suitable approach to elucidate the structures of a group of homogenous Ru catalysts during their activation stages. The intermediates were identified together with their oxidation state and changes to the structure around the Ru(II) ion. The effect of the substituted groups on Cp ligands on the activation process was studied. The results unraveled the promoting effect of the electron donating substitutes as in **2a** and the inhibitive effect of the electron withdrawing substitutes as in **2c**. In the racemization of 1-phenylethanol, a quick dynamic equilibrium was expected to be achieved leading to the averaged EXAFS data.

8 Concluding Remarks

This thesis illustrates the application of *in situ* X-ray absorption spectroscopy to probe the palladium and ruthenium species in several suspension and solution-based catalytic reactions.

The evolutions of catalytic species are discussed in Chapter 3 and 4. Pd(II) complexes immobilized on metal organic frameworks, Pd(II)@MOFs, and reduced graphene oxide, **1**@rGO, were used as heterogeneous catalysts to catalyze the Heck coupling reaction and undirected C–H acetoxylation reaction of benzene, respectively. Ligand substitutions occurred in both cases where Cl^- ligands bound to Pd in the as-synthesized catalysts were replaced by other ligands in the reaction mixture, but with different rates. At a later stage of the measurements, all the mononuclear Pd complexes in Pd(II)@MOFs are transformed into Pd nanoclusters. It turned out that Cl^- ions start to bind to the surface atoms of the Pd nanoclusters causing the deactivation of the catalyst. This transformation of Pd(II) to Pd nanoclusters takes also place in the rGO system, but in addition also Pd(IV) is formed in this system. The understanding of the deactivation mechanism of Pd(II)@MOF in the Heck coupling reaction allows the prolonging of the lifetime of the catalyst by adding new reagents before the Cl^- ligands start to bind to Pd.

The study of deactivation of the catalysts became interesting. Pd(II) complexes supported on amino-functionalized siliceous mesocellular, Pd(II)-AmP-MCF, catalyzed cycloisomerization of acetylenic acids is presented in Chapter 6. It was realized that the choice of substrate had a significant influence on the Pd species in the reaction. The Pd(II) complexes are reduced by trimethylamine forming Pd nanoparticles, and this process causes the deactivation of the catalyst. The activity is restored by adding benzoquinone to the deactivated catalyst which leads to a transformation of the surface atoms of the Pd nanoparticles. Pre-addition of benzoquinone to the reaction mixture is able to prevent the extensive formation of Pd nanoparticles and retain the activity of the catalyst.

An activation process of a homogeneous Ru catalyst was explored. The structure of the intermediate was elucidated by *in situ* XAS. The substituents on the cyclopentadiene ligands can significantly influence the activation rate. The substituents with electron-donating properties can promote the activation process, while the electron-withdrawing substituents have an inhibiting effect.

In addition to the *in situ* XAS studies of the catalytic reactions, *ex situ* XAS was applied to study the synthesis of heterogeneous Pd catalysts, such as Pd(II/0)@MOFs in Chapter 3, as well as Pd(0)-AmP-MCF and Pd(0)-CalB CLEA in Chapter 5. Successful immobilizations of Pd(II) precursors onto MOF supports were confirmed by XAS. The reduction of Pd(II) pre-catalysts to Pd(0) catalysts showed relatively complicated scenarios. Pd nanoparticles were the dominating species in Pd(0)-AmP-MCF. However, significant amounts of Pd(II) species were found in Pd(0)-CalB CLEA and Pd(0)@MOFs other than the Pd nanoparticles.

The results of these projects have shown the strength of using XAS to investigate the speciation and local structure of the metal species of interest in the catalytic procedures. The technique can be adapted to various types of catalysts and reaction systems to provide insights into the nature of the catalytic species.

9 Future Perspectives

In addition to the work presented in this thesis, several aspects concerning *in situ* XAS-based research can be considered.

First, X-ray emission spectroscopy (XES) can be used to distinguish C–, N– or O– ligands bound to Pd. Combination of XES and XAS can provide more precis understanding of the coordination environment of the absorbing atoms, particularly when the bond lengths are similar.

Second, one can continue to explore in the same direction as the work in this thesis. There are many other attractive catalysts and catalytic reactions that can be studied using the reactor presented in the thesis, such as molybdenum, ruthenium, rhodium and palladium-based systems.

Third, I would like to increase my knowledge of XANES to be able to analyze the local structure of the absorbing atoms through modelling XANES spectra. This can further improve the efficiency of *in situ* XAS measurements. The EXAFS region can then be excluded in the measurement while only focusing on XANES region. This process is helpful to either increase the time resolution of measurement or improve the S/N ratio of the data.

Fourth, it will be very exciting to apply *in situ* XAS to first row transition metals, such as manganese, iron, cobalt, nickel and copper, and their suspension/solution-based reactions. Chemists working on catalysis have been putting great efforts to replace the precious metals, such as ruthenium and palladium, by these more abundant and cheap metals. It would be of great value if *in situ* XAS can shed light on reaction mechanisms involving these elements. To achieve this goal, proper reactors are desired.

Last but not least, the quick XAS techniques have been more and more used during the recent years. It can greatly benefit measurements of fast chemical reactions. With higher time-resolution (at the levels of second or subsecond), the hidden intermediates might be able to be detected, which can provide important information of the reaction mechanism.

References

(1) Burrows, A. *Chemistry : introducing inorganic, organic and physical chemistry*, 3rd Ed. Oxford University Press, **2017**.

(2) *Catalytic Process Technology*; National Academies Press: Washington, D.C., **2000**.

(3) Cole-Hamilton, D. J.; Tooze, R. P. In *Catalyst separation, recovery and recycling : chemistry and process design*, Springer, **2006**. 16–17.

(4) Pangarkar, V. G. *Design of Multiphase Reactors*, 1st Ed. John Wiley & Sons, New Jersey, USA, **2014**.

(5) Lee, A. F.; Bennett, J. A.; Manayil, J. C.; Wilson, K. *Chem. Soc. Rev.* **2014**, *43* (22), 7887–7916.

(6) Tsuji, J. *Palladium Reagents and Catalysts*, John Wiley & Sons, Chichester, UK, **2004**.

(7) Gniewek, A.; Trzeciak, A. M.; Ziółkowski, J. J.; K˛ Epi´nskiepi´nski B, L.; Wrzyszcz, J.; Tylus, W. *J. Catal.* **2005**, *229*, 332–343.

(8) Van Bokhoven, J. A.; Lamberti, C. In *XAFS Techniques for Catalysts, Nanomaterials, and Surfaces*, Springer, **2017**, 299–316.

(9) Bloch, E. D.; Britt, D.; Lee, C.; Doonan, C. J.; Uribe-Romo, F. J.; Furukawa, H.; Long, J. R.; Yaghi, O. M. *J. Am. Chem. Soc.* **2010**, *132* (41), 14382–14384.

(10) Pascanu, V.; Bermejo Gómez, A.; Ayats, C.; Platero-Prats, A. E.; Carson, F.; Su, J.; Yao, Q.; Pericàs, M. À.; Zou, X.; Martín-Matute, B. *ACS Catal.* **2015**, *5* (2), 472–479.

(11) Platero-Prats, A. E.; Bermejo Gómez, A.; Samain, L.; Zou, X.; Martín-Matute, B. *Chem. - A Eur. J.* **2015**, *21* (2), 861–866.

(12) Thompson, A.; Attwood, D.; Gullikson, E.; Howells, M. . K.; K.-J.; Kirz, J.; Kortright, J.; Lindau, I.; Liu, Y.; Pianetta, P. . R.; A.; Scofield, J.; Underwood, J.; Williams, G.; Winick, H. *X-ray data booklet*, 3rd ed.; Lawrence Berkeley National Laboratory: Berkeley, **2009**.

(13) Jalilehvand, F. *Structure of hydrated ions and cyanide complexes by x-ray absorption spectroscopy*. Doctoral Thesis, Royal Institute of Technology, Stockholm, **2000**.

(14) Farges, F.; Brown, G. E.; Rehr, J. J. *Phys. Rev. B* **1997**, *56* (4), 1809–1819.

(15) Frank, P.; Hodgson, K. O.; Kustin, K.; Robinson, W. E. *J. Biol. Chem.* **1998**, *273* (38), 24498–24503.

(16) Jiang, N.; Su, D.; Spence, J. C. H. *Phys. Rev. B* **2007**, *76* (21), 214117.

(17) Solomon, E. I.; Lever, A. B. P. *Inorganic electronic structure and spectroscopy*, Wiley, **2006**.

(18) Ravel, B.; Newville, M.; IUCr. *J. Synchrotron Radiat.* **2005**, *12* (4), 537–541.

(19) Newville, M. *J. Phys. Conf. Ser.* **2013**, *430* (1), 012007.

(20) Klementiev, K. *VIPER (Visual Processing in EXAFS Researches)*. MAX IV Laboratory, Lund, **2013**.

(21) George, G. N. *EXAFSPAK: A Suite of Computer Programs for Analysis of X-ray Absorption Spectra*. SSRL, Standford, CA, **1993**.

(22) Zabinsky, S. I.; Rehr, J. J.; Ankudinov, A.; Albers, R. C.; Eller, M. J. *Phys. Rev. B* **1995**, *52* (4), 2995–3009.

(23) Singh, J.; Lamberti, C.; Van Bokhoven, J. A. *Chem. Soc. Rev.* **2010**, *39* (12), 4754–4766.

(24) Bordiga, S.; Groppo, E.; Agostini, G.; van Bokhoven, J. A.; Lamberti, C. *Chem. Rev.* **2013**, *113* (3), 1736–1850.

(25) Iwasawa, Y.; Asakura, K.; Tada, M. *XAFS Techniques for Catalysts, Nanomaterials, and Surfaces*, 1st Ed. Springer International Publishing, Switzerland, **2017**.

(26) Weckhuysen, B. M. *Chem. Commun.* **2002**, *0* (2), 97–110.

(27) Newton, M. A.; van Beek, W. *Chem. Soc. Rev.* **2010**, *39* (12), 4845.

(28) Kalz, K. F.; Kraehnert, R.; Dvoyashkin, M.; Dittmeyer, R.; Gläser, R.; Krewer, U.; Reuter, K.; Grunwaldt, J.-D. *ChemCatChem* **2017**, *9* (1), 17–29.

(29) Eslava, J. L.; Iglesias-Juez, A.; Agostini, G.; Fernández-García, M.; Guerrero-Ruiz, A.; Rodríguez-Ramos, I. *ACS Catal.* **2016**, *6* (3), 1437–1445.

(30) Jacobs, G.; Ma, W.; Gao, P.; Todic, B.; Bhatelia, T.; Bukur, D. B.; Davis, B. H. *Catal. Today* **2013**, *214*, 100–139.

(31) de Smit, E.; Cinquini, F.; Beale, A. M.; Safonova, O. V.; van Beek, W.; Sautet, P.; Weckhuysen, B. M. *J. Am. Chem. Soc.* **2010**, *132* (42), 14928–14941.

(32) Bezemer, G. L.; Bitter, J. H.; Kuipers, H. P. C. E.; Oosterbeek, H.; Holewijn, J. E.; Xu, X.; Kapteijn, F.; Dillen, A. J. van; Jong, K. P. de. *J. Am. Chem. Soc.* **2006**, *128* (12), 3956–3964.

(33) Rønning, M.; Tsakoumis, N. E.; Voronov, A.; Johnsen, R. E.; Norby, P.; van Beek, W.; Borg, Ø.; Rytter, E.; Holmen, A. *Catal. Today* **2010**, *155*, 289–295.

(34) Grunwaldt, J.-D.; Caravati, M.; Hannemann, S.; Baiker, A. *Phys. Chem. Chem. Phys.* **2004**, *6* (11), 3037–3048.

(35) van Beek, W.; Safonova, O. V.; Wiker, G.; Emerich, H. *Phase Transitions* **2011**, *84* (8), 726–732.

(36) Sherborne, G. J.; Chapman, M. R.; Blacker, A. J.; Bourne, R. A.; Chamberlain, T. W.; Crossley, B. D.; Lucas, S. J.; McGowan, P. C.; Newton, M. A.; Screen, T. E. O.; Thompson, P.; Willans, C. E.; Nguyen, B. N. *J. Am. Chem. Soc.* **2015**, *137* (12), 4151–4157.

(37) Ellis, P. J.; Fairlamb, I. J. S.; Hackett, S. F. J.; Wilson, K.; Lee, A. F. *Angew. Chemie Int. Ed.* **2010**, *49* (10), 1820–1824.

(38) Nagasaka, M.; Hatsui, T.; Horigome, T.; Hamamura, Y.; Kosugi, N. *J. Electron Spectros. Relat. Phenomena* **2010**, *177* (2–3), 130–134.

(39) Grunwaldt, J.-D.; Ramin, M.; Rohr, M.; Michailovski, A.; Patzke, G. R.; Baiker, A. *Rev. Sci. Instrum.* **2005**, *76* (5), 054104.

(40) Heidenreich, N.; Rütt, U.; Köppen, M.; Inge, A. K.; Beier, S.; Dippel, A.-C.; Suren, R.; Stock, N. *Rev. Sci. Instrum.* **2017**, *88* (10), 104102.

(41) Yuan, N.; Pascanu, V.; Huang, Z.; Valiente, A.; Heidenreich, N.; Leubner, S.; Inge, A. K.; Gaar, J.; Stock, N.; Persson, I.; Martín-Matute, B.; Zou, X. *J. Am. Chem. Soc.* **2018**,

140 (26), 8206–8217.

(42) Andersen, C. W.; Borfecchia, E.; Bremholm, M.; Jørgensen, M. R. V.; Vennestrøm, P. N. R.; Lamberti, C.; Lundegaard, L. F.; Iversen, B. B. *Angew. Chemie Int. Ed.* **2017**, *56* (35), 10367–10372.

(43) Grunwaldt, J.-D.; Clausen, B. S. *Top. Catal.* **2002**, *18* (1–2), 37–43.

(44) P64 Advanced X-ray Absorption Spectroscopy http://photon-science.desy.de/facilities/petra_iii/beamlines/p64_advanced_xafs/index_eng.html.

(45) Zhou, Y.; Doronkin, D. E.; Chen, M.; Wei, S.; Grunwaldt, J.-D. *ACS Catal.* **2016**, *6* (11), 7799–7809.

(46) Casapu, M.; Fischer, A.; Gänzler, A. M.; Popescu, R.; Crone, M.; Gerthsen, D.; Türk, M.; Grunwaldt, J.-D. *ACS Catal.* **2017**, *7* (1), 343–355.

(47) Manzoli, M.; Vindigni, F.; Tabakova, T.; Lamberti, C.; Dimitrov, D.; Ivanov, K.; Agostini, G. *J. Mater. Chem. A* **2017**, *5* (5), 2083–2094.

(48) Barzan, C.; Piovano, A.; Braglia, L.; Martino, G. A.; Lamberti, C.; Bordiga, S.; Groppo, E. *J. Am. Chem. Soc.* **2017**, *139* (47), 17064–17073.

(49) Lamberti, C.; Prestipino, C.; Bonino, F.; Capello, L.; Bordiga, S.; Spoto, G.; Zecchina, A.; Diaz Moreno, S.; Cremaschi, B.; Garilli, M.; Marsella, A.; Carmello, D.; Vidotto, S.; Leofanti, G. *Angew. Chemie Int. Ed.* **2002**, *41* (13), 2341–2344.

(50) Newton, M. A.; Belver-Coldeira, C.; Martínez-Arias, A.; Fernández-García, M. *Nat. Mater.* **2007**, *6* (7), 528–532.

(51) Braglia, L.; Borfecchia, E.; Maddalena, L.; Øien, S.; Lomachenko, K. A.; Bugaev, A. L.; Bordiga, S.; Soldatov, A. V.; Lillerud, K. P.; Lamberti, C. *Catal. Today* **2017**, *283*, 89–103.

(52) Alexopoulos, K.; Anilkumar, M.; Reyniers, M.-F.; Poelman, H.; Cristol, S.; Balcaen, V.; Heynderickx, P. M.; Poelman, D.; Marin, G. B. *Appl. Catal. B Environ.* **2010**, *97* (3–4), 381–388.

(53) Benzi, F.; Sheppard, T. L.; Doronkin, D. E.; Meira, D. M.; Gänzler, A. M.; Baier, S.; Grunwaldt, J.-D. *Catal. Sci. Technol.* **2017**, *7* (18), 3999–4006.

(54) Nilsson, J.; Carlsson, P.-A.; Fouladvand, S.; Martin, N. M.; Gustafson, J.; Newton, M. A.; Lundgren, E.; Grönbeck, H.; Skoglundh, M. *ACS Catal.* **2015**, *5* (4), 2481–2489.

(55) Stötzel, J.; Frahm, R.; Kimmerle, B.; Nachtegaal, M.; Grunwaldt, J.-D. *J. Phys. Chem. C* **2012**, *116* (1), 599–609.

(56) Balder – MAX IV https://www.maxiv.lu.se/accelerators-beamlines/beamlines/balder/.

(57) Iglesias-Juez, A.; Beale, A. M.; Maaijen, K.; Weng, T. C.; Glatzel, P.; Weckhuysen, B. M. *J. Catal.* **2010**, *276* (2), 268–279.

(58) de Boer, M.; van Dillen, A. J.; Koningsberger, D. C.; Geus, J. W.; Vuurman, M. A.; Wachs, I. E. *Catal. Letters* **1991**, *11* (2), 227–239.

(59) Yin, G.; Kalvet, I.; Schoenebeck, F. *Angew. Chemie Int. Ed.* **2015**, *54* (23), 6809–6813.

(60) Aufiero, M.; Scattolin, T.; Proutière, F.; Schoenebeck, F. *Organometallics* **2015**, *34* (20), 5191–5195.

(61) Diehl, C. J.; Scattolin, T.; Englert, U.; Schoenebeck, F. *Angew. Chemie Int. Ed.* **2019**, *58* (1), 211–215.

(62) Yaghi, O. M.; O'Keeffe, M.; Ockwig, N. W.; Chae, H. K.; Eddaoudi, M.; Kim, J. *Nature* **2003**, *423* (6941), 705–714.

(63) Férey, G. *Chem. Soc. Rev.* **2008**, *37* (1), 191–214.

(64) Long, J. R.; Yaghi, O. M. *Chem. Soc. Rev.* **2009**, *38* (5), 1213.

(65) Zhou, H.-C.; Long, J. R.; Yaghi, O. M. *Chem. Rev.* **2012**, *112* (2), 673–674.

(66) Batten, S. R.; Champness, N. R.; Chen, X.-M.; Garcia-Martinez, J.; Kitagawa, S.; Öhrström, L.; O’Keeffe, M.; Paik Suh, M.; Reedijk, J. *Pure Appl. Chem.* **2013**, *85* (8), 1715–1724.

(67) Moghadam, P. Z.; Li, A.; Wiggin, S. B.; Tao, A.; Maloney, A. G. P.; Wood, P. A.; Ward, S. C.; Fairen-Jimenez, D. *Chem. Mater.* **2017**, *29* (7), 2618–2625.

(68) Farha, O. K.; Eryazici, I.; Jeong, N. C.; Hauser, B. G.; Wilmer, C. E.; Sarjeant, A. A.; Snurr, R. Q.; Nguyen, S. T.; Yazaydın, A. Ö.; Hupp, J. T. *J. Am. Chem. Soc.* **2012**, *134* (36), 15016–15021.

(69) Stock, N.; Biswas, S. *Chem. Rev.* **2012**, *112* (2), 933–969.

(70) Furukawa, H.; Cordova, K. E.; O’Keeffe, M.; Yaghi, O. M. *Science* **2013**, *341* (6149), 1230444.

(71) Férey, G.; Mellot-Draznieks, C.; Serre, C.; Millange, F.; Dutour, J.; Surblé, S.; Margiolaki, I. *Science* **2005**, *309* (5743), 2040–2042.

(72) Surblé, S.; Serre, C.; Mellot-Draznieks, C.; Millange, F.; Férey, G. *Chem. Commun.* **2006**, *0* (3), 284–286.

(73) Pascanu, V.; Yao, Q.; Bermejo Gómez, A.; Gustafsson, M.; Yun, Y.; Wan, W.; Samain, L.; Zou, X.; Martín-Matute, B. *Chem. - A Eur. J.* **2013**, *19* (51), 17483–17493.

(74) Pascanu, V.; Hansen, P. R.; Bermejo Gómez, A.; Ayats, C.; Platero-Prats, A. E.; Johansson, M. J.; Pericàs, M. À.; Martín-Matute, B. *ChemSusChem* **2015**, *8* (1), 123–130.

(75) Carson , F.; Pascanu , V.; Bermejo Gómez , A.; Zhang , Y.; Platero-Prats , A. E.; Zou , X.; Martín-Matute , B. *Chem. - A Eur. J.* **2015**, *21* (30), 10896–10902.

(76) Pascanu, V.; Carson, F.; Solano, M. V.; Su, J.; Zou, X.; Johansson, M. J.; Martín-Matute, B. *Chem. - A Eur. J.* **2016**, *22* (11), 3729–3737.

(77) Gotthardt, M. A.; Beilmann, A.; Schoch, R.; Engelke, J.; Kleist, W. *RSC Adv.* **2013**, *3* (27), 10676.

(78) Bloch, E. D.; Britt, D.; Lee, C.; Doonan, C. J.; Uribe-Romo, F. J.; Furukawa, H.; Long, J. R.; Yaghi, O. M. *J. Am. Chem. Soc.* **2010**, *132* (41), 14382–14384.

(79) Duan, H.; Li, M.; Zhang, G.; Gallagher, J. R.; Huang, Z.; Sun, Y.; Luo, Z.; Chen, H.; Miller, J. T.; Zou, R.; Lei, A.; Zhao, Y. *ACS Catal.* **2015**, *5* (6), 3752–3759.

(80) Li, X.; Guo, Z.; Xiao, C.; Goh, T. W.; Tesfagaber, D.; Huang, W. *ACS Catal.* **2014**, *4* (10), 3490–3497.

(81) Torapava, N.; Elding, L. I.; Mändar, H.; Roosalu, K.; Persson, I. *Dalt. Trans.* **2013**, *42* (21), 7755.

(82) Keating, J.; Sankar, G.; Hyde, T. I.; Kohara, S.; Ohara, K. *Phys. Chem. Chem. Phys.* **2013**, *15* (22), 8555.

(83) Newton, M. A.; Brazier, J. B.; Barreiro, E. M.; Emerich, H.; Adrio, L. A.; Mulligan, C. J.; Hellgardt, K.; Hii, K. K. (Mimi). *Catal. Sci. Technol.* **2016**, *6* (24), 8525–8531.

(84) Beletskaya, I. P.; Cheprakov, A. V. *Chem. Rev.* **2000**, *100* (8), 3009–3066.

(85) Academic Software: Otley, UK 2014.

(86) Hellquist, B.; Elding, L. I.; Ducommun, Y. *Inorg. Chem.* **1988**, *27* (20), 3620–3623.

(87) Boily, J.-F.; Seward, T. M. *Geochim. Cosmochim. Acta* **2005**, *69* (15), 3773–3789.

(88) Elding, L. I. *Inorganica Chim. Acta* **1972**, *6*, 647–651.

(89) Rittner, W. P.; Gulko, A.; Schmuckler, G. *Talanta* **1970**, *17* (9), 807–816.

(90) Shimizu, K.; Kubo, T.; Satsuma, A.; Kamachi, T.; Yoshizawa, K. *ACS Catal.* **2012**, *2* (12), 2467–2474.

(91) Agostini, G.; Lamberti, C.; Pellegrini, R.; Leofanti, G.; Giannici, F.; Longo, A.; Groppo, E. *ACS Catal.* **2014**, *4* (1), 187–194.

(92) Grunwaldt, J-D.; Caravati, M.; Baiker, A. *J. Phys. Chem. B*, **2006**. *110* (0), 9916–9922.

(93) Qi, W.; Huang, B.; Wang, M. *Nanoscale Res. Lett.* **2009**, *4* (3), 269–273.

(94) Krüger, S.; Vent, S.; Nörtemann, F.; Staufer, M.; Rösch, N. *J. Chem. Phys.* **2001**, *115* (5), 2082–2087.

(95) Jentys, A. *Phys. Chem. Chem. Phys.* **1999**, *1* (17), 4059–4063.

(96) Keith, J.; Henry, P. *Angew. Chemie Int. Ed.* **2009**, *48* (48), 9038–9049.

(97) Froese, R. D. J.; Lombardi, C.; Pompeo, M.; Rucker, R. P.; Organ, M. G. *Acc. Chem. Res.* **2017**, *50* (9), 2244–2253.

(98) Fortman, G. C.; Nolan, S. P. *Chem. Soc. Rev.* **2011**, *40* (10), 5151.

(99) Peris, E. *Chem. Rev.* **2018**, *118* (19), 9988–10031.

(100) Zhong, R.; Lindhorst, A. C.; Groche, F. J.; Kühn, F. E. *Chem. Rev.* **2017**, *117* (3), 1970–2058.

(101) Majeed, M. H.; Shayesteh, P.; Wallenberg, L. R.; Persson, A. R.; Johansson, N.; Ye, L.; Schnadt, J.; Wendt, O. F. *Chem. - A Eur. J.* **2017**, *23* (35), 8457–8465.

(102) Pérez-Mayoral, E.; Calvino-Casilda, V.; Soriano, E. *Catal. Sci. Technol.* **2016**, *6* (5), 1265–1291.

(103) Majeed, M. H.; Shayesteh, P.; Persson, A. R.; Wallenberg, L. R.; Schnadt, J.; Wendt, O. F. *Eur. J. Inorg. Chem.* **2018**, *2018* (43), 4742–4746.

(104) Sabater, S.; Mata, J. A.; Peris, E. *ACS Catal.* **2014**, *4* (6), 2038–2047.

(105) Sabater, S.; Mata, J. A.; Peris, E. *Organometallics* **2015**, *34* (7), 1186–1190.

(106) Guilera, G.; Newton, M. A.; Polli, C.; Pascarelli, S.; Guinó, M.; Hii, K. K. (Mimi). *Chem. Commun.* **2006**, *0* (41), 4306.

(107) Eitel, S. H.; Bauer, M.; Schweinfurth, D.; Deibel, N.; Sarkar, B.; Kelm, H.; Krüger, H.-J.; Frey, W.; Peters, R. *J. Am. Chem. Soc.* **2012**, *134* (10), 4683–4693.

(108) Jagadeesan, R.; Velmurugan, G.; Venuvanalingam, P. *RSC Adv.* **2015**, *5* (98), 80661–80667.

(109) Powers, D. C.; Ritter, T. *Nat. Chem.* **2009**, *1* (4), 302–309.

(110) Lyons, T. W.; Sanford, M. S. *Chem. Rev.* **2010**, *110* (2), 1147–1169.

(111) Dang, Y.; Qu, S.; Nelson, J. W.; Pham, H. D.; Wang, Z.-X.; Wang, X. *J. Am. Chem. Soc.* **2015**, *137* (5), 2006–2014.

(112) Nagendiran, A.; Verho, O.; Haller, C.; Johnston, E. V.; Bäckvall, J.-E. *J. Org. Chem.* **2014**, *79* (3), 1399–1405.

(113) Bruneau, A.; Gustafson, K. P. J.; Yuan, N.; Tai, C.-W.; Persson, I.; Zou, X.; Bäckvall, J.-E. *Chem. - A Eur. J.* **2017**, *23* (52), 12886–12891.

(114) Shakeri, M.; Tai, C.; Göthelid, E.; Oscarsson, S.; Bäckvall, J.-E. *Chem. - A Eur. J.* **2011**, *17* (47), 13269–13273.

(115) Johnston, E. V.; Verho, O.; Kärkäs, M. D.; Shakeri, M.; Tai, C.-W.; Palmgren, P.; Eriksson, K.; Oscarsson, S.; Bäckvall, J.-E. *Chem. - A Eur. J.* **2012**, *18* (39), 12202–12206.

(116) Gustafson, K. P. J.; Lihammar, R.; Verho, O.; Engström, K.; Bäckvall, J.-E. *J. Org. Chem.* **2014**, *79* (9), 3747–3751.

(117) Engström, K.; Johnston, E. V.; Verho, O.; Gustafson, K. P. J.; Shakeri, M.; Tai, C.-W.; Bäckvall, J.-E. *Angew. Chemie Int. Ed.* **2013**, *52* (52), 14006–14010.

(118) Nagendiran, A.; Sörensen, H.; Johansson, M. J.; Tai, C.-W.; Bäckvall, J.-E. *Green Chem.* **2016**, *18* (9), 2632–2637.

(119) Verho, O.; Åkermark, T.; Johnston, E. V.; Gustafson, K. P. J.; Tai, C.-W.; Svengren, H.; Kärkäs, M. D.; Bäckvall, J.-E.; Åkermark, B. *Chem. - A Eur. J.* **2015**, *21* (15), 5909–5915.

(120) Görbe, T.; Gustafson, K. P. J.; Verho, O.; Kervefors, G.; Zheng, H.; Zou, X.; Johnston, E. V.; Bäckvall, J.-E. *ACS Catal.* **2017**, *7* (3), 1601–1605.

(121) Nyhlén, J.; Privalov, T.; Bäckvall, J.-E. *Chem. - A Eur. J.* **2009**, *15* (21), 5220–5229.

(122) Stewart, B.; Nyhlen, J.; Martín-Matute, B.; Bäckvall, J.-E.; Privalov, T. *Dalt. Trans.* **2013**, *42* (4), 927–934.

(123) Warner, M. C.; Verho, O.; Bäckvall, J.-E. *J. Am. Chem. Soc.* **2011**, *133* (9), 2820–2823.

(124) Åberg, J. B.; Nyhlén, J.; Martín-Matute, B.; Privalov, T.; Bäckvall, J.-E. *J. Am. Chem. Soc.* **2009**, *131* (27), 9500–9501.

(125) Zhou, M.; Andrews, L.; Charles W. Bauschlicher, C. W. **2001**. *101* (7), 1931–1961.

(126) Martín-Matute, B.; Edin, M.; Bogár, K.; Bäckvall, J.-E. *Angew. Chemie Int. Ed.* **2004**, *43* (47), 6535–6539.

(127) Martín-Matute, B.; Edin, M.; Bogár, K.; Kaynak, F. B.; Bäckvall, J.-E. *J. Am. Chem. Soc.* **2005**, *127* (24), 8817–8825.

(128) Lihammar, R.; Millet, R.; Bäckvall, J.-E. *Adv. Synth. Catal.* **2011**, *353* (13), 2321–2327.

(129) Lihammar, R.; Millet, R.; Bäckvall, J.-E. *J. Org. Chem.* **2013**, *78* (23), 12114–12120.

(130) Casey, C. P.; Singer, S. W.; Powell, D. R.; Hayashi, R. K.; Kavana, M. *J. Am. Chem. Soc.* **2001**, *123* (6), 1090–1100.

(131) Samec, J. S. M.; Éll, A. H.; Privalov, T.; Eriksson, L.; Bäckvall, J.-E. *J. Am. Chem. Soc.* **2006**, *128* (44), 14293–14305.

(132) Martín-Matute, B.; Åberg, J. B.; Edin, M.; Bäckvall, J.-E. *Chem. - A Eur. J.* **2007**, *13* (21), 6063–6072.

(133) Getty, K.; Delgado-Jaime, M. U.; Kennepohl, P. *Inorganica Chim. Acta* **2008**, *361* (4), 1059.

Popular science summary

Development of catalysts and catalytic processes are essential for the chemical industry. Therefore, it is important to acquire detailed knowledge about catalytic species and processes. Previously, research focused on characterizations of unused catalysts. However, it has been realized that, in many cases, catalysts undergo changes during the reaction processes, which raises the demand of unveiling the evolution of catalytic species. In this thesis, palladium (Pd) and ruthenium (Ru) catalytic species over the course of various reaction processes were studied using *in situ* X-ray absorption spectroscopy (XAS) as the major approach.

XAS is an element-specific technique. It can probe the coordination environment of absorbing atoms and estimate their oxidation states, regardless of the sample state. These properties make XAS suitable for the study of catalysts. Several attractive Pd and Ru catalysts were examined by both *in situ* and *ex situ* XAS measurements. Pd(II) complexes immobilized on various catalyst supports, including metal-organic frameworks (Pd(II)@MOFs), reduced graphene oxide (Pd(II)@rGO), and amino-functionalized siliceous mesocellular foam (Pd(II)@AmP-MCF), are some of the examples. It has been shown that the Pd and Ru species changed at different stages of the catalytic reactions. For example, Pd(II)@MOFs were used to catalyze the Heck coupling reaction. Ligand exchange occurs firstly and the reaction is catalyzed by mononuclear Pd complexes bound to the MOF support. At a later stage, the complexes detach from the support and gradually transform into nanoclusters. The mixture of Pd complexes and nanoclusters act as the active species. When the reaction is close to the end, chloride ions existing in the reaction mixture start binding to the surface of the Pd nanoclusters causing deactivation of the catalyst. Based on these insights into the reaction process, a method to prolong the lifetime of the catalyst was developed. By introducing new reagents before the chloride ions bind to palladium clusters, the poisoning of the catalyst can be avoided. Changes in the structure and oxidation state of Pd were also discovered in Pd(II)@rGO and Pd(II)@AmP-MCF during the reactions. Besides the studies of Pd catalysts, the activation process of a Ru catalyst was also explored. The structure of an important intermediate was unveiled by *in situ* XAS measurements.

The main goal of this thesis is to show that *in situ* XAS is an effective approach to probe the catalytic species and their changes during reactions. The information acquired is of great value for the development of new catalysts with better performance, and prolonging the lifetime of catalysts in use.

Populärvetenskaplig sammanfattning

Utveckling av katalysatorer och katalysprocesser är essentiellt för den kemiska industrin. Därför är det viktigt att få detaljerad kunskap om hur katalytiska ämnen och processer fungerar. Tidigare har forskningen fokuserat på att karakterisera katalysatorer innan reaktion, men i många fall sker en kemisk förändring av själva katalysatorn under reaktionsprocessen. Det finns därför en stor efterfrågan att studera reaktioner i realtid för att karakterisera katalysatorers förändringar. I den här avhandlingen undersöktes förändringar av palladium- (Pd) och ruteniumämnen (Ru) i olika reaktionsprocesser. Huvudverktyget var röntgenabsorptionsspektroskopi (XAS) *in situ*.

XAS är en grundämnesspecifik teknik som kan analysera atomers koordination och oxidationstal oavsett provtillstånd. Denna egenskap gör XAS lämplig för att studera katalysatorer. Flera lovande Pd- och Ru-katalysatorer undersöktes både *in situ* och ex situ med XAS. Några exempel är Pd(II)-komplex bundet till metallorganiska ramverk (Pd(II)@MOFs), till reducerad grafenoxid (Pd(II)@rGO), eller till aminofunktionaliserat kiselhaltigt mesocellulärt skum (Pd(II)@AmP-MCF). Det visade sig att bindning och struktur kring Pd förändrar sig under de katalytiska reaktionernas olika faser. I fallet med Pd(II)@MOF som katalyserar Hecks kopplingsreaktion, sker en ligandutbytesprocess och reaktionen katalyseras genom Pd-komplex som är bundna till MOF-strukturen. Sedan lossnar komplexet från MOF-strukturen och omvandlas till kluster av nanostorlek, vilka också katalyserar reaktionen. När reaktionen är nära slutet börjar kloridjoner som finns i systemet att binda till ytan av klusterstrukturen, vilket leder till deaktivering av katalystorn. Baserat på denna fördjupade förståelse av processen utvecklades en ny metod. Genom att tillsätta nytt reagens innan kloridjonerna binder till Pd-klustren kan deaktivering undvikas. Strukturella och kemiska förändringar upptäcktes också i fallet med Pd(II)@rGO och Pd(II)@AmP-MCF. Observationerna diskuteras i detalj i avhandlingen. Förutom studier av Pd-katalystorer, undersöktes också aktiveringsprocessen för en Ru-katalysator där strukturella förändringar av en viktig Ru-intermediär belystes genom XAS experiment *in situ*.

Det huvudsakliga syftet med avhandlingen är att visa att XAS-mätning *in situ* är en effektiv metod för att utforska katalytiska ämnen och hur de förändras under kemiska processer. Informationen är betydelsefull för att utveckla nya katalysatorer med hög aktivitet, och för att undvika deaktivering som leder till förkortad livslängd för katalysatorer.

Acknowledgements

The journey of pursuing a Ph.D. degree is never smooth, but extremely rewarding. I cannot image the accomplishment of this thesis without others' contributions and constant supports. I would like to express my sincerest gratitude to:

Prof. Ingmar Persson and Professor Xiaodong Zou for accepting me as a joint Ph.D. student. I am really lucky to have both of you guiding my work and many other aspects of my life. It is a great benefit having two main superiors with different experiences and personalities. I went through my Ph.D. study for one time, but received two times of help and training. I am grateful that you encouraged me to take the responsibilities of my work and drive the projects forward. Although it wasn't easy for me at the beginning, but I never felt helpless because I always received instant help from you when things were beyond of my ability. Many thanks for providing me the opportunities and resources to accomplish the projects in this thesis, and all the rewarding discussions.

The Foundations and agencies for the financial support. The work in this thesis was funded by the MATsynCELL project through Röntgen-Ångström Cluster, supported by the Swedish Research Council (VR, project no. 2013-580) and the German Federal Ministry of Education and Research (BMBF). I am also thankful to the Berzelii Center EXSELENT on Porous Materials, the Swedish Research Council (VR, project no. 2017-0432) and the Project Management Organization at DESY (Deutsches Electronen-Synchrotron). The project grants 3DEM-NATUR and CATSS are also appreciated.

Prof. Belén Martín-Matute, Prof. Jan-Erling Bäckvall and Prof. Ola Wendt for leading me into the world of catalysis and sharing the joint research interests. Without your catalysts and chemistry, the projects wouldn't be successful, and ideas would have remained as ideas.

Prof. Norbert Stock, for the design and development of the *in situ* reactor, as well as all the great support from your group during the beamtimes for the XAS and PXRD measurements.

Vlad Pascanu for the will to take the risk with me and perform the first *in situ* XAS experiments in this thesis.

Karl Gustafson for blowing my mind with your chemistry and dedications to the work. I remember clearly your record of more than 30 hours' nonstop experiments at the beamline, and your question to me: why do you need to book a guest-room when you are using the precious beamtime?

Éva Bajnóczi for joining me on this boat, and all the spontaneous discussions, and proofreading of this thesis, and of course the Thursdays' pancakes.

Arnar Guðmundsson for always waiting for me at the door of your department and proofreading this thesis, as well as the hard work and the joyful train trip to Hamburg.

Maitham Majeed for sharing with me your research interests and all the instant discussions over the phone.

Molly for proofreading this thesis. The language fika will keep rolling.

Many other awesome collaborators who I had the pleasure to work closely: Diana, Ken, Niclas, Sebastian, Alejandro, Sergio, Antonio, Zhehao, Jakob, Axel, Rein, Michael, Oscar, Alexandre, Tamás, Cheuk-Wai, Tamara, Erik, Niklas for the valuable contributions to the work in this thesis.

Beamline BM01B, European Synchrotron Radiation Facility (ESRF), beamline P64, Petra III Extension, Deutsches Electronen-Synchrotron (DESY) and beamline I811, MaxLab II for the allocations of precious XAS beamtimes. *Beamline scientists, Dr. Michela Brunelli and Dr. Hermann Emerich at BM01B, Dr. Vadim Murzin and Dr. Wolfgang Caliebe at P64, and Dr. Stefan Carlson at I811* for the great supports at the beamlines for the XAS experiments.

All my awesome current and previous colleagues at SLU and SU, Éva, Gunnar, Daniel, Vadim, Gulaim, Martin, Elisabeth, Hanna, Fredric, Sonja, Ali, Gustav, Jerry, Frida, Viktor, Magdalena, Elina, Bin, Zhehao, Laura, Hongyi, Taimin, *Max, Molly, Jingjing, Aditya, Daniel, Maria, Thomas, Erik, Mylad, Mirva, Yi, Tom, Taimin, Chris, Yuan, Istvan, Junliang, Junzhong, Ahmed, Fei, Alexandra, Fabian, Hani, Wei, Yunchen, Yang, Leifeng, Yifeng, Yinxin, Jie, Jonas, Haoquan, Peng, Stef, Yunxiang, Dickson, Qingpeng, Ximeng, Jia, Olga, Elisabeth, Vadim, Fredrik, Shun, Jiho, James, Fredrik, Zoltan, Rolf, Jekabs, Mats and many others* for the wonderful time we spent together.

Ph.D. council board members at MMK: Inna, Yulia, Korneliya for influencing me with your engagements in helping others.

Helmi Frejman not only for encouraging me to learn Swedish, but also the great help of arranging the beautiful home where Lukas was born.

Prof. Sven Hovmöller for those wonderful *svenska luncher* and enjoyable stories, totally worth the price of the food.

Viktor Bengtsson, well, we don’t really have joint projects, but I owe you big at work. Thank you for sitting next to me and NOT speaking English with me. Now you inspired me to the world of Python, it just keeps going.

My kind teaching colleagues, Anne, Viktor, Karim, Mirva, Lars, Arnold, Mattias for all the help during the teaching periods.

My lovely students, I know there are a hundred of you. I never thought I would gain so rich experience from the teaching. Without you I would never dare to speak Swedish in public.

My dear friend Hermann Berg for being my family in Sweden when I first came. You really gave me lots of strength to live and grow in this country. *And Niclas Jonsberg* for being a bright and positive model in my life, although I am jealous of how young you are.

My dear friends outside work, Selena, Yishi, Ling, Philip, Oscar, Karin, Huina, Yuanyuan, Hui, Ana, Ola, Anotonio, Wolfgang, Xinfeng, Haiyan, Shimizu, Kelvin, Justin, Steffi, Kerstin, Andrea, Nazanin, Wentong, Jing, Jie, Fei, Kevin, Maja, Chenxi, Anqi, Lin, Dongmin, Duoduo, Wenbin, Bo, Yanjuan, Feng, Wenzhao, Dongmei, Wenqiong, Wentong, Hüsan, Biaobiao, Qijun, Xinchen, Pierre, Yina, Mattias and many others.

My parents Shuxia Wang and Baosheng Yuan for raising me up and giving me the chance to choose my own path. Home is always home.

My wife Qiong Wu, for the 13 years of beautiful life in China, Japan and Sweden. I was always trying hard to lead our small team, but you were the one who did a better job and guilded us. Thank you!

My son Lukas, having you in our sweet family is the best thing that ever happened in my life. You made me a better person every single day.